Hybrid RF-Acoustic Ranging for Energy Efficient Indoor Positioning

Bert Cox

Supervisor:
Prof. dr. ir. L. De Strycker
Co-supervisor:
Prof. dr. ir. L. Van der Perre

Dissertation presented in partial fulfillment of the requirements for the degree of Doctor of Engineering Technology (PhD)

June 2022

Hybrid RF-Acoustic Ranging for Energy Efficient Indoor Positioning

Bert COX

Examination committee:
Prof. dr. ir. B. Meesschaert, chair
Prof. dr. ir. L. De Strycker, supervisor
Prof. dr. ir. L. Van der Perre, co-supervisor
Prof. dr. ir. T. van Waterschoot
Prof. dr. ir. V. De Smedt
Dr. ir. K. Deforche
  (BlooLoc, Belgium)
Prof. dr. ir. K. Witrisal
  (TU Graz, Austria)

June 2022

Preface

The worth of a human being lies in the ability to extend oneself, to go outside oneself, to exist in and for other people.

Milan Kundera - Laughable Loves

During the course of this PhD, I have searched long and extensively for a fitting quote to open this thesis. Being in doubt about phrases from read books, cheesy movie quotes, or lyrics from songs I have listened to on repeat, it was hard to pick a single sentence that snapshots 5 years of research. It was only one month prior to the start of the final, ambitious writing session, I came along the above quote from Milan Kundera. This PhD was conducted during some of the most intense years of my early adulthood and there are a lot of people that extended and went outside themselves for me that I would like to thank.

First of all, I would like to express my gratitude to Lieven, Liesbet, Jean-Pierre and Nobby for giving me this opportunity. By joining DRAMCO in 2015, I was able to refine my research, programming and hardware skills by means of various interesting projects. It was in one of these projects with BlooLoc that a clear research subject emerged, enabling to pursue my ambition for a PhD.

This job has brought me to places I could not imagine and let me meet interesting people from all over the world. However, it is always pleasant to come home to the DRAMCO group. Thank you Geoffrey for taking the role as a big brother in our research group. You are always in for a laugh, but when things get serious, I know we can count on your support and feedback. A special thanks to Stijn W. and Bart, you both mentored me in the beginning of this PhD and gave some crucial advice in both the RF and acoustic research domains. Thank you Guus for the 'Guusification' of posters and presentations, and together with Jarne, for answering all my hardware related questions. Thank you Gilles for your everlasting enthusiasm, sincere interest and generous insights. Thank you Chesney and Daan

Abstract

For many years, persons and objects experience the advantages and comfort of positioning for wayfinding, asset tracking and even gaming. Most of these applications perform well in the outdoors but suffer from poor accuracy and precision when used in indoor environments. The fast adoption of digital technologies to improve efficiency and deploy new services in diverse sectors leads to an increasingly high number of objects getting an ID in the virtual world. However, as more and more applications depend on knowing the exact position of these objects, the need for a precise and low-power indoor positioning system is bigger than ever.

This work introduces an unconventional hybrid RF-acoustic indoor ranging system. The hybrid approach is chosen based on an extensive, energy consumption focused assessment of current systems. It exploits the slower propagating acoustic waves for ranging together with the instantaneous character of electromagnetic signals for synchronization and communication.

To enable energy-neutrality at the mobile node, a disruptive system design is established that comprehends innovation in structural, hardware and communicative practices. The mobile nodes are kept as lazy as possible, by low active times and letting others do the processing. A major, original contribution lies in the signaling approach that does not transmit the RF and acoustic signal simultaneously, yet uses the RF signal for a synchronized wake-up of the mobile nodes. These mobile nodes receive a different part of the original broadcasted ultrasonic chirp, depending on their distance to the acoustic source. Backscattering is adopted to communicate the received, zero-crossed digitized, ultrasonic chirp snippets back to a processing unit where pulse compression is applied. A last contribution to enable energy-neutral indoor ranging comes in the form of RF energy harvesting.

Simulation-based evaluations are performed in an image source model engine, allowing to test the impact of environmental and hardware implications on the pulse

compression method applied to the ultrasonic signals. Simulation-based refinement is essential for the prototype design and experimental validation of the system in real-life environments. These experiments analyze the power consumption, the pure acoustic ranging error and a hybrid system ranging error with RF backscatter. In conclusion, the architectural and algorithmic co-design of this hybrid RF-acoustic ranging system proposed in this PhD is mature enough to explore energy-neutral, indoor 3D positioning.

Beknopte samenvatting

Personen en objecten genieten sinds enige jaren van de voordelen en het comfort van buitenshuise positionering in toepassingen zoals navigeren, het opvolgen van goederentransport en zelfs gamen. Veel van deze applicaties werken uitstekend in buitenomgevingen maar ontbreken echter de vereiste nauwkeurigheid en precisie wanneer ze gebruikt worden binnen gebouwen. De snelle adoptie van digitale technologie in verschillende sectoren heeft als doel de efficiëntie te verhogen en nieuwe diensten te lanceren. Een gevolg hiervan is dat een steeds groeiend aantal objecten een identificatie krijgen in de virtuele wereld. Nu meer en meer applicaties afhangen van de exacte positie van deze objecten, blijft de vraag naar een precies en energie-efficiënt binnenshuis positioneringssysteem groeien.

In dit werk wordt een geavanceerd hybride RF-akoestisch systeem voor *indoor* afstandsbepaling geïntroduceerd. Deze hybride benadering is gekozen na een uitgebreide studie met de focus op het energieverbruik. Het exploiteert de trager voortbewegende akoestische golven om afstanden te bepalen en de ogenblikkelijke aanwezigheid van elektromagnetische signalen voor synchronisatie- en communicatiedoeleinden.

Om de energieneutraliteit van de mobiele nodes te verzekeren wordt er in dit onderzoek een baanbrekend systeem ontwikkeld dat innovaties op structureel, hardware en communicatief vlak introduceert. De hardware aan de gebruikerskant wordt zo lui mogelijk gehouden door de actieve tijd te limiteren en berekeningen uit te besteden aan anderen. Een belangrijk en originele bijdrage in dit doctoraat komt van de werkwijze waarop signalen worden verzonden. Het systeem voorkomt dat RF en akoestische signalen tegelijk worden uitgezonden maar gebruikt het RF signaal om de mobiele nodes tegelijkertijd te ontwaken. Afhankelijk van de afstand tot de zender ontvangen de mobiele nodes een ander deel van een verzonden, ultrasone chirp. *Backscattering* is geïmplementeerd als communicatiemiddel waarover de ontvangen, gedigitaliseerde, ultrasone chirp signalen worden verstuurd voor verdere verwerking door middel van pulscompressie. Een laatste bijdrage om

de energieneutraliteit mogelijk te maken bestaat uit het capteren van energie uit elektromagnetische golven.

Simulaties zijn uitgevoerd in een *image source model* omgeving. Hierin wordt de impact van omgevings- en hardware invloeden op de pulscompressie van de ultrasone geluidsfragmenten uitgetest. Verbeteringen bekomen dankzij deze simulaties zijn essentieel voor het prototype ontwerp dat het systeem verder beoordeelt in een waarheidsgetrouwe testomgevingen. De experimenten laten toe om het energieverbruik, de meetfout voor puur akoestische afstandsbepaling en de meetfout wanneer het systeem wordt uitgebreid met RF-*backscattering* te analyseren. Tenslotte wordt er aangetoond dat het architecturale en algoritmische co-design van het hybride RF-akoestische systeem uitgewerkt in dit werk matuur genoeg is om verdere energie-neutrale 3D positionering te verkennen.

List of Abbreviations

ADC Analog-to-Digital Converter.

AoA Angle of Arrival.

APT Acoustic Power Transfer.

ASK Amplitude Shift Keying.

BER Bit Error Rate.

BLE Bluetooth Low Energy.

BPSK Binary Phase Shift Keying.

CDF Cumulative Distribution Function.

CMUT Capacitive Micromachined Ultrasonic Transducers.

COTS Commercial Off-The-Shelf.

DAC Digital-to-Analog Converter.

DAQ Data Acquisition System.

DoA Direction of Arrival.

ERP Effective Radiated Power.

ESR Equivalent Series Resistor.

FDMA Frequency Division Multiple Access.

FSK Frequency Shift Keying.

GBWP Gain-Bandwidth Product.

GNSS Global Navigation Satellite System.

IC Integrated Circuit.

IMU Inertial Measurement Units.

INS Inertial Navigation Systems.

IoT Internet of Things.

ISM Image Source Model.

LBS Location-Based Services.

LDO Low-Dropout voltage regulator.

LI Lithium-Ion.

LoPs Lines of Positions.

LoS Line-of-Sight.

LPS Local Positioning Systems.

MAE Mean Absolute Error.

MEMS Micro-Electromechanical Systems.

OOK On-Off Keying.

PCB Printed Circuit Board.

PMIC Power Management Integrated Circuit.

PMUT Piezoelectric Micromachined Ultrasonic Transducers.

PoA Phase of Arrival.

PPF Peak Prominence Factor.

R-LS Range-Based Least Squares.

RCS Radar Cross Section.

RF Radio Frequency.

RFID Radio-Frequency Identification.

RFPT Radio Frequency Power Transmission.

RIR Room Impulse Response.

RSS Received Signal Strength.

RSSI Received Signal Strength Indicator.

RT60 Reverberation Time 60 dB.

SDR Software-Defined Radio.

SNR Signal-to-Noise Ratio.

SOTA State Of The Art.

SPDT Single Pole Double Throw.

SPL Sound Pressure Level.

SR-LS Squared-Range-Based Least Squares.

STMR Side lobe To Main lobe Ratio.

SWIPT Simultaneous Wireless Information and Power Transfer.

TDMA Time Division Multiple Access.

TDoA Time Difference of Arrival.

ToA Time of Arrival.

ToF Time-of-Flight.

TWR Two Way Ranging.

UGB Unity Gain Bandwidth.

USRP Universal Software Radio Peripheral.

UWB Ultra-Wideband.

VLP Visible Light Positioning.

WASN Wireless Acoustic Sensor Network.

WILS Weighted Iterative Least Squares.

WLAN Wireless Local Area Network.

WPT Wireless Power Transfer.

WSN Wireless Sensor Network.

List of Symbols and Notations

Γ	Antenna load mismatch
σ	Radar cross section
α	Acoustic absorption coefficient
Δf	Frequency swing
γ	Sound source degree of directivity
$\hat{p}$	Polarization loss
Λ	Linear increasing and decreasing triangle function
λ	Radio Frequency (RF) or acoustic wavelength
$\langle s_c, s_c \rangle(t)$	Autocorrelation result of the linear chirps
$\mathbb{S}_N(X,Y)$	Similarity between two binary vectors
σ	Standard deviation
τ'	-3 dB bandwidth of the cardinal sine
$\underline{R}$	Acoustic reflection factor if a wall
$\underline{Z}$	Acoustic wall impedance
A_r	Antenna effective area
A_s	Structural mode of an antenna
C_{xx}	Self correlation function of real valued sequence x

C_{xy}	Cross correlation function of real valued sequences x and y
D	Antenna directivity
d_c	Critical distance
e_{cd}	Antenna radiation efficiency
f_a	Audio signal frequency
f_c	Carrier frequency
f_{clo}	Local oscillator frequency
G	Antenna gain
I	Sound intensity
max_2	2nd highest value of an array
$O[n]$	Complexity of a function
p_0	Standardized reference pressure of $2 \cdot 10^{-5}$ Pa
P_r	Receive power
P_t	Transmit power
RT_{60}	Reverberation time to -60 dB intensity
$s_c(t)$	Linear chirp signal
T_0	Start time of the audio signal broadcast
T_A	Wake-up time of the mobile nodes
v	Speed of sound in a medium
W	Power Density

Contents

Chapter 1

Introduction

This first chapter gives an introduction to indoor localization, its possibilities and challenges in a broader context. It further zooms in on the contributions of this PhD and formulates the addressed research questions and adopted methodologies. The first section addresses the context and opportunities of this research. In section 1.2, the necessary concepts and a fundamental background to comprehend this work are given, together with the challenges faced when designing an indoor positioning system. The research questions and methods to solve these questions are summarized in Section 1.3. Lastly, the outline of the book, including the contributions per chapter are presented.

1.1 Context and opportunities

1.1.1 Indoor Positioning in its Context

Digital technologies are increasingly adopted in diverse sectors to increment efficiency and to offer improved and new services. With the Internet of Things (IoT) technology having over 10 billion active devices, a massive number of common objects get an ID in the virtual world [1]. Ever more autonomous vehicles (from cobots to drones) handle these IoT devices. For many applications and services, in business, societal, and personal contexts, information about the position of these IoT devices is essential. Examples include finding people in emergency situations, localizing equipment and goods, offering context-relevant information and delivering proximity-restricted services.

For outdoor localization, the well-established Global Navigation Satellite System (GNSS) is used, where 20 cm accuracy can be obtained in Europe with the recently deployed Galileo System [2]. However, these satellite based systems have weak signals, making them susceptible to noise, reflections and interference and therefore inaccurate in dense and indoor environments where no direct line-of-sight with satellites can be maintained. To obtain the same level of accuracy and reliability, extensive research on indoor positioning technologies has been accomplished over the past decades. In Western society, persons spend over 85% of their time in indoor environments [Kle+01]. Expanding the localization of objects or users from outdoor environments to the indoors would enable seamless navigation, accurate and precise tracking and improved location based services.

Positioning in general can answer three questions: "Where am I?", "Where do I want to go to?" and "What can I do here?"

Where am I? Supplying a temporal sequence of location data of a person or object can answer the question "Where am/was I". Tracking systems can be divided into two parts: (I) monitor based systems, where a central entity collects data and calculates the position, or (II) device based, and more privacy oriented strategies, where the position is calculated by the mobile device itself. A myriad of tracking systems are already available in our everyday life with applications in real-time inventory processes, personal object finders, patient locators, etc. However, as became apparent with the COVID-19 outbreak of 2020, indoor tracking lacks the necessary scalability, accuracy and ease-of-use. Tracking is not limited to the real environment but can be extended to virtual space applications.

Where do I want to go to? The real-time display of self-localization in combination with spatial awareness enables indoor navigation. Here, the user or object gets guided along a route to the point of interest. There are a tremendous amount of applications in this research field, going from personal wayfinding in large buildings such as hospitals, universities and conference halls, optimal routing of unmanned vehicles in warehouses, to helping with urban and traffic planning.

What can I do here? Location based services is the generic term for applications that provide certain information or aid to the user based on the positioning data. Applications can be found in healthcare, mobile commerce, entertainment and work environments with examples such as proximity based payments at tolls, digital nameplates for art, augmented reality games, emergency call localization, targeted advertising. Privacy can be a major concern as user location data can be easily stored for longer time periods and shared without the user's knowledge.

1.1.2   Opportunities for Indoor Positioning

Localization and tracking can be either the primary objective of a business or an added value service to many other systems. With a global market expected to reach 28.2 billion dollars by 2024 [3], positioning, localization and navigation goes way beyond academic research and attracted the attention of large technological companies. The list for opportunities is ever-growing and can be categorized into societal, personal and business applications.

Societal

Societal applications of indoor positioning focus on the public prosperity and target a broad audience. They can help communal services to perform their job more adequately and improve response time in case of emergency, increase security or aid in the deployment of smart-cities. For example, in [Dep+18], the user's position together with predefined shortest paths to the nearest exit are used for indoor navigation in emergency building evacuations. Another emergency related example can be found in [FTW21], where the tracking trainees of the fire department in difficult visual conditions ensure their safety and efficient training. With the COVID-19 pandemic, the countermeasure *social-distancing* became a colloquial term. [Bar+21] shows which enhancements to indoor localization architectures are needed to ensure future, effective social distancing.

Personal

Next to its social purposes, smart environments could improve the quality of life on a personal level as well. Acclaimed examples are the aforementioned indoor navigation in large buildings and route optimization. Monitoring the location of persons at home as done in [Dek+17] enables ambient assisted living, and could enhance human well-being and security. These improvements can be more subtle and less invasive such as automatized indoor food delivery [Sun+19], smart object finding [Pos+22], sport analytics [Vle+21] and enhanced cultural experiences in museums and public places [SP20].

Business

Precise indoor positioning can revolutionize operations in Industry 4.0, health services, entertainment and marketing. Examples in Industry 4.0 can be found in asset management and tracking [Els+22; Rae22]. This corner stone of future manufacturing allows for better inventory and optimized operation management. In health services, patients, medicines, staff and critical equipment can be tracked and linked in emergency situations [Kon+18]. Location data is a valuable asset for navigation optimization and improved venue design in entertainment business.

In marketing, targeted advertising in stores and supermarkets can boost sales, prevent theft and monitor specific products.
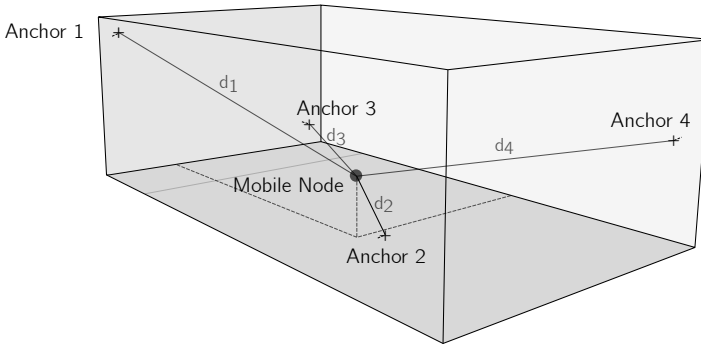
Figure 1.1: General architecture of an indoor positioning system with the minimum required anchors to perform a 3D position estimate.

1.2 Preliminaries

The design of a positioning system comes with a plethora of choices and dedicated terminology. What architecture is wanted, a centralized or a privacy oriented system? Do the mobile nodes need to be synchronized? What multiple access technique will be implemented to position several devices at the same time? How will the anchor and mobile nodes be deployed for optimal operation? What equipment is necessary, how can it be installed and what are the costs? What signal is chosen and what is its optimal design for precise and accurate measurements?

In the paragraphs above, the term *system* has been mentioned a couple of times already. A system in this work is an algorithmic and architectural co-design for indoor ranging or positioning.

In general, the architecture of a Local Positioning Systems (LPS) can be classified in two parts: (I) infrastructure, containing the necessary components to support the position estimation such as anchor nodes at known positions and a central processing system and (II) mobile nodes, whose location needs to be determined. A composition of such common, 3D architecture can be found in Figure 1.1. For 3D indoor positioning, at least 4, non-planar anchor nodes' with fixed, known

positions are needed.

Designing the algorithmic part of an indoor positioning system requires three phases [Ija+13], as depicted in Figure 1.2:

1. Deciding the physical quantity of the signals to be employed in measurements. Sound, RF, optical and magnetic signals are often used for indoor positioning, all with their own advantages and disadvantages.

2. Selecting the measurement method for these physical quantities. The signals from the previous phase will traverse the medium from transmitter to receiver. At the receiver, the physical quantities can be measured via different methods such as time (Time-of-Flight (ToF), Time of Arrival (ToA) and Time Difference of Arrival (TDoA)), Received Signal Strength (RSS), phase (Phase of Arrival (PoA)) and direction (Direction of Arrival (DoA)).

3. Choosing an appropriate algorithm to process the obtained measurements for the final location estimation. Distinction can be made between proximity, range, angle and fingerprinting [SGG08].

Physical Modality of Signals	Featured Measurement Methods	Algorithms for Location Estimation
Sound Radio Frequency Optical Magnetic	TOF DOA POA RSS	Lateration Angulation Fingerprinting
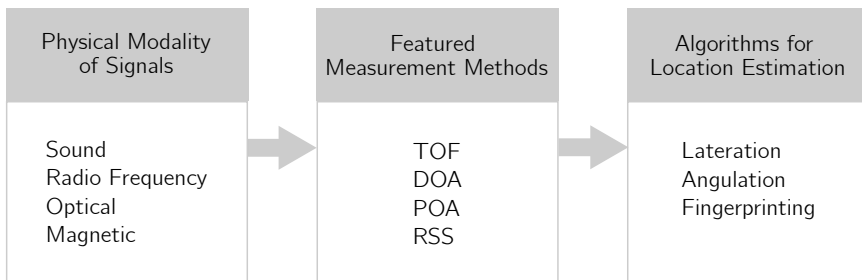
Figure 1.2: The three design phases for an indoor positioning system. Based on [Ija+13]

Figure 1.3 gives an overview of the geometrical and fingerprinting location estimation algorithms. Geometrical location estimation is done with angles or ranges. Ranges can be obtained from the RSS or the ToF measurement methods. Based on the distances, distance differences or angles, algorithms such as circular lateration, hyperbolic lateration and triangulation can be performed. In circular lateration, circles in a 2D (or spheres in a 3D) environment are drawn with the obtained range as radius and the known anchor point coordinates as center. The

intersection of these circles or spheres results in a position estimation of the mobile node. In 2D, at least 3 non-linear anchors are necessary to get an estimate. In 3D, this number increases to 4 non-planar anchors. Hyperbolic lateration uses the time difference of arrival to draw multiple two-sheeted hyperboloids. The estimate lies again on the intersection of these hyperboloids. In triangulation, or angulation in more general terms, lines are drawn in the direction of the calculated angle of arrival. The junction of these lines gives the calculated position. In fingerprinting, a measurement from a physical parameter is compared with a dataset gathered in an offline phase. Proximity based algorithms offer a coarse accuracy while being quite simple and inexpensive. Proximity evaluation is based on the connection stability between different anchors and the mobile node.
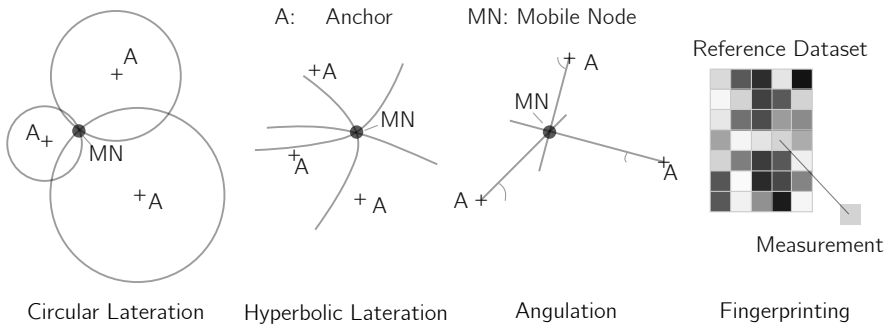
Figure 1.3: Geometric and fingerprinting algorithms for location estimation.

1.2.1 Constraints and evaluation

Depending on the application, different constraints in terms of cost, precision and accuracy, deployment, timing, security and energy efficiency are pushed forward [SVW22]. These constraints have an impact on each other, often in a negative way, e.g. the quest for improving accuracy and reliability of the position information leads to more complex processing, which logically counteracts potential power savings. Therefore, they form excellent parameters for the evaluation framework of indoor positioning systems [ZGL19].

Cost

From an academic point of view, highly expensive systems could be built to obtain the most accurate positioning possible. Although they could explore new

positioning techniques or gain information to overcome current obstacles in existing systems, a commercial adaptation would be implausible as a system is expected to be low cost and lack any high-end user devices. Extra hardware should be limited and when possible, Commercial Off-The-Shelf (COTS) components should be used to reduce the overall cost. Overhead expenses such as system maintenance and deployment in form of hardware, battery and software updates should be added to the total cost overview.

Precision and Accuracy

The localization precision and accuracy of an object or user is a key feature in a positioning system. Signals in indoor environments are prone to multipath effects and noise because of moving objects and obstacles, providing a challenging space to estimate positions. Extensive signal processing or noise reduction might be required to obtain an ideal sub 10 cm accuracy. Note that these two terms are intertwined but should not be confused, as precision is how close estimated values are to each other and accuracy is how close they measure to ground truth. A precise system can be inaccurate, i.e. constantly making the same, large error, and visa versa. Reliability and robustness are two terms that can be linked to precision and accuracy. Reliability can be described as the accuracy and precision over a longer time period, robustness as the ability to continue working properly when system errors or failures occur.

Deployment

There are several factors influencing the deployment of a LPS, with coverage and scalability the two most prominent. To allow for localization in large spaces, proper signal measurements should be obtained over the whole area. Interference and performance degradation due to the increasing distance are the main constraints for a wide coverage. Scalability is often associated with coverage, and addresses the effort it takes to increase the number of users or expand the positioning area. Multiple access schemes and protocols are necessary to connect this vast amount of users over the same medium with each other.

Timing

Timing in localization can refer to several measurable parameters: (I) the latency or delay is between obtaining the required data and the reported location, (II) the update rate between different location estimations or (III) the ability of different entities to operate at the same time or rate (synchronization). Most Location-Based Services (LBS) in business, societal and personal context require at a certain point, a real time position of a device or person. This means that within milliseconds, reference signals should be measured and a calculation performed.

Complex and time consuming signal processing techniques are thus often not viable and lower the linked update rate drastically. Errors in synchronization can lead to small errors in time resulting in large electromagnetic based positioning errors due to the speed of light.

Security and Privacy

To improve location based services and tracking systems, sensible positioning data about persons and objects is gathered. As any other data capturing service, they are vulnerable to data leaks and security attacks. Counteracting these attacks is often system specific and requires a thorough system evaluation to find the security holes and vulnerabilities [BEH18]. Unfortunately, indoor positioning has another privacy related issue from a user's perspective. To prevent that precise indoor positioning would lead to Orwellian scenarios, users should give their consent. Implementation of positioning systems should therefore not interfere with the user's privacy, e.g. signal reception in acoustic positioning systems should be processed immediately and not stored, as they can contain snippets of private information.

Energy Consumption

With the growing number of portable electronic devices, electric vehicles and large scale energy storage systems, the demand for batteries increases. It is predicted that by 2030, 11 million tons of e-waste will be generated from Lithium-Ion (LI) batteries alone [Roy+21]. With less than 6% of this e-waste being recycled, large amounts of LI batteries end up in landfills showing high human toxicity and terrestrial ecotoxicity potential [BSD16]. From this ecological perspective, the autonomy of positioning systems should be increased drastically by switching to energy-neutral positioning as epitome of battery waste reduction. Disruptive methods are needed to ultimately enable indoor positioning of energy-neutral devices, which can operate purely based on energy they harvest from their environment. Obtaining energy-neutral positioning would fulfill a deep-rooted ambition of localization solutions in retail, logistics and healthcare and facilitate a 'place-and-forget' implementation. The system would be low cost, a child's play to deploy and easily maintainable. Major influences on the energy consumption come from the update rate, the transmission power, the amount of transmission data, the awake time and computational complexity. By implementing low power communication technologies, decreasing location data, providing interpolation between positioning updates and offloading the localization calculations to the central, continuously powered server could minimize the energy drainage at the mobile node drastically.

Additional constraints

The cost, accuracy, deployment, timing, security and privacy and energy consumption are not the only parameters to evaluate a location based system. They, however, form challenges that have to be faced for adoption in future, smart environments. The list can be extended with the following additional challenges:

- Lack of standardization. At the moment of writing, there is no standard set of specifications as a guide for designing LPS, nor is there a single, ubiquitous technology pushed forward for future adaptations. This has lead to an excess of dissociated systems.

- Interference with other technologies. As positioning is often an extra service implemented in a smart environment, the negative impact on other services should be limited. For example, object finding with Bluetooth Low Energy (BLE) should not interfere with the transmission of health sensor data from medical devices to a mobile phone.

- Handovers. Due to lack of standardization and the different advantages of each system, future LPS should be heterogeneous and handover the positioning calculations to other technologies with ease. This should not be limited to indoor positioning only, and preferably extended to outdoor systems as well.

1.2.2   System Design Requirements

The main ambition of this PhD is to launch a disruptive and innovative integrated system approach with the potential of energy neutral, low cost and accurate indoor ranging. This integrated approach addresses the algorithmic and architectural co-design of a ranging system and goes beyond the construction of a hardware node and assessing it. Some system design requirements are quantified in Table 1.1 to open the door for 3D indoor positioning, additionally setting explicit goals for future evaluation.

1.3   Research Questions

The main research hypothesis in this work can be described by the following question: "Can a hybrid RF-acoustic indoor ranging system design achieve energy-neutral, low-cost and accurate ranging?". To answer this hypothesis, a divide and

Requirement	Quantified goal
Ranging accuracy	<10 cm in 80% of the ranging measurements
Energy consumption	<16.5 μJ/meas., which equals 5 y. of lifetime on a CR2032 battery
Cost	<€15 per mobile node with COTS components
Update rate	Static devices: 1 update/s. Dynamic devices: 10 updates/s.
Multiple Access	At least 10 nodes in the same room, at the same time.
Range	Up to 10 m

Table 1.1: Quantified requirements for the indoor ranging system design.

conquer approach is applied and the technological challenges and system co-design requirements of this indoor ranging approach are refined to the following set of research questions:

Q1 What technology can be used to design an energy-neutral, low cost and accurate ranging system?

Q2 How do environmental factors impact the system performance and what improvements can be carried out to counter these negative effects?

Q3 How can a ranging accuracy below 10 cm be achieved with energy-constrained measurements?

Q4 How can energy-neutrality be achieved at the mobile node?

Q5 How well can a mobile node be located when the ranging system is expanded to a 3D environment?

1.4 Contributions, Thesis Outline and Research Methods

The most prominent objective of this work is to design and research a disruptive and innovative approach for indoor ranging. This should be an algorithmic-architectural co-design where the most critical system elements are validated in a step-by-step approach.

Next to this first introductory section in this book, there are six additional chapters. Contributions to these chapters come from different journal and conference papers

published during the different years of working on this PhD. These scientific reports are mentioned in the beginning of each chapter. Chapters are composed of an introduction, detailing the contributions and putting each chapter in its context. The introduction is followed by research in the form of a dedicated literature review, theory, simulations or experiments performed in realistic environments. Each chapter is terminated with a conclusion, giving an overview of the accomplished research and connecting it with the other chapters. A graphical overview of these chapters can be found in Figure 1.4.

The remainder of this introduction shows the scientific contributions of each chapter.

1.	Introduction
2.	Positioning of Energy-Neutral Devices
3.	Ultrasonic Signaling with COTS Components

4.	Hybrid RF-Acoustic Ranging	5.	RF-Based Communication and Energy Provision

6.	Towards Hybrid RF-Acoustic 3D Indoor Positioning
7.	Conclusions and Outlook
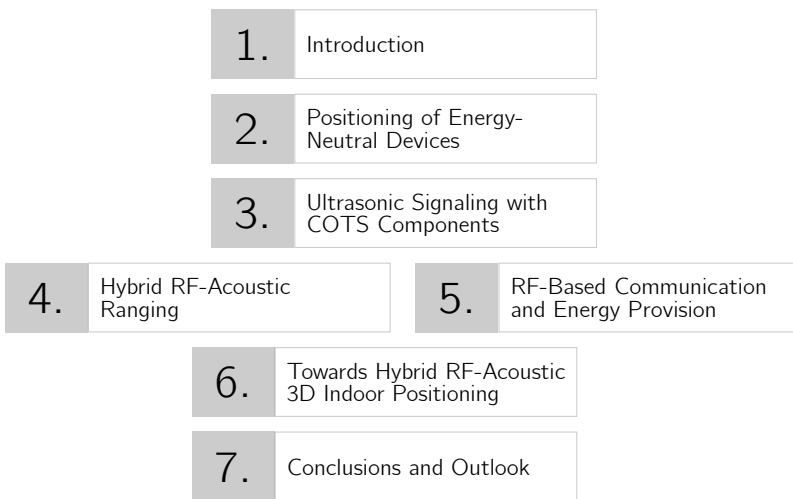
Figure 1.4: An overview of the different chapters and the overall structure.

Chapter 2 - Positioning of Energy-Neutral Devices. In the second chapter, a positioning technology is selected, based on a comparative literature study and the recommended system design requirements. The focus in this chapter lies on a key challenge in indoor positioning: the energy consumption at the mobile node. **Chapter 3 - Ultrasonic Signaling with COTS Components**. An introduction on environmental and hardware restrictions in the acoustic, ultrasonic domain are given based on theory and experiments. These will steer certain design decisions of the system concept. The main contribution consists of the assessed measurements regarding ultrasonic hardware. **Chapter 4 - Hybrid RF-Acoustic Ranging** In this chapter, the state-of-the-art

hybrid ranging system concept is introduced, together with the theory of the applied broadband pulse compression technique. Simulation-based assessments on both the influence of noise and room reverberation in the acoustic domain are performed, followed by accuracy enhancement methods. An initial experimental validation shows the potential of this proposed method. The last part of this chapter describes the system energy consumption optimization by means of hardware elimination and data reduction. For this optimization, experiments were conducted in a real life scenario as well. The main contributions in this chapter are the innovative system design, conducted simulations and experiments.

Chapter 5 - RF-based Communication and Energy Provision. The work done here runs parallel with Chapter 4 and consists of two parts, both connected to the RF signals of the hybrid ranging system. The first part proposes RF backscattering as a low-power communication solution. The necessary background is expanded with related research on modulation and demodulation schemes for COTS components. The second part consists of a practical assessment of RF energy harvesting to enable complete energy-neutrality within the European regulations.

Chapter 6 - Towards Hybrid RF-Acoustic 3D Indoor Positioning. In Chapter 6, the research results from Chapter 4 and 5 are combined, resulting in a hardware implementation and related power consumption analysis. Experiments demonstrate the opportunities and challenges for hybrid RF-acoustic ranging in both domains and a final measurement campaign evaluates the ranging capabilities for 3D indoor positioning.

Chapter 7 - Conclusion and Outlook This work is concluded with a review of the conducted work and an outlook for advances in hybrid RF-Acoustic based positioning.

Chapter 2

Positioning of Energy-Neutral Devices.

This chapter is adapted from:

- Cox, B., Buyle, C., Delabie, D., De Strycker, L., Van der Perre, L. "Positioning Energy-Neutral Devices: Technological Status and Hybrid RF-Acoustic Experiments.", 2022, Future Internet 2022, 14, 156. doi: 10.3390/fi14050156 [Cox+22]

Contributions: Coordination and the methodology were conducted by the author. The sections from the paper adopted in this chapter contributed to the state-of-the-art research and energy neutral conceptualization. Both were drafted by the author and co-authors.

In the first chapter, the three phases of designing an indoor positioning system were introduced. Deciding on the physical quantities and measurement method has an impact on several evaluation parameters. In this chapter, a comprehensive overview of these technologies for indoor positioning is given together with their linked (dis)advantages. With energy consumption having a prominent place in this work, a more in depth review is made on the appropriate technologies. A final indoor ranging technology is chosen based on the system design requirements.

The remainder of this chapter is organized as follows. Section 2.1 gives an introduction to different physical signal quantities that are suitable for accurate indoor positioning in combination with a wide coverage. The next section comprises

a state-of-the-art literature review for energy-neutral positioning. In Section 2.3, it is stated why Hybrid RF-Acoustics is chosen as key technology. And lastly, a short conclusion is made.

2.1 Positioning Technologies

Indoor positioning is made possible through several technologies, each with their own accuracy, coverage, advantages and linked applications. In the last couple of years, several overview papers, with some having over 300 references [Ogu+18], reviewed the vast amount of positioning papers available in current literature. With subjects going from system requirements like robustness [Cad+16] and accuracy for mobile targets [Tah+16] to dedicated positioning methods like fingerprinting [HC16], positioning systems are classified from different points of view. In this section, an overview is given from a technological perspective. For indoor positioning targeting the proposed accuracy below 10 cm and coverage over 10 m there are three main candidates, depicted with color in Figure 2.1, RF-, acoustic- or optic-based systems.
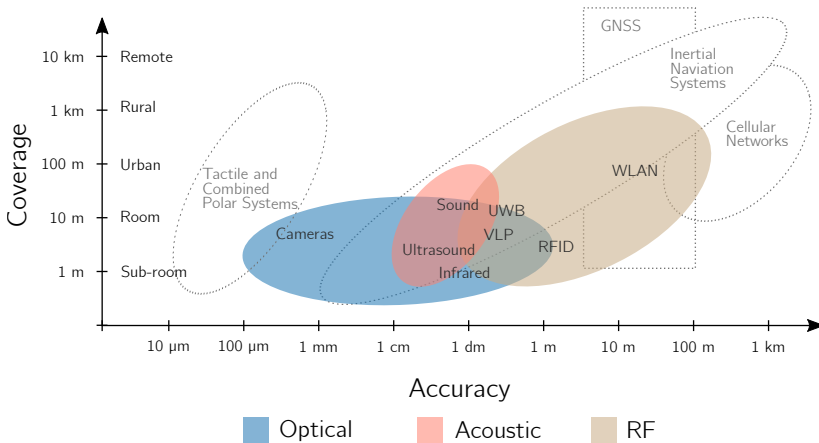
Figure 2.1: Overview of different technologies for indoor positioning, showing their coverage and localization accuracy. Adapted from [Ure+18].

2.1.1 Radio Frequency

Within the RF technology, a couple of wireless communication protocols (Radio-Frequency Identification (RFID), UWB, Bluetooth, WLAN) are adapted for positioning. The measurement methods listed below give an overview of how these protocols exploit the physical properties for localization purposes.

- RSS: with no extra hardware, bandwidth or energy costs, this is a simple and efficient positioning method. Through Friis transmission formula [Fri46], an elementary relation between received signal strength and distance can be derived, with influences of the transmitted power, antenna gains, polarization and directionality. However, the distance estimations have only a coarse accuracy as it is difficult to include detailed environmental influences on this path loss model [SGG08]. RFID, Bluetooth and Wireless Local Area Network (WLAN) systems often adopt this measurement method.

- ToF: With the constant speed of electromagnetic waves, the distance between two antennas can be calculated by measuring the travel time of the signal. The term Time-of-Flight comprises both time-related ToA and TDoA methods. In ToA systems, this time of flight is measured between the transmitter and receiver, imposing both to be synchronized. In TDoA, only fixed anchor nodes are synchronized, measuring the time difference between two or more received signals. With their known position, hyperbolic lateration can be performed. Perfect synchronization can be a major hurdle, as an inaccuracy of 3.33 ns leads to a 1 m ranging error. In Two Way Ranging (TWR), only the transmitter needs a high speed clock, measuring the round trip time between the start of a signal transmission and the reception of the signal that was retransmitted by the receiver. For ToF systems, Ultra-Wideband (UWB) technology is often used, with a high ranging resolution and exploiting the large bandwidth properties for signal shaping, link quality optimization and Line-of-Sight (LoS) component detection.

- Angle of Arrival (AoA): The phase delay phenomenon when receiving an RF signal with multiple antennas in an array or other configuration can be exploited to calculate the transmitted signal direction. For 2D systems, this is referred to as AoA. For 3D configurations, it is called DoA. The array configuration depends on the application, but $\lambda/2$ spacing is often used to prevent phase ambiguities. The AoA estimation algorithms can be classified as non-parametric, where no assumptions on the statistical properties of the signal are made or as parametric, where these assumptions are made. In the first class, a beam is steered over all directions, creating a spatial

spectrum where the received power is shown in function of the direction. In the second class, only specific areas are selected to steer to.

- Fingerprinting: In all of the above techniques, fingerprinting can be used to include the influence of real-life channel effects on the measurements. Measurements are matched to a reference dataset collected in an offline phase. Gathering this dataset is often labor intensive, requires update with changes in the environment and is often not detailed enough for precise localization. In RF, RSS data is most of the time combined with fingerprinting, as this RSS data is often available as a feature in wireless sensor networks.

The largest drawback of radio frequency based systems lies in their susceptibility to indoor multipath effects such as reflections, scattering, diffraction, refraction and absorption [SGG08]. These effects can be considered as random events in geometric LPS with constructive and destructive interference influencing the RSS values and propagation path alterations effecting the ToF and DoA parameters. Accurate systems require a large bandwith having a negative impact on the energy consumption. Another drawback of these RF-based systems is the high propagation speed, requiring exact synchronization in time based systems.

2.1.2   Optical

Optical based systems use the part of the electromagnetic spectrum where the waves are (partly) visible for the human eyes. In current developments, two main research fields can be classified: (visible) light and computer vision based positioning.

(Visible) Light Positioning

Transmitters in light positioning systems are commonly LEDs, positioned at the ceiling and emitting modulated light signals. When visible light is used as an information carrier for positioning, the term Visible Light Positioning (VLP) is used in literature. Receivers can consist of a photodiode used individually or in a constellation, a camera/image sensor or a quadrant photodiode. For positioning purposes, several transmitters are necessary using the medium. For this reason, multiple access schemes in time, frequency or code are used. The greatest advantage of light signals over their RF counterpart is the relative immunity to multipath effects. However, they require a direct LoS between transmitter

and receiver, limiting this localization technique to short range, and mostly, indoor applications. VLP-systems are commonly subdivided by their receiving characteristics.

- RSS: just like in RF systems, these are widely adopted due to their low-complexity receivers. The short wavelength of light makes it considerably more immune to multipath fading than its RF-based equivalent. The signal strength itself depends on the transmitted optical power, the radiation pattern of the transmitter, the effective area of the photodiode and the Euclidean distance between these latter two. An important advantage is that there is no need for time synchronization when Frequency Division Multiple Access (FDMA) is used, and the RSS values can be directly measured [Ver21].

- ToF: ToF strategies in VLP have similar properties as those in RF. ToA is hard to implement in VLP systems, because of the required precise synchronization between transmitter and receiver. In TDoA systems, the transmitters instead of the receivers need to be synchronized since the time of flight differences between two transmitters are calculated in a CDMA or FDMA setup. At the receiver side, high sampling rates are required and the time resolution determines the maximum ranging accuracy.

- AoA: compared to the RF counterpart, the LoS dependency of VLP makes the use of AoA more advantageous. No synchronization is required between transmitter and receiver. However, a simple photodiode cannot calculate the incoming angle and common implementations use photodiode arrays, quadrant photodiodes, and image sensors.

In [RLW20] a summary of different VLP based systems is given. This summary shows that for small scale setups ($< 1.2\,\text{m}^2$), sub centimeter accuracy in 2D space can be obtained. In more realistic and large scale scenarios, the error increases between sub-decimeter to meter level in a 3D environment.

Camera-based Visual Positioning

In fixed camera-based positioning systems, an object in the camera image coordinate plane is mapped to a local area coordinate plane using planar homography [Tsa87] and further to a geographic plane. This transformation requires additional depth information about the positioning area which can be provided by 3D models, stereo camera systems and laser-scanners [MT11]. Another

hurdle in these systems is the need to isolate the object to position from their surroundings. In the past, background subtraction algorithms were used, but these lack accuracy in dynamic conditions. With the recent advances in machine learning, deep learning is a more promising solution for object detection and tracking. With these algorithms, a mean positioning error below 20 cm is possible [Par+21].

2.1.3 Acoustics

Acoustic based systems use sound and ultrasound to position a target. Depending on the application, the acoustic transmitters can be positioned at the anchor side or at the mobile node. The latter enables device free positioning of persons and objects broadcasting audible sounds. There are three measurement methods used in acoustic positioning:

- ToF: compared to light and RF signals, the propagation speed of sound is around 880 000 times slower, enabling more accurate results with less stringent synchronization. E.g. a synchronization error of 3 ms has the same 1 m ranging error as in the previous example. ToA is viable in acoustic positioning, but still needs the transmitter and receiver to be synchronized. Unlike ToA, TDoA can be used to localize unsynchronized sound sources, as long as the receivers are synchronized. However, this propagation speed is dependent on the temperature, and can create decisive errors when left unmonitored.

- DoA: In acoustic based systems, DoA is calculated with time differences instead of phase differences. The least computational intensive systems simply calculate the time lag between the signals received by two microphones by using cross correlation. Increased accuracy can be obtained by combining microphone pairs. Other techniques consist of delay and sum beamforming where a virtual, directional microphone can be steered to locations of interest, steered response power and the more complex spectrum based beamforming.

- Fingerprinting: with fixed transmitters sending out known acoustic signals, a fingerprinting method where measured acoustic signals are matched to a dataset gathered in an offline phase, can be implemented.

Although it is possible to measure the sound intensity with microphones for RSS based positioning, this method is not included in the list above. As will be explained in the next chapter, it is challenging to determine the attenuation of a sound source and in both the audible and ultrasonic domain, there is a lot of interference

of other sources. For passive, device free sound localization, RSS is not viable at all, since the initial transmit power and signal shape are unknown. RSS for sound signals is, in contrast to the common available RF technologies, an improved method for room presence detection.

2.1.4 Evaluation Parameters for Indoor Positioning

Table 2.1 summarizes the aforementioned physical quantities and positioning techniques, accompanied with the main sources of review papers and evaluation parameters to rely on when selecting a suitable solution for a new or existing setup [Ogu+18]. The selected evaluation parameters are shortly discussed here.

Scalability from a system level perspective is how well the LPS can endure system extensions on both geographical and node density level. Entities in this system should not interfere with each other and system stability should be maintained.

Accuracy and precision defines how well the estimated position approaches the actual position. Precision indicates the repeatability of a measurement. In positioning systems, the accuracy is often given by the Euclidean distance between the measured and actual position.

Complexity depends on the amount of parameters in hard-, software and operating factors that have to interact with each other.

Robustness describes the ability to continue working when errors or failures in hard-, software or positioning occurs. It goes hand in hand with complexity and physical parameters in real life systems.

Reliability defines how well the system performs within a certain, predefined accuracy and precision for a longer time and/or in certain areas.

Energy Efficiency from a node perspective. As most mobile nodes in LPS do not have a mains connection and e.g. operate on a battery, data processing, communication and the overall active time should be kept to a minimum.

Cost should include all the expenses made to buy, roll-out and maintain the positioning system.

2.1.5 Hybrid technologies

In well-composed hybrid positioning systems, two or more technologies or measurement methods are combined in a way that the advantages add up and overrule the disadvantages. Hybridization comes with an increased system complexity, even if different methods within a single technology are chosen. Existing systems often combine the aforementioned technologies with Inertial Navigation Systems (INS), making use of Inertial Measurement Units (IMU) such

Physical Parameter	Main Source(s)	Location Identification Technique	Typical Accuracy	Scalability	Complexity	Robustness	Reliability	Energy Efficiency	Cost
Light	[RLW20]	AoA, ToF RSS	<40 cm	Poor, 3D	Moderate	Low	Moderate	Low	Moderate
Computer Vision	[Par+21]	Homographic Mapping	<50 cm	Poor, 3D	Moderate	Low	Moderate	Low	High
RF	[ZGL19] [MTH19]	AoA, ToF RSS, Fingerprint	<10 cm to 5m	Good, 3D	Low	Low - High	Fair	Moderate to High	Moderate
Sound	[Ure+18] [Ija+13]	AoA, ToF Fingerprint	<10 cm	Poor, 3D	High	Low	Moderate	High	Moderate
INS + RF	[Jin+14]	RSS Fingerprint + Tracking	<1 m	Good, 3D	Low	Moderate	Moderate	Moderate	Low
INS + RFID	[FR09]	Fingerprint + Tracking	<1 m	Good, 3D	Low	Moderate	Fair	High	Low
UWB + RFID	[Fab+20]	ToF	< 10 cm	Poor, 3D	Moderate	Low	Fair	High	Moderate
RF + Sound	[Hol09]	ToF	< 10 cm	Moderate, 3D	High	Low	Moderate	Moderate to High	Moderate
Light + Sound	[FHP98]	ToF	< 10 cm	Moderate, 3D	High	Low	Low	Moderate to High	Moderate

Table 2.1: Overview of positioning techniques and the selected evaluation metrics. Adapted from [MTH19] and [Ogu+18]

as gyroscopes and accelerometers to track the position and angular motion from an initial starting point, angle and velocity. The systems described in literature are added to Table 2.1. Their advantages, possible challenges and drawbacks are specified here.

INS + RF RSS + Fingerprint uses the tracking feature of the IMU to optimize correct matching in systems where RSS variation is low. Machine learning algorithms can be used to improve this matching process even further [Jin+14]. An initial position is still required and drift and cumulative errors can decrease the accuracy drastically.

INS + RFID again make use of the IMU for tracking the object when there is no coverage by the RFID readers [FR09]. This system has similar disadvantages as the previous described hybrid method, but has a lower power consumption due to the passive RFID tags.

UWB + RFID exploits the backscattering communication capabilities of RFID with UWB signals. This enables ToF measurements, having an improved accuracy with passive tags but decreases the range and coverage to 2.5 m maximum [Fab+20]

RF + acoustic combines the best of both worlds, using the slower propagating acoustic signals for positioning purposes, obtaining cm accuracy and exploiting the RF signals for synchronization and communication. This still requires acoustic LoS and a larger bandwidth in both acoustics and RF and is sensitive to noise in the two domains instead of one [Hol09].

Light + acoustic has similar advantages and disadvantages as hybrid RF-Acoustics, but requires LoS in both light and acoustic domain [FHP98].

2.2   Positioning of Energy-Neutral Devices

A sought-after feature in many applications is interaction with energy-neutral devices. Energy-neutral operation creates the opportunity to eliminate the need for a battery in a device which in turn reduces the cost and maintenance and enables a small form factor. Furthermore the localization possibility of the device could theoretically be extended to an unlimited lifetime since the harvesting of the necessary energy is inherently present. In indoor positioning, device free positioning is only possible with a couple of technologies (camera based and acoustic systems). With unknown signals and random timing intervals, these systems need a high processing power and lack the necessary accuracy for most applications. In this section, energy-neutrality is defined followed by an overview of the current State Of The Art (SOTA) of device based, indoor positioning techniques for a limited energy budget at the positioning object.

2.2.1 Interacting with Ultra-Low Power and Energy-Neutral Devices

Before reviewing the current SOTA, a detailed definition of an energy-neutral, an active and a passive device needs to be given. In this work an energy-neutral device is defined as a passive or active device with a guaranteed continuity of use by means of a Wireless Power Transfer (WPT) or energy harvesting link that offers the ability to provide sufficient energy (see Figure 2.2). In other words, the device experiences no net negative effect on its potential energy resources from its harvesting (E_{in}) and consumption operations (E_{cons}). An active device contains an internal energy buffer such as a battery, (super)capacitor, etc. while a passive device contains no such internal energy buffer and depends entirely on the momentary WPT or energy harvesting link. Since the energy used is equal to or less than the energy received, the device can be defined as an energy-neutral device. An energy-neutral device is classified under low-power devices, given the low power consumption. A low-power device may have a net negative value if the consumed energy is larger than the incoming energy. In that case, a larger energy storage is needed that must be replaced after a certain time.
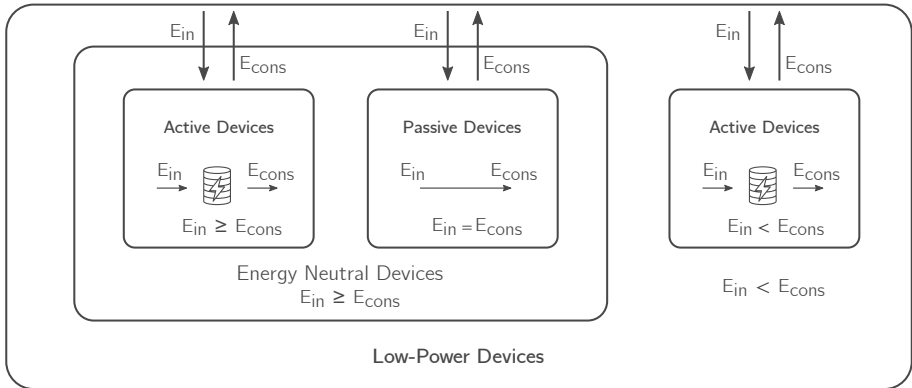
Figure 2.2: Graphical overview of the low power devices classification with both active and passive devices in energy-neutral devices.

Energy can be harvested from a variety of sources and through different techniques [Adu+18], and recently solutions are also designed specifically for small IoT devices [Mag+17; La +19]. In view of the objective to position size-constrained devices indoors, solar energy is typically not a viable option. Coupled inductive power transfer is a very efficient solution for wireless charging in close

proximity of devices reaching $> 90\%$ efficiency, yet the coupling deteriorates rapidly over distances larger than a few centimeters. Harvesting mechanical energy can only be relied on if devices are repeatedly and significantly moving, and if the form factor of the device allows the integration of a rather bulky harvester. Acoustic Power Transfer (APT) is considered for reaching devices where inductive or RF transfer is prohibited, e.g. through human skin for biomedical implants or when metallic surfaces obstruct RF waves [Awa+16]. However, the power density is low ($< 0.1\,\mathrm{nW\,cm^{-2}}$) [Awa+16] and the conversion to electrical energy requires large transducers with rather low efficiencies.

In recent years, Radio Frequency Power Transmission (RFPT) has received significant interest as radio waves offer the advantage of being ubiquitous, and hence energy can be obtained over a large area, even in inaccessible places. RF energy has a density varying between $0.2\,\mathrm{nW\,cm^{-2}}$ and $1\,\mathrm{\mu W\,cm^{-2}}$ [CAK19]. Practically, this results in a received power in the range of µW at the size-constrained sensor or actuator node. This makes RF harvesting highly suitable for remote powering small devices from a distance of several meters in indoor environments. Still, since the total amount of energy that can be transferred is very limited, innovative approaches for the positioning of these devices need to be developed.

2.2.2 Emerging Energy-Neutral Indoor Positioning Systems

In regard to Table 2.1, only a couple of technologies are viable for potential energy-neutral positioning. In what follows, a short overview of developments and technologies that are adopted to reduce energy consumption per (hybrid) physical quantity is given. Table 2.2 shows a comparative summary of state-of-the-art, low-power indoor positioning systems for the different technologies. A check mark (✓) is given to systems consuming less than $100\,\mathrm{\mu W}$.

RF

RFID is currently the most mature and deployed technology for positioning energy-neutral devices. Hereby, the RF signal is used for activating and positioning the device at the same time. A backscattering mechanism is used, altering the characteristics of an incident RF wave based on some unique parameter(s) of the passive device. This technology offers an elegant and low-complexity approach. However, the accuracy of RFID localization systems is defined by the limited

read range, and false or missed detections occur due to multipath [Wit+16]. In [Gom+22], an overview is given of current RFID positioning systems, dividing them in three classes based on the underlying positioning technology. For Received Signal Strength Indicator (RSSI) based systems, the accuracy is very limited, in the order of meters for larger distances, and the reliability is strongly affected by multipath effects and tag orientation [EDP10; SN11]. For smaller distances, sub-decimeter can be achieved with machine learning algorithms using extensive data sets [Gom+22]. PoA methods typically show a better localization accuracy, but currently suffer from two main issues: ambiguity due to phase periodicity and phase offset [DM14].

From section 2.1.1, it is clear that the most promising RF technology that meets many quality metrics for indoor positioning is UWB-signaling based. The high bandwidth enables great resistance against multipath fading and consequently makes UWB highly attractive for indoor environments. The average power consumption of commercial UWB systems depends on the device mode, but even in idle mode, this value, which is heavily influenced by the design, is larger than 5 mW [Flu+20]. There is still room for lower power design optimization for this technology. In order to coexist with narrowband system architectures, the spectral power density in UWB is limited to -41.3 dBm/MHz by regulations. Unfortunately, this is insufficient to power UWB tags remotely at useful distances [CCF13; CCF12; Fab+20]. The latter in combination with the higher power consumption makes the design of an energy-neutral UWB tag for long range indoor positioning practically impossible at the time of writing.

Light

With photodiodes only consuming a couple of µW and with light sources where photovoltaic panels could harvest light from, VLP systems could be an ultimate low-power and even energy-neutral positioning system. However, precise positioning is obtained with ToF techniques, with the obligatory synchronization and linked sensitive hardware and energy consuming precision timers. Communicating the signals back should be instantaneous and would require too much energy. In VLP systems the term passive is often referred to as: *not requiring explicit intervention of the user* [MH21]. An overview paper [SR20] of these passive VLP systems divides the current literature in three classes: (I) fully passive systems where the transmitters are sending out unmodulated light and receivers are spread across the room to detect changes due to shadows. (II) In passive user systems the light is modulated and the reflected signals on a passive user are received by spatially

dispersed receivers. Due to the LoS restraints, these passive devices should be reflective and directly reflect the signals to the receivers [Wan+20b]. (III) Passive sources use smart materials such as polarizers, LCD and birefringence material to alter the incoming light and reflect them back to receivers [Yan+15].

Acoustics

Power consumption in acoustic LPS has come a long way since groundbreaking systems like Cricket and Active Bat [Har+02; Pri05] with current, cutting-edge Micro-Electromechanical Systems (MEMS) based transducer chips consume less than 100 μW [Wan+22]. Since receiving acoustic signals consumes less power than transmitting, mobile nodes are often equipped with broadband low power MEMS microphones [TOD17] or narrowband Piezoelectric Micromachined Ultrasonic Transducers (PMUT) [Wan+21]. In these systems, the received acoustic signals can not be transmitted back and processing is done at the mobile node, adding to their power consumption. In highly reverberating situations, optimizations to improve accuracy such as Doppler compensation [Agu+20], likelihood expressions [Ogi21], or additional anchor nodes to increase spatial diversity [Man+19; WS17], are not feasible on these local processors. Smartphones are often used as mobile nodes in acoustic localization systems since they are widespread and have a built-in speaker, microphone and sufficient computing power [Che+19; Cao+20]. However, these are not low-power devices and are not designed to deal with ultrasonic sound signals as the audio components are usually limited to the audible region given their primary functions. Moreover, RF-based positioning for smartphones is more straightforward, given the presence of appropriate antennas.

Hybrid RF-acoustic positioning

Early hybrid positioning systems adopted the RF signal for both synchronization and communication. A previous overview paper from Holm et al. [Hol09], bundles these first generation RF-acoustic positioning systems. Although the energy efficiency of wireless acoustic sensor nodes has progressed significantly by the developments in MEMS and Capacitive Micromachined Ultrasonic Transducers (CMUT) microphones and low energy computing, current hybrid RF-acoustic solutions have not achieved fully energy-neutral operation for long range (>10 m), centimeter-accurate and multiple access operation, with RF communication as the main limiting factor to achieve this [Li+19]. Active low power wireless standards like Ant+ [Car+17; Car+19] achieve long range but are still power hungry, taking

Technology	Reference	Technique	Accuracy [cm]	Ultra-low power	Energy harvesting
RFID	[EDP10]	RSSI	75	✓ (passive)	✓
	[SN11]	RSSI	10	✓ (passive)	✓
RFID/ML	[Gom+22]	RSSI	5	✓ (passive)	✓
RFID/odometry	[DM14]	PoA	4	✓ (passive)	✓
UWB	[Zwi+15]	TDoA	11.4		
	[Flu+20]	ToA	13.2	✗ (6.6 mW idle)	
UWB/RFID	[CCF13]	ToF	<10	✓ (passive)	✓
	[Fab+20]	ToA	<50	✓ (passive)	✓
Acoustic	[Man+19]	TDoA	22		
	[Che+19]	TDoA	20		
	[Wan+22]	TDoA	3	✓ (100 µW)	
	[Wan+21]	TDoA	<0.5		
	[Ogi21]	ToF, TDoA	<24		
RF-Acoustic	[MSD13]	ToF	<1	✗ (150 mW)	
	[Car+17]	ToF	<0.2	✗ (21.7 mW)	
	[Rek+21]	ToF	<1	✓ (passive)	✓
	[ZS13]	ToF	13	✓ (81 µW)	✓
	[Mer+21]	ToF	5		
	[Car+18]	TDoA	<0.5	✗ (26.4 mW)	(✓)

Table 2.2: Comparative summary of low-power indoor positioning systems.

up a large part of the energy budget in energy-constrained devices. RFID, although being passive and making use of energy harvesting, still has a limited reading range for communication [ZS13; Car+18] or synchronization [Mer+21]. A promising hybrid method makes use of the backscattering technology refined in RFID systems, and inspired by the *Great Seal bug*, where passive hybrid RF-acoustic signaling was used in the cold war to eavesdrop the American embassy. In [Rek+21], the acoustic signal coming from a CMUT transceiver is modulated around the carrier, making it vulnerable to self-interference and prohibiting multiple access when several mobile nodes are present.

2.3 Hybrid RF-Acoustics as Chosen Indoor Ranging Technology

The previous section showed that there are only four technologies of interest that have the appropriate accuracy and range while maintaining a low energy consumption: acoustics, UWB, RFID, and hybrid RF-Acoustics. A visual
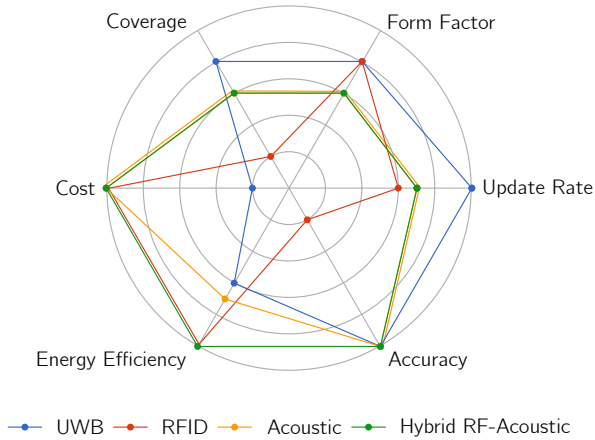
Figure 2.3: Radar plot of different energy-neutral, indoor positioning technologies with quality metrics.

comparison between the quality metrics of these technologies is given in the radar plot in Figure 2.3. The area of one such radar plot indicates how well the technology scores on the given parameters. This narrows the suitable technologies further down to hybrid RF-acoustic and UWB. When matching them with the system design requirements drawn up in Section 1.2.2, the cost and energy efficiency of the UWB impairs its application within this PhD. For hybrid RF-acoustic, state-of-the-art research in [Rek+21] shows that energy neutrality can be achieved for limited ranges when ToF is adopted. In the following chapters, research will be done on such ToF-based, hybrid RF-acoustic indoor ranging system. As there are two physical quantities to be measured, major hurdles will be the ranging accuracy and precision for the proposed range, low-energy consumption in combination with COTS components and multiple access in both the RF as in the acoustic domain.

2.4   Conclusion

A wide range of indoor positioning technologies, based on different physical signals, is available today. For accurate and room sized coverage, acoustic, RF and optical systems are the go-to solutions, having their own pros and cons. Hybrid

technologies can combine the best of both worlds enabling overall better performing systems.

With the positioning of energy-neutral devices being a sought after feature, it is clear that only a couple of technologies could enable this form of indoor positioning. The timing constraints in light and RF systems and the higher power consumption for long-range distance measurements in acoustic systems make these technologies less preferred. The conducted state-of-the-art research shows that energy neutrality can be achieved with hybrid RF-acoustics, making them the perfect indoor ranging candidate based on the proposed system design requirements. In hybrid systems, the signals are present in two different media, being twice as sensitive to noise and interference, potentially consuming more energy because of the dual signal reception and retransmission and having to support multiple access for both acoustic and RF signals. The next two chapters will dive deeper in to these constraints, with the focus on acoustic signals.

Chapter 3

Ultrasonic Signaling with COTS Components.

With hybrid RF-acoustics chosen as technology for accurate, low-power indoor positioning, a more in-depth review on the impact factors on the accuracy is given in this chapter. The focus lies on the acoustic signals, as they embed the necessary ranging information. The first section shows the need for broadband signals and ideal signal modeling for optimal acoustic ranging. Section 3.2 summarizes constraints when transmitting sound signals in real-life environments. A first part in this section addresses the acoustic scene and channel effects to fully comprehend signal propagation in simulations and real-life environments. The second part introduces the chosen acoustic simulation environment. The main scientific contributions are given in Section 3.2.3, where measurements were conducted regarding the directionality of ultrasonic speakers and MEMS microphones together with frequency responses of the speaker and microphone pairs. These hardware restrictions come with implications for the energy-neutral devices, as can be read in Section 3.3

3.1 From narrowband systems to spread spectrum techniques

A first generation of hybrid LPS exploiting the slower propagating acoustic waves originates from around the turn of the century. By combining the mechanical

wave with an electromagnetic wave, a reference timing signal is used in the form of light [FHP98] or RF [Har+02; Pri05]. With this synchronization signal, the ToF of the acoustic signal can be easily calculated at the mobile node and used to estimate the position. These systems used narrowband, piezoelectric transducers, emitting single frequency ultrasonic signals. At the receiver, processing was limited to an envelope based signal detection. This latter has a couple of drawbacks, such as low accuracy, low robustness against in-band noise, low update rate and limited multiple access mode.

Driven by the technological progress of (acoustic) hardware, i.e. MEMS microphones and low-power microcontrollers, broadband system designs begin to develop from the mid 2000s. Spread spectrum techniques from radar systems were applied on acoustic signals [HW02; Pri+09]. By encoding the acoustic signal, the narrowband problems were overcome, improving the Signal-to-Noise Ratio (SNR) and sensitivity, detecting overlapped echoes and enabling simultaneous transmission. However, additional hardware is required at the receiver side such as an Analog-to-Digital Converter (ADC), converting the broadband acoustic signal into a digital, processable bitstream, and a microcontroller correlating the digitized signal with stored codes, increasing the power consumption. To improve the accuracy and robustness even further, extended research is performed on the encoding of the transmitted signal. According to [SP80], an optimal set of codes has two features:

1. Self correlation should approach the Kronecker delta function [Kro68].
2. Cross correlation with other codes should be zero.

For the real valued sequences x and y of length N and with $C_{xx}[n]$ the cyclic autocorrelation function and $C_{xy}[n]$ the crosscorrelation function, this can be rewritten as:

$$
C_{xx}[n] = \begin{cases} \sum_{k=0}^{N-1} x[k]\,x[k+n] = 0, & 0 < n < N \\ \sum_{k=0}^{N-1} x[k]\,x[k+n] = 1, & n = 0 \end{cases}
$$

(3.1)

$$
C_{xy}[n] = \sum_{k=0}^{N-1} x[k]\,y[k+n] = 0, \quad 0 \leqslant n < N.
$$

Figure 3.1 shows an overview of the spreading sequences applicable to acoustic signals [Gar+15]. Two groups can be distinguished: the real and polyphase

sequences. The first group only uses two real phases (0 and π) for encoding the sequence. Binary Phase Shift Keying (BPSK) demodulates the signal after which it can be correlated. In the second group, the phase can take any value, embracing a good Doppler resilience but they require a more complex demodulation and often consist of only a single code [Mur+20].
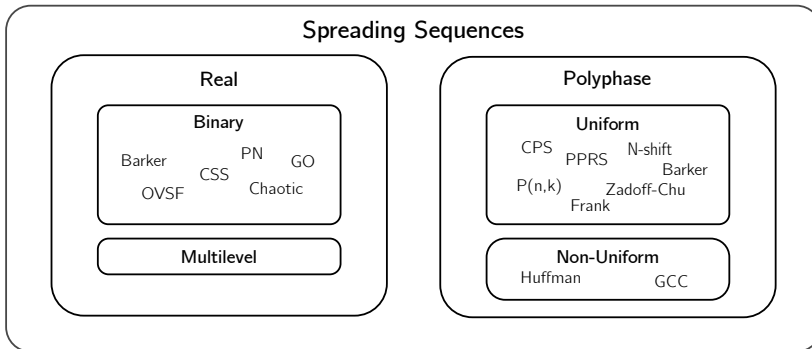
Figure 3.1: Overview of spreading sequences subdivided into two classes: real and polyphase sequences.

In ToA and TDoA based positioning systems, the acoustic signals are transmitted in an aperiodic manner. In other words, no continuous, periodic signal is sent by the transmitter but rather short encoded acoustic bursts are transmitted with silence in between. Although the burst itself can be broadcasted periodically, e.g. a 30 ms Barker code every other second, the noise received by the microphones during the silence periods makes the total signal aperiodic. In real scenarios, the periodic crosscorrelation functions from equation 3.1 can be expanded as follows:

$$
C_{xy}[n] = \begin{cases} \displaystyle\sum_{k=0}^{N-1} x[k]\,y[k+n] = 0 & 0 \leq n \leq N \\ \displaystyle\sum_{k=0}^{N-1} x[k]\,y[k+n] = 0 & \text{for other } n. \end{cases} \tag{3.2}
$$

Showing that the correlation between a coded signal and the received noise outside the code sequence should also be equal to zero. Asynchronous detection of the coded signal is possible but this implies that there is a constant correlation between the possible codes and received signal, leading to a large processing overhead, higher energy consumption and potential false detections. Additionally, an internal timer should time-stamp the received correlation peak. These timers can limit

the sampling time and correlation overhead, but they are prone to internal rates, drift, jitter and skews. Maximum likelihood estimators can partly overcome these errors [CSQ08] but a more robust and accurate approach is to synchronize the beacons and mobile nodes. Protocols, such as reference broadcast synchronization (RBS) protocol, the timing-sync protocol for sensor networks (TPSN) and flooding time synchronization protocol (FTSP), often used in Wireless Sensor Network (WSN), can be implemented for positioning applications [DP10].

In hybrid acoustic-RF systems, the high propagation speed of electromagnetic waves can be exploited for synchronization and communication. Thanks to the slower propagating acoustic waves, timing errors are not that critical as those in pure RF-based ranging systems. A 1 cm ranging error takes around 29 µs for acoustic LPS whereas it takes only 33 ps in RF-based systems.

To enable energy-neutrality, a spread spectrum technique is designed that can be processed on the limited processing capabilities and energy budget of the mobile node. When restrictions are applied, the advantages, the improved SNR, sensitivity and echo resolving, should still be present. The correlation between the original and received, noisy acoustic signal should still obtain a clear peak value and simultaneous transmission and identification of several mobile nodes or anchors should be possible. The measures to obtain these features often oppose the wanted energy conserving methods, e.g. long codes improve the SNR but require more processing power and longer receive windows or a higher bandwidth. In the next chapter, chirp pulses are conceived that trade off these properties in a feasible system architecture.

3.2   Real scenario constraints

Energy-neutral positioning with hybrid signaling in real-life environments comes with a couple of technical challenges. The hybrid aspect of this positioning technique is both a blessing and a curse as it combines the best of both worlds but at the same time there are two mediums where things can impact the signaling. The challenges addressed in the next subsection are acoustic based, since the essential ranging information is embedded in the sound signals. To make sure that the ranging systems does not intervene with our daily life, ultrasonic signals are chosen as they are inaudible to humans. Additionally, a larger bandwidth can be obtained in the ultrasonic domain, depending on the hardware.

3.2.1 Acoustic Scene and Channel effects

Undisturbed free-field propagation of acoustic signals is only possible in anechoic environments. In real life environments, there are a couple of channel effects that impact the sound intensity on the receiving end. For a continuously transmitting sound source, the measured sound pressure level at the receiver is the sum of the direct and reverberant sound. In general approaches, this depends on the sound pressure level of the transmitted sound signal, the directivity of the receiver, the distance to the source and room reverberation. The distance dependency of sound propagation in the free-field is given by the inverse-square law, decreasing the sound intensity by approximately 6 dB for each doubling distance. The room reverberation - or sound decay inside a room - describes *"a series of both physical and perceptual phenomena that occur in a enclosed environment, i.e. the room, and relates to the acoustical interaction between a sound source and the enclosure"* [Kap16] .This parameter is difficult to calculate for a real room with different objects, shapes and wall types.

This work lies outside the psychoacoustic domain, and does not have to deal with subjective parameters and human perception. There are two objective parameters of interest for hybrid positioning with microphones, the reverberation and the linked stationary Sound Pressure Level (SPL). Reflection, scattering and diffraction on objects and walls and attenuation influence this reverberation.

Intensity and Sound Pressure Level

In sound waves, the particles in a gas, fluid or solid media follow a space- and time dependent displacement, compressing and decompressing the medium. This implies an increase in mechanical energy, carrying the sound wave away from the source. The loudness of a sound is related to how energetically the source is vibrating and quantitatively described by the sound intensity, also called 'energy flux density'. In wave propagation, this intensity is the power per unit area carried by the wave, which has an SI unit of W/m². The relationship between the sound intensity (I) and pressure variation (Δp) of a plane wave is given by:

$$I = \frac{(\Delta p)^2}{2\,\rho\,v}, \tag{3.3}$$

where ρ is the density of the material in which the sound wave travels, v is the speed of sound in the medium and the pressure variation is the difference between the maximum and minimum pressure. Our hearing is most sensitive in the frequency range starting at 500 up to 5000 Hz. In this range, the intensity

thresholds between hearing a sound and experiencing pain differ about 13 orders of magnitude. For this reason, a logarithmic quantity is introduced: the sound pressure level, defined by the quotient of the time-averaged received pressure over a standardized reference pressure (p_0) of $2 \cdot 10^{-5}$ Pa whereby p_0 corresponds to the normal hearing threshold at 1000 Hz:

$$SPL = 20 \log \left(\frac{p_{rms}}{p_0} \right) = 10 \log \left(\frac{I}{I_0} \right). \tag{3.4}$$

The sound pressure level is expressed in decibel (dB), which is not a unit, but defines the logarithmic leveling scale.

In what follows, reflection, scattering, diffraction and attenuation are discussed as they all play a key role in reverberation, impacting the ranging performances.

Reflection

Plane waves that incident on a large rigid and smooth wall reflect according to Snell's law, potentially changing the amplitude and phase (Figure 3.2). In literature, this is known as specular reflection. An important determinant is the reflection factor $\underline{R}$. This parameter depends on the wall impedance $\underline{Z}$, the incident wave angle θ and the characteristic impedance of air Z_0.

$$\underline{R} = \frac{\underline{p}_r}{\underline{p}_i} = \frac{\underline{Z} \cos \theta - Z_0}{\underline{Z} \cos \theta + Z_0}. \tag{3.5}$$

A more well known and related constant often given by manufacturers and available in datasheets is the absorption coefficient α:

$$\alpha = \frac{|p_i|^2 - |p_r|^2}{|p_i|^2} = 1 - |\underline{R}|^2, \tag{3.6}$$

where p_i and p_r represent respectively the amplitude of the incident and reflected wave at the surface of the wall. For spherical waves, surfaces are hit at various angles and the total received signal can be approximated by taking the sum of a direct sound coming from source (S) and another point source, called the image source (S'). This latter is located at the mirrored point with respect to the surface and radiates a spherical wave with a reduced amplitude ($\underline{R}(\theta)$). This model is exact when the reflection factor $R = 1$ or $R = -1$. In any other case, the approximation is sufficiently accurate when the longitudinal distance (r) between the source and receiver is large ($r \gg \lambda$) [SN99].

In practical applications, surfaces are part of larger systems and internal, radiation and coupling losses can make the absorption coefficients frequency dependent.
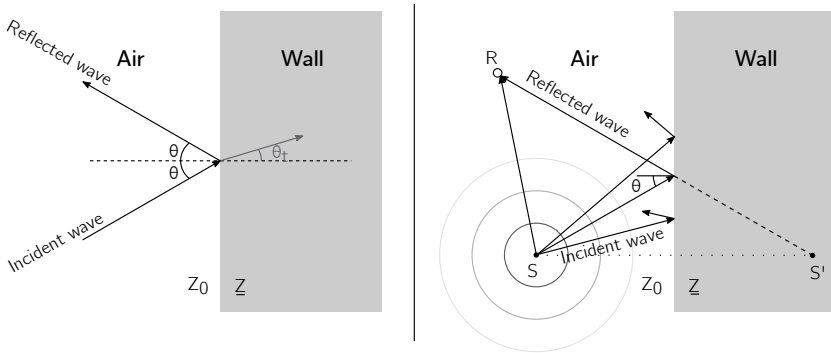
Figure 3.2: Reflection on a large smooth wall by a plane wave (left) and by a spherical wave (right) creating an image source.

Scattering and diffraction

Sound will be distorted following a specific distribution when sound hits an object. This scattering field depends on the size of the object (D) and the wavelength (λ) and is a difficult problem to solve except for typical cases such as spheres, cylinders, etc. In practical cases, the scattering field is mapped to an equivalent field created by a spherical scatterer. For surface scattering, sound reflection is also described by scattering and is frequency dependent as can be seen in Figure 3.3. When the wavelength is large in comparison to the scatter element length or depth, the object can be assumed as smooth. When these corrugations are in the magnitude of the wavelength, the scattered field becomes complicated. With higher frequencies, specular type of reflections occur. For rough surfaces, scattering may lead to sound paths with oblique angles of incidence, reflection and delayed arrival. Theoretical approaches often use spatial wave decomposition with the lowest order component as the specular reflection component and higher orders as scattered components [Vor07].

Reradiation at the edges and corners of objects is called diffraction. When the object is sufficiently smaller than the wavelength, the intensity is neglectable. For larger objects, sound intrudes the shadow zone behind the object and interferes with the original sound wave. Many objects encountered in real life environments approach the wavelength size and reradiation is therefore difficult to predict by calculation.
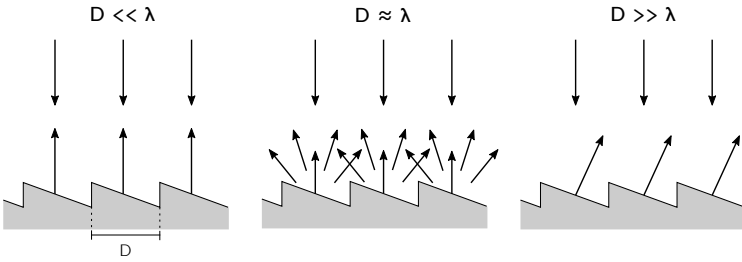
Figure 3.3: Scattering on surfaces at different frequencies.

Practically a scattering coefficient is often used (s_r) accounting for the scattering caused by surface roughness and diffraction (Figure 3.4). s_r values of 0 represent the specular reflection as showed in the left part of this figure, a value of 1 presents diffuse reflection [RC09]. This scattering coefficient is frequency dependent and increases with the frequency. This means that for ultrasonic frequencies, the reflection of sound signals becomes more diffuse due to the surface scattering. Typical values of these scattering coefficients can be found in the literature [Chr05].
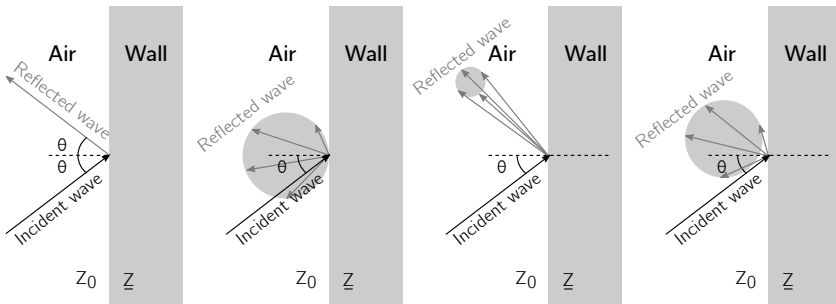
Figure 3.4: From left to right: ideal specular reflection by Snell's law with $s_r = 0$, diffuse reflections $s_r = 1$ and partially diffuse reflections $s_r = 0.1$ and $s_r = 0.9$

Attenuation

As aforementioned, the sound intensity of a spherical wave follows the inverse-square law, halving the received power with each doubling of the distance. In practice, there is an extra air absorption attenuation depending on viscosity, heat condition and thermal relaxation and energy extraction from the sound wave that is converted into other energy forms. Humidity has a large influence on the attenuation as translational, rotational or vibratory modes of water molecules can absorb this energy [Kut16]. Figure 3.5 shows the attenuation of the sound signal in dB/m for different frequencies and at different humidities. The attenuation becomes relevant for sound waves that are observed after a longer time period, with an attenuation reaching 1 dB/m for ultrasonic signals.
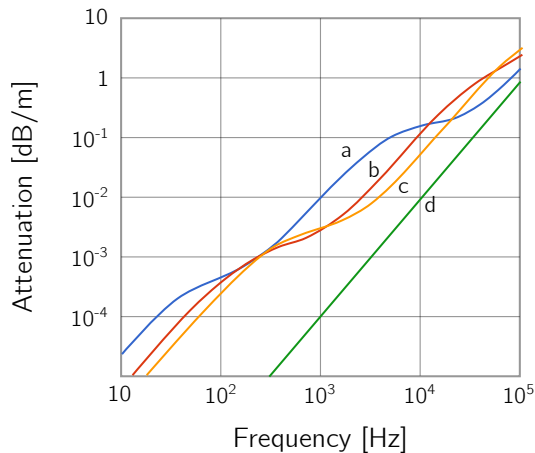
Figure 3.5: Frequency dependency of the attenuation at different humidity levels with a) 10%, b) 40%, c) 80% and d) classical theory. After [Kut06].

Reverberation

The aforementioned reflection, scattering and diffraction all influence the reverberation. A sound signal in a room will decay for a time period after transmission. In the literature, there are several methods that characterize this sound decay, depending on how acoustic signals are represented in the room. For wave equation based systems, reverberation can be seen as decaying vibrations.

In geometrical room acoustics, reverberation is defined as the sum of all, late reflections. For room acoustics, the reverberation time is often described by the Reverberation Time 60 dB (RT60) value, introduced by Sabine [ES01]. The latter is the time interval in which the reverberation drops down by 60 dB after a stationary sound source is switched off.

$$RT_{60} = \frac{24 \ln(10) \, V}{v_{20} \, S_a} \tag{3.7}$$

where V the volume of the environment, v_{20} the speed of sound at 20 degrees Celsius, and S_a the equivalent absorption surface in m².
Practical measurements for this decay process are done by sending out a sound impulse, e.g. popping balloon, and recording the SPL or by first estimating a Room Impulse Response (RIR) followed by sketching the energy decay curve. The reverberation time for small rooms lies around 0.3 s and this characteristic can go up to 10 s for large rooms such as churches. A closely related term often used in acoustics is the critical distance, being the distance at which the reverberated sound can drown out the direct sound SPL value. This depends on the sound source degree of directivity γ, the volume of the environment V and the RT60 value:

$$d_c = 0.057 \sqrt{\frac{\gamma \, V}{RT_{60}}}. \tag{3.8}$$

Doppler

In LPS, positioning objects are often not static. With mobile nodes, the Doppler effect can no longer be neglected. Its influence depends on the relative movement of sound receivers and sources. When one moves, a change in frequency, caused by the received rate of sound pressure minima and maxima, is observed. Depending on whether the transmit-receive pair move towards or away from each other, the perceived frequency goes up or down respectively. This influence on the acoustic positioning accuracy for moving targets can be large. For example, the acoustic positioning of an ant moving with a speed of 5 cm per second creates the same Doppler shift as the radar based positioning of NASA's X-43A, the fastest aircraft known to mankind, moving at Mach 10.
The Doppler effect has a negative impact on encoding and modulation schemes as observed in practical measurements performed by [Mur+20], as the main correlation peak amplitude decreases. Solutions can be found in chirp based encoding, as linear chirps show high Doppler tolerance for a wide range of time-bandwith products [Tho62].

3.2.2   Simulation Environment

The selection of a simulation environment to obtain a first indication of the impact coming from the aforementioned channel effects on the received acoustic signal is motivated here.

Geometrical acoustics algorithms can simulate sound fields fast for different room shapes and sizes. These simulations are sufficiently accurate for broadband signals and as long as the room dimensions are larger than the signal wavelength. Their advantage lies in their simulation speed, experimental replication, the ability to have a controlled environment, ease of room modification and thus scenario exploration, and large scale multiple in- and output simulations. In geometrical acoustics, a sound field is reduced to energy, transition time and direction of rays. The concept of sound wave is replaced by a sound ray. Two fundamental algorithms can be distinguished: ray tracing and image sources. The main difference is that in ray tracing, the energy is detected by volumes rather than points and that the physical energy propagation is stochastic by counting the received energy in the volume and not deterministic by distance. In this work, an open source, Image Source Model (ISM) based, shoe box RIR generator is used for simulating different scenarios [SBD17]. In this model, the lower reflected rays can be replaced by a virtual sound source perpendicular to the reflecting wall. The mirroring process can continue when the reflected sound signal hits a new wall, creating a second order image. This way, more and more image sources can be created with increasing orders. Eventually, these models create a RIR from the corresponding delays and attenuation. The aforementioned generator makes use of the Allen and Berkley algorithm [AB79]. For real to life room simulations, the ideal, rigid wall solutions from Allen and Berkley are often extended with wall reflection coefficients. Typical absorption (or reflection) coefficients for different materials can be found in tables. The Doppler effect is not taken into account for this shoe box simulation environment as it only supports static sound sources and receivers.

Care should be taken when simulating sound sources in these shoebox models as reception can suffer from *sweeping echoes*. This is a distinctive, continuous pitch increase caused by the progressive and monotonic convergence of high-order image sources in a rectangular simulation setting [De +15]. This phenomenon can be removed by introducing a small, random displacement away from perfect symmetric positions.
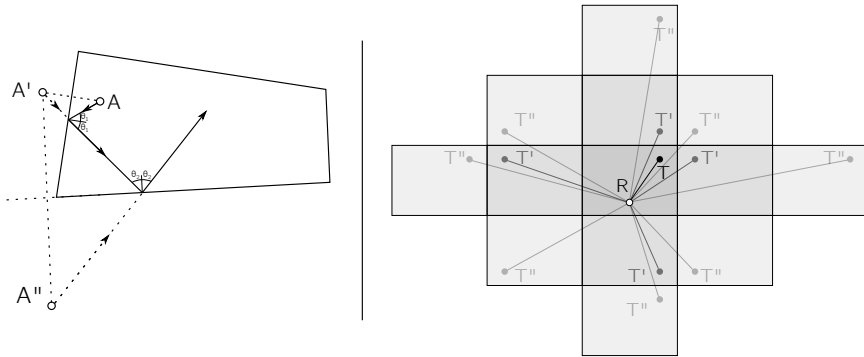
Figure 3.6: Left, first and second order virtual image for a single wall. Right, virtual image source model for a rectangular room extended with all second order reflections.

3.2.3   Restrictions in Ultrasonic Hardware

Ultrasonic transducers and microphones have, just like any other acoustic or RF system, a limited bandwith. Having insight in these bandwidths is crucial for broadband modulation sequence adaptations. As most MEMS microphones are designed for audible purposes, the frequency spectrum plots in their corresponding datasheets are limited to a maximum frequency of 20 kHz. For this reason, the frequency response of 7 low-power MEMS microphones, together with a baseband, 5 to 20 kHz flat response microphone was determined and is plotted in Figure 3.7. Measurements were performed in an acoustic anechoic chamber, with a log sweep going from 20 Hz to 80 kHz transmitted by a broadband ultrasonic tweeter (Fostex FT17H [4]). The MEMS microphones were positioned 1 m away from the sound source and a 1 kHz sound signal had a SPL of 41.1 dB. All microphones show similar behavior to the flat response microphone, increasing the SPL in the audible region and decreasing it in the ultrasonic domain. This shows that the speaker has a major influence on the received acoustic spectrum. The MEMS differ in these regions among each other. With the microphone's sensitivity as main selection criterion, the VM1000 [5] and MM20 [6] show the best results in the audible, and the IMP23ABSU [7] in the ultrasonic region. This latter is rated as an ultrasonic microphone, however, it does not significantly outperform the other microphones, making them capable of doing measurements in this region as well. Outside an anechoic chamber, these MEMS microphones only show an acceptable ultrasonic bandwith of 25 kHz, going from 20 kHz up to 45 kHz.
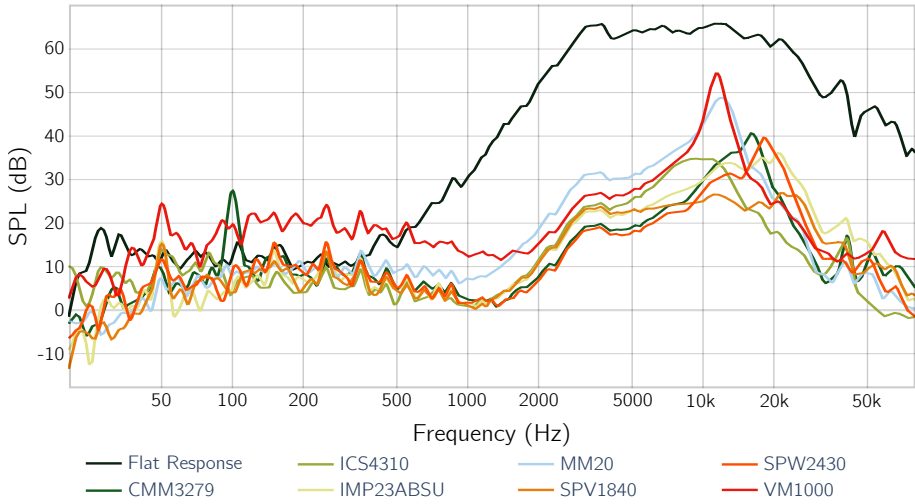
Figure 3.7: Microphone frequency response of 7 MEMS microphones for transmission of a log sweep going from 20 Hz to 80 kHz broadcasted by a Fostex FT17H speaker and performed in an anechoic chamber. 1/12 smoothing with no SPL compensation is applied to the measurement data.

Another hardware restriction that should be considered when designing an acoustic-based indoor positioning system is the directivity. In idealized cases, both speaker and microphone should transmit or receive an audio signal to or from all angles with the same amplitude. In real case scenarios, some angles are attenuated, while others are amplified. In acoustic positioning, omnidirectional receivers are required, as the sound signal can come from every angle. For speakers, omnidirectionality could lead to unwanted reflections. On the other hand, too directional transmitters could lead to shadow zones where no direct sound signal is obtained. The directivity of both speakers and microphones is frequency dependent. Generally, the directivity pattern of a speaker sharpens with the increasing frequency. A measured polar plot of the earlier described ultrasonic transducer (FT17H) and a cheaper alternative (Kemo L010 [8]) transmitting a 25 kHz sine wave are depicted in Figure 3.8. Measurements are performed in a large room with low-power acoustic signal transmission and a distance of 1 m between transmitter and receiver. In the XY plane, a half power beam width angle of 30° can be observed for a frequency of 25 kHz. To counter the shadowing when placing speakers in an indoor setup, multiple speakers are often combined in one constellation. For omnidirectional speakers, setups like dodecahedron or more generally omnidirectional parametric

loudspeakers are formed [Arn+18; Que+14]. However, these systems are often omnidirectional for a narrow band of audible or ultrasonic sound signals, and, again, with the increase of frequency, lobes arise in the spherical pattern leading to higher order rotational symmetries [KWV13].
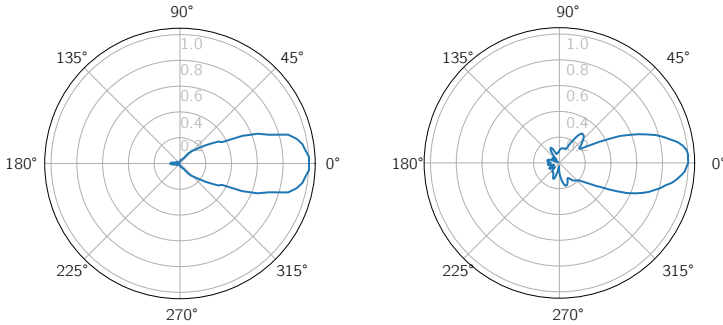
Figure 3.8: Measured polar plot of the relative, XY directionality of a Fostex FT17H speaker (left) and Kemo L010 [8] (right) for a 25 kHz signal.

A directivity assessment of different MEMS microphones was conducted for microphone array applications. The polar plots in Figure 3.9 of a single Sonion N8 [9] MEMS microphone depict the spectral response at different frequencies. The results were obtained by placing the MEMS microphone on a stepper motor construction and making a 360° turn around its z-axis in steps of 3°. Sine wave signals at different frequencies were transmitted by a single speaker 2 m away from the microphone construction. The received signals were averaged by calculating the root mean square value over a 3 s interval and adapted with the flat response factor measured with an Earthworks M30 [10] flat response microphone. At higher frequencies, not only are the signals more attenuated, but they become more directional as well. From this assessment, it could be concluded that the omnidirectionality statement from microphone datasheets only holds for the lower frequency range. One can assume that in the ultrasonic domain, the directionality of these MEMS microphones becomes more and more apparent and significant for indoor positioning.

Next to the acoustic transmitters and receivers, the surrounding hardware should be checked for functioning in the ultrasonic domain. In all acoustic measurements, the bandwidth of commercial available amplifiers was tested prior to connecting it to the ultrasonic speakers. At the receiver side, amplifiers with a high Gain-Bandwidth Product (GBWP) should be selected as the ultrasonic bandwidth can be higher and correct filtering should be applied on the incoming signals.
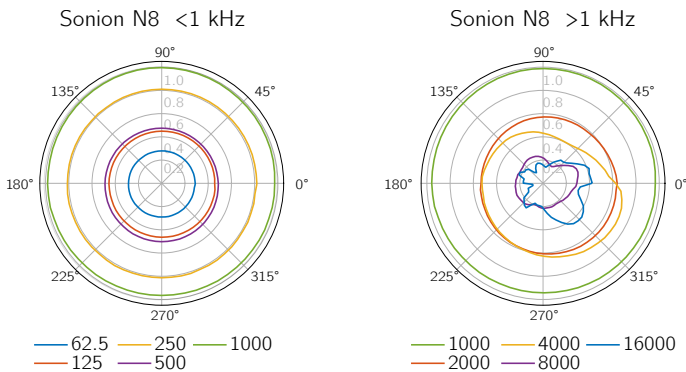
Figure 3.9: Splitted, normalized spectral response of Sonion N8 [9] MEMS microphone.

3.3 Implications for Energy-Neutral Devices

In order to achieve energy-neutrality at the mobile devices, three prerequisites are proposed for using acoustic signaling in a hybrid RF-acoustic positioning system:

1. Acoustics signals should be received instead of transmitted at the mobile nodes.

2. The active time of receiver devices should be kept as low as possible.

3. Mobile device should be allowed to be lazy.

These three rules can be applied to the envisaged hybrid indoor positioning system. When comparing a cutting-edge, commercially available MEMS speaker (USound UT-P2023 [11]) with a microphone (Vesper VM1000) a look at the power consumption shows that the speaker and reference driving circuit consumes around 46 mW for a 60 dB SPL at 10 cm distance. For microphones and accompanying audio amplifiers, the total power consumption is 0.775 mW at a driving voltage of 3.3 V. This first requirement comes with a couple of implications at the mobile node. Acoustic reception requires omnidirectionality of the microphone. MEMS microphones are often used in acoustic positioning, but as seen in Figure 3.9, the omnidirectionality decreases with the increasing frequency. As narrowband systems have a limited accuracy, this MEMS microphone should have a broadband acoustic frequency as well. A second implication is the need for synchronization

and communication for ToF-based positioning, as it should be known when the acoustic signal is received and information regarding the ranging estimation should be communicated back to the anchor nodes. In hybrid RF-acoustic systems, the RF signal can be used for this, coming with an additional hardware and energy consumption cost.

To limit the active time of the mobile nodes, the most obvious strategy is to turn the device off or put it in a low-power sleep mode as much and as fast as possible. Synchronization should assure timed wake-up for acoustic signal reception. However, there are specific, hardware dependent wake-up times leading to missed acoustic reception windows and increased power consumption. Table 3.1 resumes the power consumption and acoustical characteristics of the MEMS microphones used in the frequency response measurements of Figure 3.7. As deduced from this table, the wake-up times can come as short as 200 µs up to 0.8 s, confirming that these wake-up times can have a major impact on the power consumption. The reduced active time not only has impact on the power consumption of the hardware but also implies less received acoustic data, shorter processing times and also less data to communicate back to the anchors. This suggests it is necessary to search alternatives for the long spread spectrum codes discussed in section 3.1 but with similar encoding performances.

By shifting the processing tasks from the energy-neutral mobile node to the anchor nodes, processors and microcontrollers can often be eliminated on the first. In the approach adopted in this work, the acoustic signal could be directly modulated on an RF signal, and an RF-receiver should simply decode the received signals. The only concern the designer has then left is to implement an energy efficient RF communication technology.

3.4   Conclusion

In this chapter, the focus lied on the acoustic constraints of the hybrid-indoor ranging system. It is shown that broadband acoustics signals with proper encoding are preferred over narrowband signals as they are more resilient to noise and improve the sensitivity at the cost of additional hardware components. For the ToF method, aperiodic correlation can be initialized by the RF signal, acting as a synchronization signal.

The ultrasonic domain should be chosen for the acoustics ranging signals as they do not intervene with our daily activities. Real scenario constraints for these ultrasonic signals show that scattering and air absorption attenuation are more prominent due to these higher frequencies. Other channel effects, such as

Type	Supply Voltage[V]	Supply Current [µA]	Sensitivity [dB]	SNR [dBA]	Freq. Response	Startup Time [s]
Invensense ICS-40310	0.9 - 1.3	16	-37	64	90 - 16 kHz	0.8
Knowles MM20	0.9 - 1.3	38	-55	70.5	20 - 20 kHz	0.5
Knowles SPV1840	1.5 - 3.6	45	-38	62.5	>10 kHz	/
Knowles SPW2430	1.5 - 3.6	70	-42	59	>10 kHz	/
CUI CMM-3729	1.6 - 3.6	80	-38	85	>10 kHz	/
ST IMP23ABSU	1.5 - 3.6	120	-38	64	20 - 80 kHz	/
Vesper VM1000	1.6 - 3.6	165	-38	62	>10 kHz	200 µ

Table 3.1: Overview of power, frequency and timing specifications of MEMS microphones used in measurements.

reflection and the sound intensity behave similarly as their audible counterparts. As most commercial components are made for our human hearing, measurements were performed to assess how well the available hardware performs outside this domain. Speakers and microphones become more directional and available MEMS microphones only show an acceptable bandwith of 25 kHz when combined with an ultrasonic tweeter.

The cherished mobile nodes' energy-neutrality offers some prerequisites for using the ultrasonic signaling in hybrid RF-acoustic systems. At the mobile nodes, sound signals should be received, the wake-up and awake time limited, and processing should be shifted towards the anchor nodes. These three implications form the foundation for the following chapter in which the hybrid ranging method is introduced and tested within a real life environment.

Chapter 4

Hybrid RF-Acoustic Ranging

This chapter is adapted from:

- Cox, B., Van der Perre, L., Wielandt, S., Ottoy, G., De Strycker, L. "High Precision Hybrid RF and Ultrasonic Chirp-based Ranging for Low-Power IoT Nodes.", 2020, Eurasip Journal On Wireless Communications And Networking, Art.No. 187, 1-24. doi: 10.1186/s13638-020-01795-1 [Cox+20a]

- Cox, B., Van der Perre, L., De Strycker, L., "Zero-crossing Chirp Frequency Demodulation for Ultra Low-Energy Precise Hybrid RF-Acoustic Ranging of Mobile Nodes.", 2020, IEEE Sensors Letters, 1-4. doi: 10.1109/LSENS.2020.2990213 [CVD20]

Contributions: The author performed the theoretical study, simulations and conducted the measurement campaigns. The innovative idea behind the system design was coined by the author and co-authors of the first paper. Peak selection optimization was co-composed by the author and Stijn Wielandt. The zero-crossing method was an idea of the authors of the second paper. All co-authors contributed to the writing of the manuscripts.[1]

This chapter presents four main contributions towards the positioning of energy-neutral nodes. The first is a novel hybrid RF-acoustic signaling that performs a just-in-time wake-up of the nodes. This concept enables ultra low-power consumption at the mobile node and takes the implications from the previous chapter into account. Secondly, a fast and lightweight algorithmic solution to resolve incorrect measurements due to reflective acoustic signals is proposed.

---

[1]A special thank you to Koen Deforche and Ivo Vanderweerd from BlooLoc for coming to us with the initial low-power positioning problem statement.

Power consumption optimization in the form of data reduction by means of zero crossing chirp frequency demodulation is the third addition of this chapter. The last contribution is the realization of an experimental set-up that was used to validate the results in real-life proof of concept.

4.1   Hybrid System Design

Pioneering hybrid RF-acoustic system designs consisted out of two classes. The Active Bat Local Positioning System [Har+02] proposed the original concept of the indirect positioning class, where the position of a mobile node is calculated on a system level. Base stations are attached to the ceiling and periodically broadcast a radio message containing a single identifier, causing the corresponding mobile node to emit a short encoded ultrasound pulse. The position is calculated at a central point using the time of arrival (ToA) at the different anchors. The second class is developed by the Cricket System [Pri05] and introduces self positioning, where mobile nodes calculate their own position ensuring their privacy. Here, the base stations simultaneously emit ultrasonic and radio pulses for TDoA calculations. This straightforward approach of simultaneously transmitting the acoustic and RF signal introduced by the Cricket System has the potential to overcome the implications for implementation in energy-neutral mobile nodes introduced in Section 3.3. While it offers high precision, the TDoA method with narrowband ultrasonic signals can suffer from in band noise, low update rate and a limited multiple access mode. Additionally, receivers are powered on for a relatively long time, waiting for the acoustic signal to arrive. This latter prohibits an ultra-low power ranging system.

In this section an alternative solution is proposed where:

- The RF signal is transmitted at the end of the acoustic signal broadcast, to wake-up all receivers simultaneously for a short duration only.

- Signals are modulated in order to enable the extraction of delay information later on. Acoustic chirp signals are used as a modulation, as they enable short awake times.

4.1.1   Hybrid Ranging System Concept

Figure 4.1 depicts the proposed hybrid ranging system concept in its most generic form. It consists of a single anchor (A) and one or more mobile nodes (M_x). The anchor is able to wake-up all the mobile nodes simultaneously by a single RF signal ($m_{RF}(t)$). A distance measurement is performed as follows:

1. An audio signal ($m_a(t)$) with a certain duration (τ_{tx}) is broadcasted by the anchor at a starting time (T_0).

2. At a given time ($T_A > T_0$), a single RF signal is transmitted, waking all the mobile nodes simultaneous for a short awake time (τ_{rx}). The mobile nodes receive, depending on their distance, a specific part of the delayed, distorted and modulated audio broadcast.

3. The received audio snippet can be processed locally or at the anchor nodes, after communicating back the received data, through pulse compression resulting in a distance estimation.
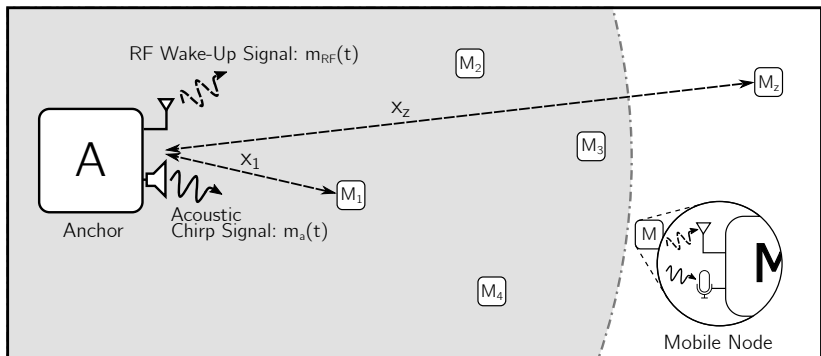
Figure 4.1: Ranging System Overview. The anchor periodically transmits a sound signal and the RF signal serves as a synchronized wake-up signal.

The timing diagram for an exemplary case with three mobile nodes is depicted in Figure 4.2, which illustrates the difference between the proposed concept and conventional hybrid RF/acoustic TDoA systems. The ranging information is comprised in the received chirp snippets: $\Delta f_{rx,n}$ for the nth mobile node. These snippets contain only a fraction of the original chirp signal and restrictions of the awake time will directly impact the accuracy of the measurements. On the other hand, a restricted awake time reduces the power consumption.
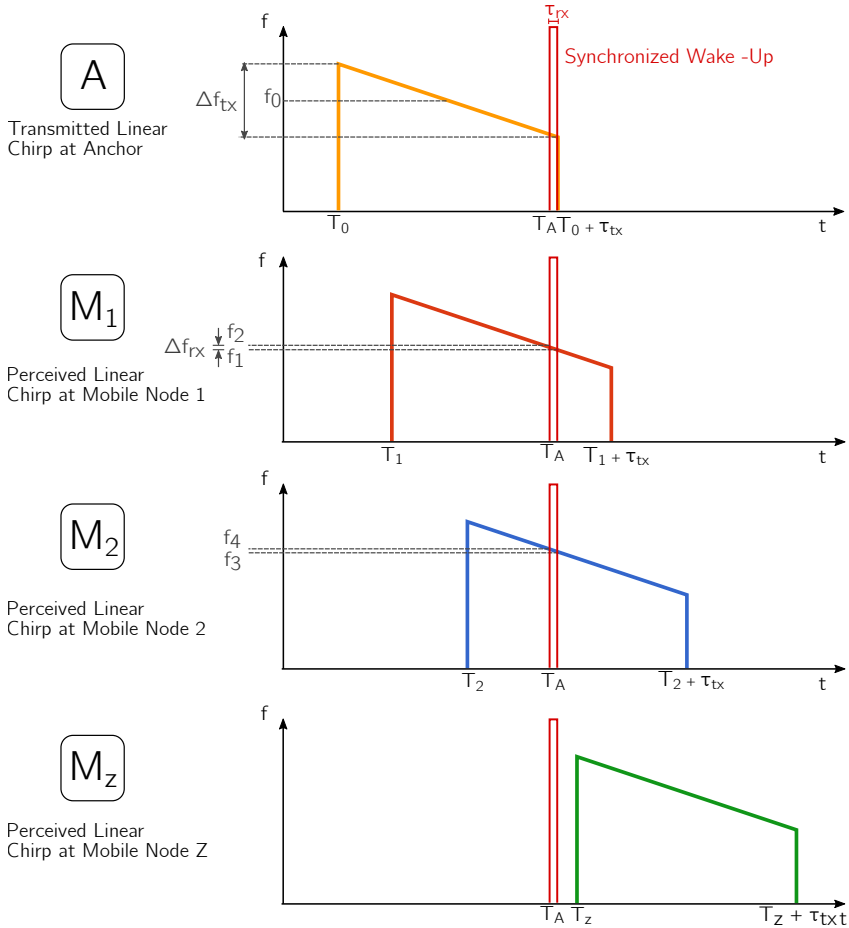
Figure 4.2: Timing overview of the transmitter and three mobile nodes as in the setup in Figure 4.1. Mobile node 1 and 2 are within the range of the anchor, mobile node z is not. The distances to the transmitter are calculated based on the received sound chirp extract.

Note that alternatively acoustic wake-up sensors [Gol+04] could be considered to avoid a long "on-time" of nodes waiting for the signal to arrive. However, these typically generate frequent false wake-ups caused by ambient sounds, decreasing the energy efficiency and system accuracy drastically. Another convenient strategy

could be to broadcast audio at fixed time intervals. In these scenarios, clock drift should be countered by performing timing synchronization between the transmitting and receiving side, leading to a more complicated and power hungry system architecture. Our proposed system can transmit the hybrid signals at its own convenience and is clock drift independent thanks to the RF-signals both acting as a time reference and communication backbone. Advantages of this system are the reduction of the awake times to milliseconds, the prevention of false wake-ups and the opportunity to use ultrasonic sound signals, enabling human unaware, acoustic positioning, and easy synchronization with RF.

4.1.2 Ranging Coverage

The ranging coverage of the system[2] is determined by the audio broadcast duration (τ_{tx}) and the speed of sound. For example, for a sound signal with a duration of 30 ms and a speed of sound of v_s = 340 m/s, the coverage is limited to 10.2 m. Figure 4.3 depicts the three possible ranging scenarios. The left scenario illustrates the standard operation described at the beginning of this section. For maximum coverage directly around the anchor, the RF wake-up signal is sent at the very end of the acoustic signal, i.e. $T_A = (T_0 + \tau_{tx}) - \tau_{rx}$. In Figures 4.1 and 4.2, mobile node z is too far away from the anchor to receive the sound signal when it wakes up, as $\frac{x_z}{v_s} > (T_A - T_0)$. It is therefore incapable of calculating its distance to the anchor.

If the RF wake-up signal is sent earlier during the audio broadcast, the maximum ranging coverage is reduced, as illustrated in the middle scenario.

If the RF-awake signal is sent after the audio broadcast, a disk shaped coverage area is formed around the anchor, as depicted on the right side of Figure 4.3. Here the receivers close to the anchor do not receive a direct audio signal during their awake period, making them incapable of calculating a correct distance. On the other hand, the maximum distance to the anchor is increased.

The proposed system permits both self (device based) and indirect (monitor based) positioning. The first is achieved by locally processing the audio samples, the latter by transmitting the audio samples back to the anchor by means of instantaneous RF communication. In view of the energy-neutral mobile node requirements, indirect positioning is further used in this research. As aforementioned, multiple

---

[2]This is an area around an anchor, in which mobile nodes can measure their distance to that anchor.

nodes can be positioned at the same time. This however requires identification of the mobile node, which can be done in the RF domain by concatenating an unique ID before or after the acoustic data.

Ideal close ranging:
$T_A = (T_0 + \tau_{tx}) - \tau_{rx}$

Limited close ranging:
$T_A < (T_0 + \tau_{tx}) - \tau_{rx}$

Extended ranging:
$T_A > (T_0 + \tau_{tx}) - \tau_{rx}$
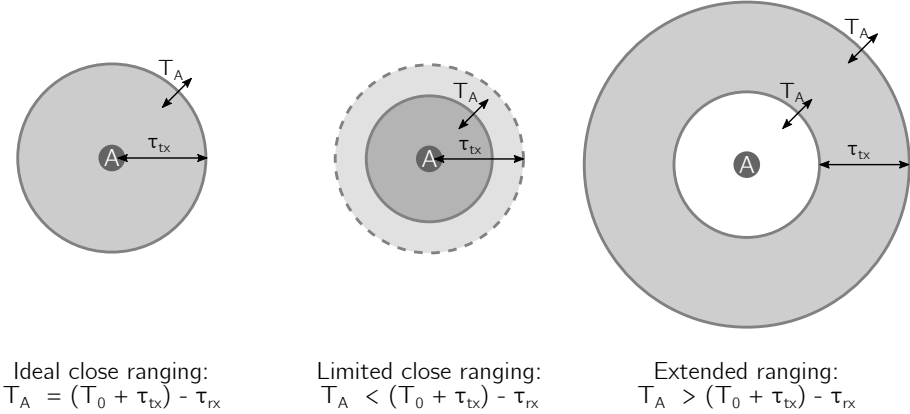
Figure 4.3: The ranging scenarios possible when shifting the RF wake-up signals in time.

By adding at least two more anchors to the system, two-dimensional positioning of the mobile nodes can be achieved. The acquired, relative distances to these anchors can be used in circular lateration or other geometric models to find the position of the mobile nodes [Mun+09]. Identification of the sound source is crucial here, and similar to the mobile nodes, multiple access techniques (e.g., FDMA, TDMA, CDMA) as proposed by [Che+19; TS19; YJC20] can achieve this.

4.2 Pulse compression

Cross-correlation is used to perform fast distance calculations using small data sets, as described in [PJF91; Mar+92], and exploited in [Nak+01; HDK16]. The aforementioned linear chirp [Mur+20; BB18; Khy+17] is used as audio broadcast signal for two reasons. First of all, mobile nodes can rely solely on the range dependent, measured chirp snippet Δf_{tx} to compute their distance to the anchor. Secondly, when processing, chirps have compressed inter-correlation signals [LR12].

A linear chirp, $s_c(t)$, can be described in its complex form as:

$$s_c(t) = \begin{cases} A\, e^{i2\pi\left(\left(f_0 - \frac{\Delta f}{2}\right)t + \frac{\Delta f}{2\tau}t^2\right)}, & \text{if } 0 \leqslant t < \tau \\ 0, & \text{otherwise}, \end{cases} \tag{4.1}$$

where τ is the pulse duration, A is the amplitude of a rectangle window function which should be chosen carefully to maintain the amplifier's operation in its linear region, f_0 is the carrier frequency and Δf is the nominal chirp bandwidth. The equation for the instantaneous frequency $f(t)$ shows this linear ramp of the chirp:

$$f(t) = \frac{1}{2\pi}\left[\frac{d\phi}{dt}\right]_t = f_0 - \frac{\Delta f_{tx}}{2} + \frac{\Delta f_{tx}}{\tau}t, \tag{4.2}$$

where $\phi(t)$ is the phase of the chirped signal.

As acoustic transmission through a speaker only plays the real part of the complex chirp, the corresponding time-domain function for this chirp is given by:

$$\text{Re}(s_{c,tx}(t)) = A\cos\left(2\pi\left(\left(f_0 - \frac{\Delta f_{tx}}{2}\right)t + \frac{\Delta f_{tx}}{2\tau_{tx}}t^2\right)\right) \tag{4.3}$$

With Δf_{tx} and τ_{tx} respectively the transmitted nominal bandwidth and pulse duration. Similarly, the time-shifted, received acoustic signal with shorter pulse duration τ_{rx}, bandwidth Δf_{rx} and receiver wake time T_A becomes:

$$\text{Re}(s_{c,rx}(t)) = A\cos\left(2\pi\left(\left(f_0 - \frac{\Delta f_{rx}}{2}\right)(t - T_A) + \frac{\Delta f_{rx}}{2\tau_{rx}}(t - T_A)^2\right)\right) \tag{4.4}$$

Cross-correlation and autocorrelation of linear chirps can be calculated via the complex chirp forms. This results in a form of pulse compression and can be achieved in the proposed system by convolution of the received signal with the conjugated and time-reversed transmitted signal:

$$\langle s_{c,tx}, s_{c,rx}\rangle(t) = \int_{-\infty}^{+\infty} s_c^\star(\tau_{rx})\, s_c(t + \tau_{rx})d\tau_{rx}. \tag{4.5}$$

It can be shown [Hei04] that the autocorrelation of a chirp signal is given by:

$$\langle s_{c,tx}, s_{c,rx}\rangle(t) = A^2\tau_{rx}\Lambda\left(\frac{t}{\tau_{rx}}\right)sinc\left[\Delta f_{tx}t\Lambda\left(\frac{t}{\tau_{rx}}\right)\right]e^{2i\pi f_0 t}, \tag{4.6}$$

with Λ a triangle function, with a value of 0 on $[-\infty, -\frac{1}{2}]\cup[\frac{1}{2}, \infty]$ and linearly increasing on $[\frac{-1}{2}, 0]$ where it reaches its maximum 1, and then decreasing linearly

on $[0, \frac{1}{2}]$. Around the maximum, this function behaves like a cardinal sine, with a -3 dB width of $\tau' \approx \frac{1}{\Delta f_{rx}}$. For common values of Δf_{rx}, τ' is smaller than τ_{rx}, hence the name pulse compression.

The pulse compression ratio for a linear chirp can be described as the ratio between the received pulse and the compressed pulse duration:

$$\frac{\tau_{rx}}{\tau'} = \tau_{rx} \, \Delta f_{rx} = \tau_{rx}^2 \frac{\Delta f_{rx}}{\tau_{rx}} = \tau_{rx}^2 \frac{\Delta f_{tx}}{\tau_{tx}} \ . \tag{4.7}$$

This equation can be rewritten as the time bandwidth product, which is generally larger than 1. As the energy of the signal is kept constant when pulse compression is performed, the energy gets concentrated in the main lobe of the cardinal sine, resulting in an SNR-gain proportional to the compression ratio.

In this work, chirp pulses are conceived to meet all the target system requirements. Three parameters in Equation (4.7) can increase the SNR-gain and inherently result in more accurate distance calculations:

1. The nominal chirp bandwidth (Δf_{tx}), limited by the combined speaker and microphone frequency response as presented in Section 3.2.3. These empirical measurements show that, at larger distances, the upper limit frequency is defined at 45 kHz, so the Δf_{tx} is in practice 25 kHz with COTS

2. The audio broadcast duration (τ_{tx}), which should be as low as possible for an optimal compression ratio. However, limiting this parameter decreases the coverage range, as explained in Figure 4.3. In this work, the target range is 10 m, resulting in a broadcast duration of $\tau_{tx} = 30 \, ms$.

3. The receiver awake time (τ_{rx}). This parameter should be set with care. On the one hand, there is a direct relationship with the time-bandwidth. Increasing τ_{rx} improves the SNR and accuracy quadratically. On the other hand, the receiver awake time should be kept as low as possible to restrain the power consumption for a single measurement.

As a visual example, the pulse compression of a chirp with a nominal chirp bandwidth of $\Delta f_{tx} = 20$ kHz and a constant pulse duration $\tau_{tx} = 30$ ms for different awake times is depicted Figure 4.4. This figure confirms that the longer the chirp excerpt, the higher and narrower the correlation. Correct maxima at a sufficient resolution can be derived from the pulse compression calculations when the awake time is limited to 1 ms. For these simulations, the frequency domain cross-correlation based on fast Fourier transformation is used with a complexity of
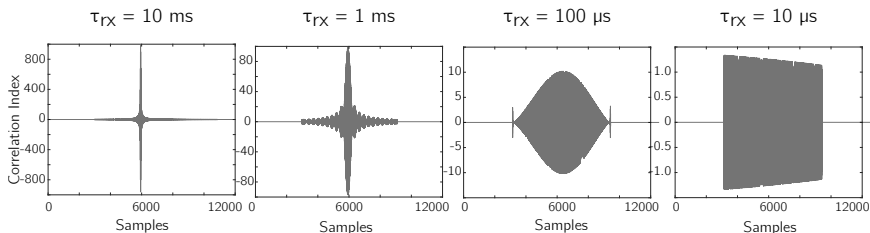
$$O[n_{tx} \cdot log(n_{tx})] \tag{4.8}$$

Figure 4.4: Influence of the awake time (τ_{rx}) on the pulse compression.

This complexity only depends on the transmitted signal length and sample frequency since the chirp extract is zero padded to obtain two vectors of equal length, necessary in the used cross-correlation algorithm.

Compared to other spread spectrum techniques described in Section 3.1, the main advantages of the broadband chirp method lies in the ease of implementation at both the anchor and mobile node side. For low-cost and low-power systems, the synchronization and processing are kept simple, the awake time is kept low and it still yields a clear correlation peak. The main disadvantage is the lack of simultaneous transmission without compromising on the acoustic bandwith and thus decreasing the ranging accuracy. It can be concluded that the chirp-based method has a lot of similarities with the spread spectrum that are too power hungry to be implemented on energy neutral mobile nodes.

4.3   Simulation-based Performance Analysis

To assess the performance of the proposed ranging system under realistic noise conditions and in reflective indoor environments, simulations were conducted in a shoebox, ISM-based environment as described in Section 3.2.2. All RIR-calculations were performed in a $6 \times 4 \times 2.5$ m room with rigid walls. The sound source is positioned slightly off the room center at a height of 1 m to prevent sweeping echoes. Both the sound source and the receiver positioned in this room are perfectly omnidirectional. The absorption coefficients of the walls are kept uniform over all 6 planes. This is accurate as long as the wavelength of the sound is small relative to the size of the reflectors [SBD17]. The speed of sound is kept constant (340 m/s) considering a uniform room temperature of less then $20°$ C and the sample frequency is set to 196 kHz, which is larger than the Nyquist frequency of the ultrasonic speaker's transmit frequency (40 kHz). The audio broadcast duration τ_{tx} is fixed to 30 ms such that every possible sensor position

in the simulation environment receives a sound signal during its wake-up period.

Two types of simulations are performed. The first type is a Monte Carlo simulation to test the influence of signal bandwidth and additive white Gaussian noise on the accuracy of the pulse compression technique. During these simulations, the impact of the room characteristics, such as reflection, scattering and reverberation, are kept as low as possible. The second type of shoe box simulations evaluates the impact of the room's characteristics by creating simulation environments with 600 uniformly distributed microphones.
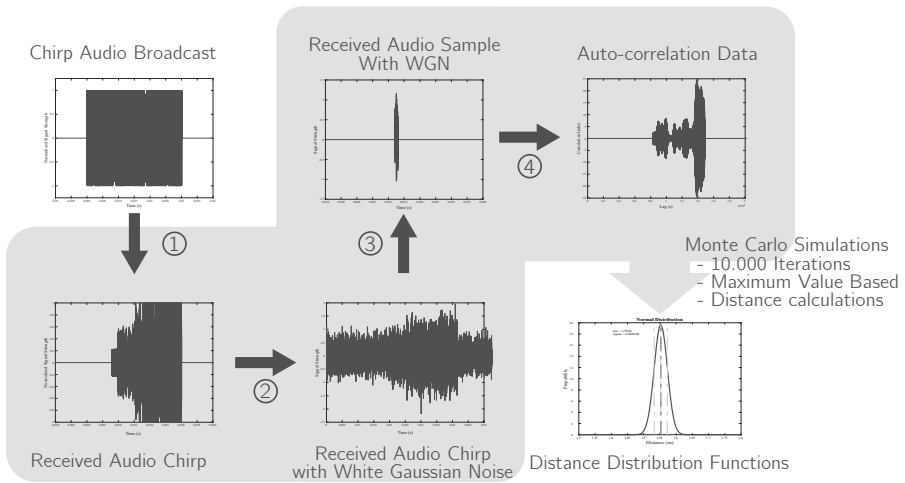
① Shoe Box Model: Received Audio Simulations ③ Windowing: Simulating the Wake-up Time
② WGN Addition at Predetermined SNR   ④ Autocorrelating

Figure 4.5: Overview of the Monte Carlo simulations to estimate the influence of the noise addition and chirp bandwidth.

4.3.1 Monte Carlo Simulations validating Pulse Compression

Monte Carlo simulations are performed to test the autocorrelation efficiency when noise is added to the received acoustic signal at different chirp bandwidths (Δf_{tx}). In a low-reverberant room, a single sensor receiver is positioned at a distance of 1.553 m from the source. The Monte Carlo simulation process is depicted in Figure 4.5. The first two steps are conventional to the source image method: the

room impulse response at the microphone is calculated and convoluted with the transmitted audio signal. In step 3 white noise is added to create sound signals with different SNR levels at the receiver. The next step consists of applying a 1 ms window to the noisy signal, mimicking the wake-up time of the mobile nodes. In the final step of the simulation, the emitted sound signal is correlated with the calculated, received sound signal, selecting the index of the correlation maximum and calculating the corresponding distance. The white noise addition, windowing and correlation processes are repeated 10 000 times. Post-processing fits the acquired distances to a normal distribution.

Table 4.1 shows the mean range error (ε) and standard deviation (σ) derived from the Gaussian distributions for five different chirp bandwidths at decreasing signal to noise ratios. The bandwidth dependency performs as expected for lower SNRs, with an increase in bandwidth improving both accuracy and precision. The influence of additive white noise on the accuracy is minimal with a ε below 1 cm for bandwidths above 20 kHz and true to life SNR levels of 3 dB and above. The precision however drops significantly, with an increased standard deviation of 50 cm and more. Worth mentioning is that in noisy environments, a better precision is achieved by using these lower chirp bandwidth signals. It can be concluded that with a limited chirp bandwidth of 20 kHz (45 kHz downto 25 kHz) implied by the MEMS' frequency response measurements, the accuracy and precision remain adequate to perform distance calculations in both noisy as well as in noiseless situations.

SNR (dB)		20	10	6	3	1	0
35 kHz - 25 kHz	ε	0.044	0.061	0.063	0.061	0.049	0.007
10 kHz BW	σ	0.024	0.043	0.058	0.092	0.277	0.573
45 kHz - 25 kHz	ε	0.001	0.011	0.008	0.008	0.029	0.068
20 kHz BW	σ	0.004	0.021	0.31	0.042	0.300	0.565
55 kHz - 25 kHz	ε	0	0	0	0.001	0.020	0.080
30 kHz BW	σ	0.001	0.014	0.020	0.042	0.316	0.652
65 kHz - 25 kHz	ε	0.001	0.002	0.004	0.005	0.029	0.109
40 kHz BW	σ	0.001	0.006	0.014	0.023	0.435	0.833
75 kHz - 25 kHz	ε	0.001	0.001	0.001	0.001	0.053	0.138
50 kHz BW	σ	0.001	0.004	0.008	0.099	0.550	0.887

Table 4.1: Standard deviation and difference between actual distance and mean value (ε) from Monte Carlo simulations with a single microphone at a distance of 1.553 m. All given distances are in meter.

4.3.2   Room Characteristics Simulations

The Monte Carlo simulations from the previous section show the influence of white noise addition and bandwidth on the proposed system's ranging error in an ideal, anechoic room. The following simulations test the pulse compression method when reverberation is present. Three shoeboxes are created, all with a different absorption coefficient: $\alpha = 0.05$, $\alpha = 0.3$, and $\alpha = 0.9$. These absorption coefficients are distinctively chosen and represent respectively an empty room with walls of standard brickwork, fiberboard and acoustic plaster panels [12]. In these rooms, 600 microphones (20x30) are uniformly dispersed in one quadrant of the room, with a fixed distance of 10 cm between two sensors or a sensor and a wall. The microphones and the sound source are positioned in the same z-plane, at a height of 1 m. Table 4.2 shows the P50, P95 and mean distance errors of the pulse compression technique with a chirp bandwidth of 20 kHz in these three rooms when no noise is added. The P50 value shows that half of the simulated distances have an error smaller than 3 cm in the most real world representative room ($\alpha_2 = 0.3$). The large difference between the mean and P50 value indicates that there are a lot of outliers, and is confirmed by the higher P95 values.

Absorption coefficient	0.05	0.3	0.9
Mean (m)	1.5330	0.5462	0.0108
P50 (m)	0.4158	0.0293	0.0007
P95 (m)	5.1463	3.1489	0.0502

Table 4.2: P50, P95 and mean values of the simulated distance estimates in the three rooms with no noise added.

To visualize the cause of these larger errors, a heatmap of the absolute mean ranging error for the two lowest absorption coefficients is shown in Figure 4.6. As expected, there is a considerable, negative effect of the reflections on the accuracy of the proposed system. The radius in which the ranging performs well decreases as the walls become more reflective. Inspection of the generated correlation data of an erroneous distance simulation, i.e. microphone 522 at a distance of 2.136 m in a room where $\alpha = 0.05$ (Figure 4.7), provides additional insights. The calculated distance corresponding with maximum correlation value is larger than the actual distance, indicated by the red line. Constructive interference of higher frequencies due to reverberation causes correlation peaks larger than the peak generated by the lower, effective distance frequency chirp snippet.
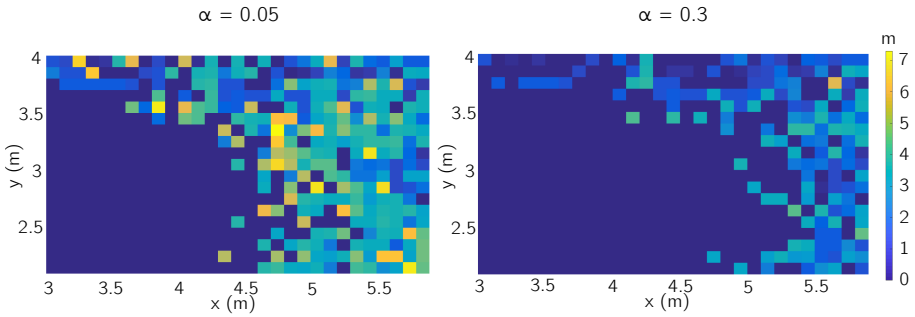
Figure 4.6: Heatmap of the simulated distance error for different absorption coefficients ($\alpha = 0.05$ and $\alpha = 0.3$).
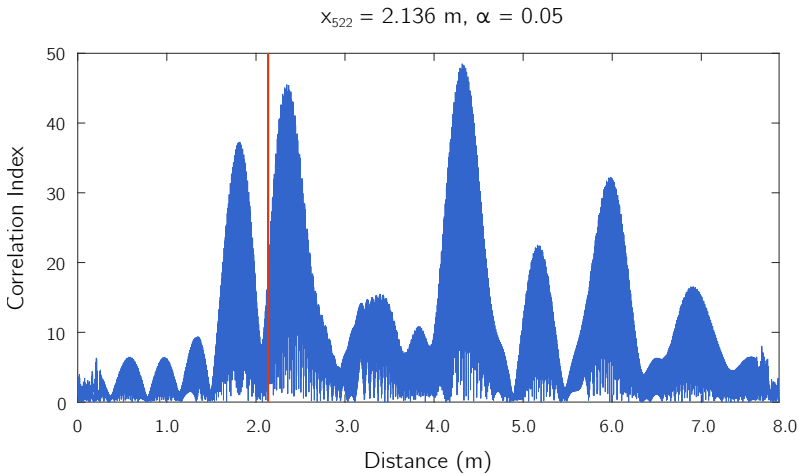
Figure 4.7: Cross correlation of the original transmitted chirp and a 1 ms sample for a microphone at 2.136 m distance from the sound source. The correct distance is indicated by the red line.

4.4 Enhanced Accuracy Solutions

Utilizing the maximum correlation index as a selection criterion for the distance measurements in highly reverberant rooms results in an adequate solution, yet it does not yield the best distance estimate in many situations. In most cases, the

correct maximum is the first one of a series of local maxima. This is explained by the fact that the lower frequencies have not arrived yet at the mobile node for a descending chirp signal. Three methods to select this first local peak and enhance the system's accuracy are proposed: window functions, peak prominence and delta peak approaches.

Method 1: Window functions

In the first method, window functions are applied to the correlation results, such that the first peaks of the local maxima are increased relatively to the others. The most straightforward window function is a linearly decreasing function, which is compared with the faster declining positive quadratic and exponential window functions. The optimal half-life time of the exponential window is empirically set to a tenth of the original broadcasted signal. These three functions give, in order of appearance, a larger weight to the early peaks. Advantages of this method are that it is effortless and weights can be applied directly on the calculated pulse compression data.

Method 2: Peak Prominence

The prominence of a peak indicates how much the peak stands out because of its intrinsic height and its location relative to other peaks [CM08]. It can be calculated as follows: a horizontal line from a chosen peak is extended to the left and the right until the line crosses a signal because either there is a higher peak, or it reaches the left or right end of the signal. Next, the minima of the left and right interval (min_1 and min_2 in Figure 4.8) are detected. These points can be valleys or the signal endpoints. Finally, the prominence is calculated by taking the difference between the height of the peak and the higher minimum of the two intervals. This means that a low, isolated peak can be more prominent than a higher member of a tall range. The index used for distance calculations is selected by calculating the prominence of all correlation peaks, setting a prominence threshold, the Peak Prominence Factor (PPF), and using the index of the first peak in the array of the prominences larger than the threshold.

Method 3: Delta Peak

In this approach, the difference between two consecutive local maxima is calculated and the peak following the largest positive difference is selected for further distance
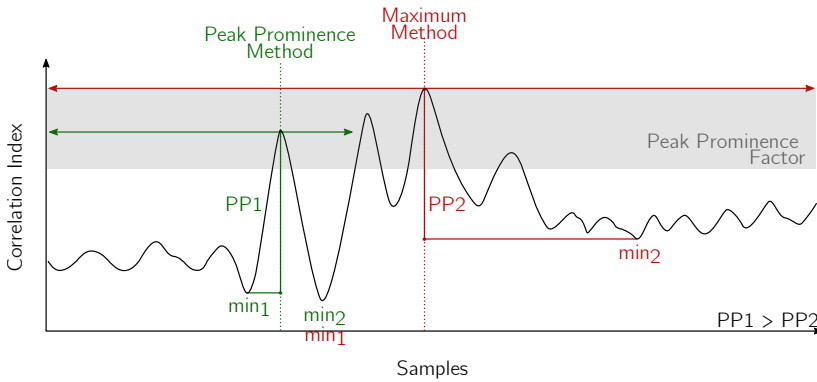
Figure 4.8: Comparison between the peak prominence and maximum method for early peak selection detection.

estimations. Just like the peak prominence method, searching for the largest delta peak does not alter the correlated data resulting in a lower computational cost.

Method Comparison

A comparative Cumulative Distribution Function (CDF) plot of the distance errors made by the proposed optimization methods in the simulated room with a uniform absorption coefficient of 0.3 is shown in Figure 4.9. The median (P50) distances of these methods range between 2.2 cm for the peak prominence method up to 5.2 cm for the exponential window function. Cm-accuracy can thus be obtained in ideal scenarios, where distances are short and there is minimal influence of room reverberation. When analyzing the CDF plots in more detail, it is clear that the maximum method has the worst performance, with a step wise increase in error and with large outliers and a high P95 value (3.15 m). A similar graph can be seen for the delta peak method, demonstrating that the complexity reduction compared to peak prominence impairs the accuracy. When examining the three window functions, it can be noted that adding a simple weight to all correlation values, and consequently increasing the influence of the earlier peaks, does improve the accuracy greatly. The exponential window function achieves the best P95 value (21.1 cm) and forms with the peak prominence the go-to methods for enhanced accuracy solutions. Additional simulations test the proposed methods when different levels noise are added to the received sound snippet. The mean

and median distance errors at these distinct SNR show that the peak prominence approach has the highest accuracy and precision, even at a very low SNR. This method should thus be implemented if sufficient processing power is available.
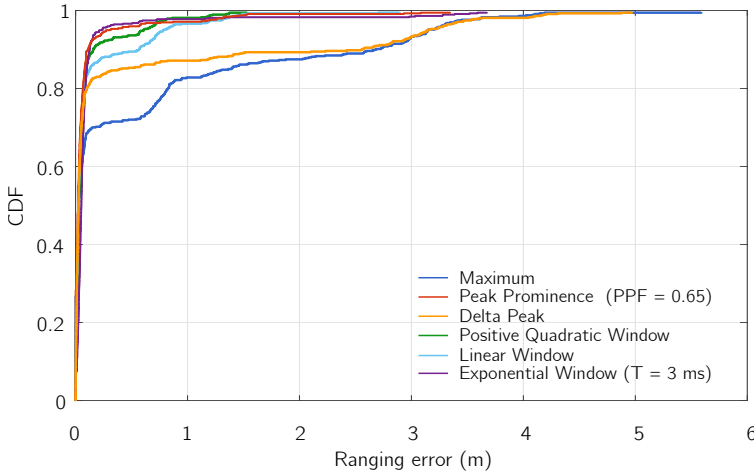
Figure 4.9: Cumulative Density Functions of the distance error of the proposed optimization methods in a room with $\alpha = 0.3$.

4.5 Initial Experimental Validation

4.5.1 Experimental Setup

The proposed hybrid signaling approach, the pulse compression technique and methods to improve the accuracy are tested in a real-life environment with focus on the key acoustic components. The acoustic transmitter and receiver are realized in hardware and the RF-based wake-up is implemented through a cable link between the two entities for proof of concept validation. Figure 4.10 depicts the system in an empty $6 \times 4.27 \times 3.41$ m³ room in which the walls consist of plaster-wood and glass, the floor of ceramic tiles and the ceiling of rock wool on solid backing. Three RT60 measurements were performed to test the reverberation time of this room. The average value and uncertainty at the different frequencies can be found in Table 4.3. The used measurement equipment only allows for RT60

measurements in the audible domain. The RT60 values in the ultrasonic domain will be lower, as the reverberation time is inversely proportional to the frequency.

Frequency (Hz)	250	500	1000	2000	4000	8000
RT60 (s)	1.17	0.94	0.78	0.78	0.79	0.59
Uncertainty (%)	7.8	6.2	4.8	3.4	2.4	1.9

Table 4.3: Average RT60 values of the room where the measurements were performed.

Figure 4.10: Measurement environment based in meeting room with speaker positioned centrally.

To receive the ultrasonic sound signals at low power, dedicated hardware has been designed with ultrasonic SPU1410LR5H MEMS microphones [13] as sound transducers and two opamps (TLV341 [14]) with a large gain bandwidth product to boost the low amplitude signals coming from the microphone. Active filters are added to the cascading opamps to narrow the amplified signals to the limited bandwidth in the ultrasonic domain (25 kHz to 45 kHz). A fixed LDO voltage regulator is added as a supply for the MEMS microphone and as an input offset voltage to guarantee a rail-to-rail output. The output of this ultrasonic receiver is then sampled with a NI-USB-6212 Data Acquisition System (DAQ) at 196 kS/s with 12-bit per sample resolution [15], and used as an input signal for the pulse compression performed in a Matlab environment.
The transmit side consists of the following elements: a Digital-to-Analog Converter (DAC), a commercially available amplifier circuit, and an ultrasonic speaker. Here, the NI-USB-6212 DAQ is used as a DAC to generate two signals: the 45 kHz to 25 kHz chirp and the 'start-sampling'-signal. The latter signal is sent over the

cable to the receiver side and is implemented as a pulse at T_A imitating the RF wake-up. This pulse initiates a 1 ms sampling time at the receiver DAQ. The DAC chirp signal is amplified with a commercially available amplifier circuit, based on a TDA7492 class-D opamp [16]. In-house tests have show that it has an amplification bandwidth over the intended 45 kHz. As an ultrasonic sound speaker, the aforementioned Fostex FT17H is chosen.

4.5.2 Ranging Measurements

The accuracy of the proposed solution is evaluated by performing acoustic measurements in one quadrant of the room, in which 63 measurement points with a mutual distance of 30 cm were dispersed. Two types of scenarios were tested: with the speaker directed to the x-axis and with a quasi-omnidirectional speaker. As in the simulations from Section 4.3, the sound source is located at an off-centered position.

The first measurement scenario shows that the signal power received outside the directional speaker's beam is limited, resulting in large accuracy errors, as can be seen in Figure 4.11. To obtain a quasi-omnidirectional speaker for the second measurement scenario, a semi-sphere is put on a distance from an upwards oriented tweeter, reflecting the sound in all possible directions. Tests in the audible domain and on a single XY-plane show only a difference of 6 dB between the maximum and minimum measured sound intensity level caused by the structure of the speaker. The results of the maximum method applied on these quasi-omnidirectional speaker measurements are in line with the corresponding simulations (Figure 4.11). The accuracy of these measurements is high for microphones close to the sound source. If the distance is increased or the microphone is closer to a wall, the accuracy drops.

Next to the maximum peak selection method, the enhanced accuracy solutions from Section 4.4 are applied to the quasi omnidirectional measurement data. A detail of the CDF plot can be found in Figure 4.12. With a median (P50) value of 9.04 cm, one can say that this method can enable below 10 cm accuracy. All methods follow the same curve for the first 80% of the measurements. For higher values, the peak prominence method performs best, with all errors below 1.85 m. The maximum peak selection method has the same P100 value but with higher P95 value and a more steadily increase above the 80% mark, this can be chosen as second best method. The delta peak in the measurements method shows a similar behavior as in the simulations where the large distance error outliers lead to a method that performs worse than the original maximum method. Comparable
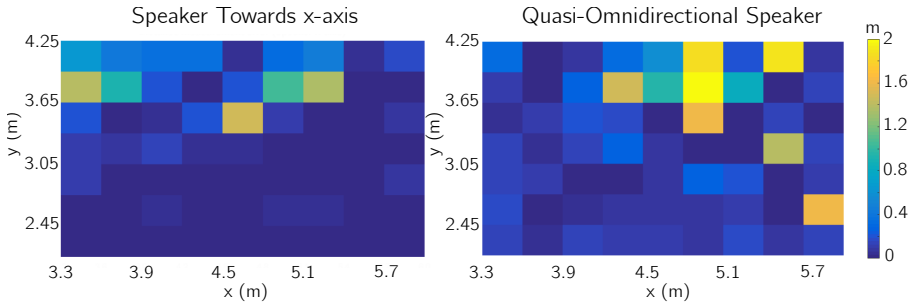
Figure 4.11: Heatmap of the maximum method in different measurement scenarios: when the speaker is aimed towards the x-axis and towards the z-axis with a semi-sphere (quasi-omnidirectional speaker).

results are found for the positive quadratic window method. These errors can be explained by the overamplification of the early correlation peaks, making them larger than the actual distance peak, and increasing the distance error.
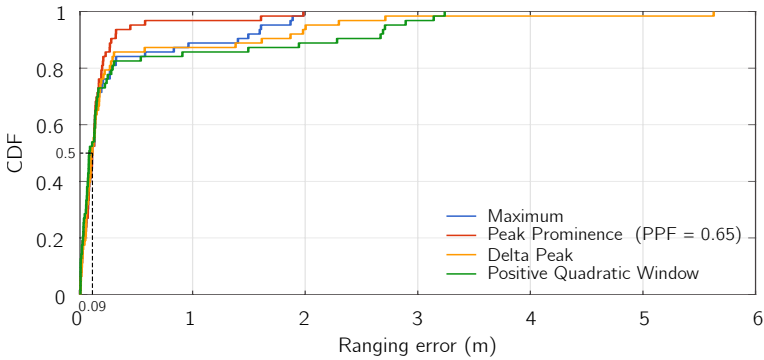
Figure 4.12: CDF plot of the maximum and improved accuracy methods on the quasi-omnidirectional dataset.

4.6 Zero Crossing Chirp Frequency Demodulation

The approach described in the previous sections involved limited processing at the mobile node, yet relies on an energy expensive ADC, that prohibits its application in real-time energy constraint devices. To further reduce the total energy consumption on a mobile node, energy efficiency at each level of WSN operation, sensing, computing, switching and transmission, should be pursued [RD14]. Their energy conservation schemes can be divided into three sub-categories: data driven, duty cycling and mobility based schemes [Ana+08]. In Wireless Acoustic Sensor Network (WASN), most research focuses on the data driven schemes as sensing and processing consume significantly less energy compared to communication operations [Bar19; Ali+09].
This PhD proposes a combination of the first two schemes:

- Data driven: the sought-after features of the audio on bit quantized level is researched, which will allow to eliminate power hungry analog to digital converters (ADCs) [MB18] and achieving both data reduction and computing power.

- Duty cycling: its contribution to the energy efficiency is twofold. On the one hand it switches off the nodes to a lower power stage. On the other hand, it only obtains data during this active time, decreasing the transmitted data proportionally to the duty cycle.

4.6.1 System Optimization

The maximum amount of acoustic data captured in the restricted wake-up time (τ_{rx}) is determined by the combination of the system's ADC sampling rate and the wireless data throughput. This is typical for WASN relying on conventional ADC's in combination with low-power, long-range sub-GHz communications. The sub-GHz development board (CC1310 [17]) used in the experimental validation of this work has an ADC with a resolution of 12 bits and a maximum sampling rate of 200 kS/s. For an awake time (τ_{rx}) restricted to 1 ms, 2400 bits are hence generated by the ADC. However, the maximum data throughput on the wireless link is 500 kbps, and as a result only 500 bits can be transmitted from the mobile node to the anchor in this single millisecond. This means that for optimal sampling during the awake time, assuming 12 bit/sample, the ADC sampling speed should be decreased to 41,7 kS/s. Pulse compression with this lower amount of ADC samples spreads the cardinal sine and reduces the accuracy drastically.
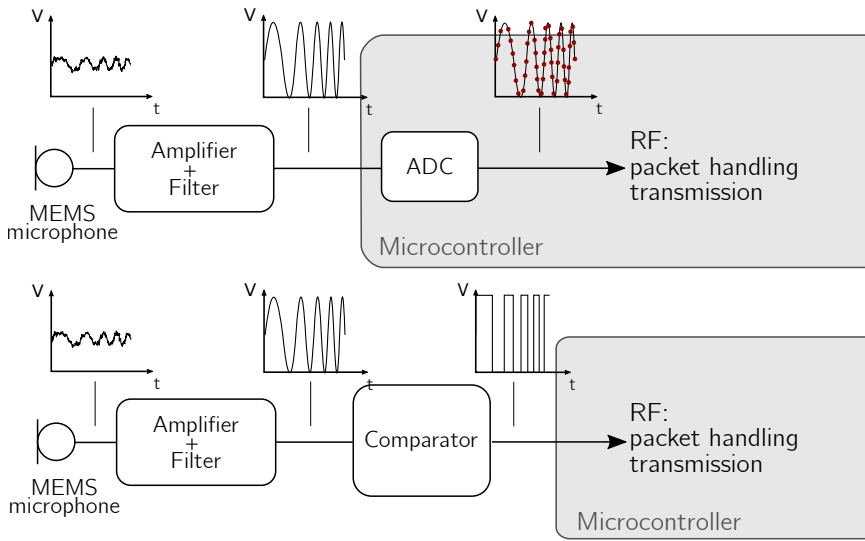
Figure 4.13: System architecture for both the convenient ADC based sampling technique and the zero crossing modulation solution.

To enhance the accuracy in a data efficient manner zero crossing chirp frequency demodulation [Nie13] is implemented. Recent progress in high-speed, low-power digitization and memory allow to time the zero crossings of the received sound signals and to process them locally. The most common technique is to fit the binary chirp data to a parabolic equation, which however handles noisy signals poorly. Therefore, a binary template cross correlation technique is used. Previous research has also proposed ADC elimination for passive, low-power, backscatter communication and sensing [Tal+17; Nad+18; VSV19]. These systems replace the functionality of the ADC by introducing comparators, adapting the transimpedance of a JFET or translating the voltage resolution to the time domain as a PWM signal. In this work we propose a different approach that offers a high resolution in the time domain rather than on voltage, as we aim to precisely detect the time instants of the zero-crossings directly on the received acoustic signal.

Figure 4.13 illustrates both hardware implementations, namely the convenient ADC based pulse compression technique and the newly adapted zero crossing demodulation. In the first setup, the sound signal recorded by the MEMS is filtered and amplified through a generic opamp. The microcontroller's internal ADC samples this signal and assembles the data in packets for efficient RF transmission. In the second architecture, a comparator is added to the development board. Here, a binary quantization is performed on the amplified and filtered audio signals

through comparison with a fixed DC level. The binary data is sampled through a generic digital input/output pin at a fixed frequency of 500 kHz. Packet handling with the improved method is straightforward and does not need splitting of the samples.

At the anchor side, the peak of the cross correlation is acquired by using a binary template based on the matching procedure of Sokal and Michener [Sok63] instead of the Fourier transformed cross correlation. If X and Y denote n-dimensional binary vectors, let

$$\delta_m(i,j) = \begin{cases} 1 & \text{if } x_m = i \ \& \ y_m = j \\ 0 & \text{if otherwise} \end{cases} \qquad (4.9)$$

for $i, j = 0, 1$ and x_m and y_m the mth elements of X and Y respectively. Let

$$n_{ij} = \sum_{m=1}^{n} \delta_m(i,j) \qquad (4.10)$$

That is, n_{ij} is the number of occurrences where $X = i$ and $Y = j$. Sokal and Michner define the similarity measure as

$$\mathbb{S}_N(X,Y) = \frac{n_{11} + n_{00}}{n} \qquad (4.11)$$

which is the ratio of the number of correctly matched 0's and 1's to the total number of binary samples. For a larger, p-dimensional binary vector Z the similarity measure is performed by binary shifting n-elements of this vector q-times, with $o > n$ and $q = p - n$. A maximum peak-seeking procedure defines the calculated distance and is obtained by searching the index I_{max} of the maximum similarity measure:

$$I_{max} = arg\,max_k \left(\mathbb{S}_N(X, Z_k) \right) \qquad \text{with } 0 < k < (p-n) \qquad (4.12)$$

The binary cross correlation matching method based on Eq. (4.9) is carried out as a bit-based XNOR operation between the -locally stored- quantized, broadcasted chirp and the binary sampled sound signal, resulting in a lightweight implementation. A rolling window is further applied to this stored chirp to obtain binary vectors with the same length as the recorded and quantized sound signal. The matching is done by summing the bit-based XNOR results (Eq. (4.11)) without normalization to eliminate an extra operation. Finally, the distance is calculated based on the correlation maximum (Eq. (4.12)). This method can be conveniently implemented on the mobile or anchor node, and is hence preferred over a power-intensive Fourier

transformed cross correlation technique.

Figure 4.14 depicts the results of the two correlation methods for measurements at a distance of 86 cm. The black line in these plots indicates the maximum correlation and its associated distance. With the same number of bits, 500 zero crossed bits which corresponds to 41 ADC samples at 12-bit per sample, the ADC cross correlation method has a lower pulse compression ratio, resulting in decreased accuracy and larger distance errors. Five times more bits are required to obtain similar results as with the bit based correlation method, as can be seen in the second plot in Figure 4.14. In conclusion, with the bit based correlation similar pulse compression results are obtained with a lower amount of bits, and giving a higher resolution in the time domain.

Note that with this zero-crossed method, a next step could be to transmit multiple spread spectrum codes from different anchor nodes simultaneously. These spread spectrum sequences could enable ranging to several anchors at the same time. Potential issues are the need for longer codes to obtain the same signal to interference ratio, resulting in longer awake time and more power consumption when the amount of anchors tranmsitting simultaneously is increased. This lies however outside the scope of this work.
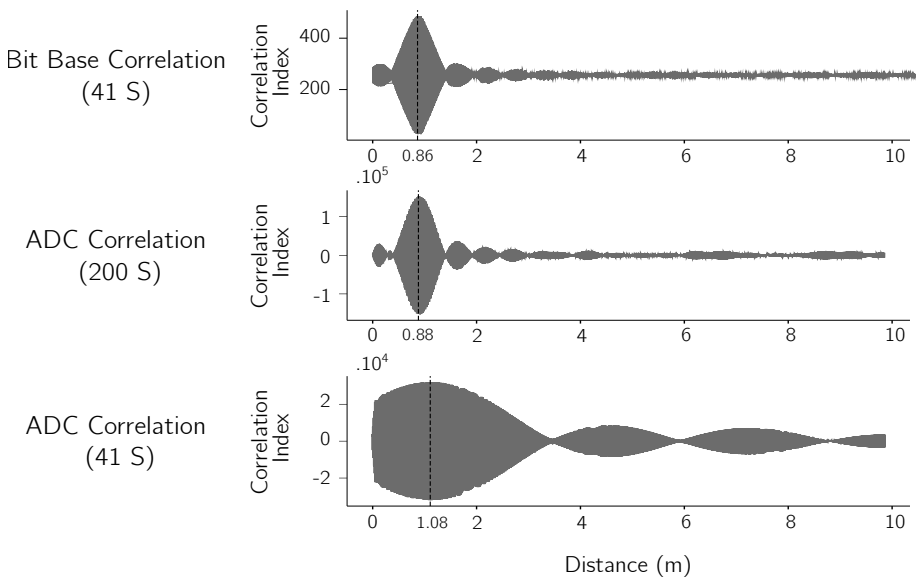

Figure 4.14: Results of the two correlation methods performed for measurements at a distance of 86 cm.

4.6.2   Performance comparison

Power Consumption

Both the conventional ADC sampling and the zero crossing approach are implemented on the CC1310 development board to gain insight into the possible lifespan of the mobile sensor nodes. A sample and communicate back approach is applied and further processing is done on the anchor node (here represented by a computer). The power measurements were performed with a Happy Gecko with the "Energy Profiler" in Simplicity Studio at a fixed supply voltage of 3.3 V.

Table 4.4 summarizes the power and energy consumed during the sensing, computing and communication operations for the binary sampling method (41 samples) and the ADC sampling method (200 samples). It shows that the binary sampling method is 4 times more energy efficient than the ADC sampling method. This large difference results from the fact that the latter method requires a larger transmit duration in combination with the high current drawn for RF transmission. The transmit duration is directly correlated to the payload, and thus the amount of sampling data. Note that the packet handling for the ADC sampling method is limited to splitting each 12-bit samples into two bytes. Improvements could be achieved by combining two samples into three bytes, which would still result in an energy consumption that is ∼180 µJ higher per measurement. The RF receiving energy consumption is the same for both techniques. Since the proof-of-concept lacks RF wake-up capabilities, an internal timer is used to leave the sleep state and force the node in an RF-listening state for a single millisecond. This enables low-power RF sensing but clock drift and jitter can have a major impact on the accuracy of both sampling methods when used during a longer operation period. Smaller contributions to the higher energy consumption come from the sampling and packet handling. This takes almost double the time for the ADC sampling method, while the current drawn in both cases is similar. For the acoustic hardware, the only difference with the hardware described in 4.5.1 is that in the binary sampling method a comparator is added to the circuit, hence the higher drawn current in active mode. This table confirms that computational energy is insignificant compared to the wireless communication impact, conform the statement in [Ana+08; Cal+21]. Calculating the lifespan of the mobile sensor node using this zero crossing demodulation method, it is estimated that it could operate 3795 days or ∼10 years on 3, 1.5 V AAA batteries of 2500 mAh when performing a single measurement per second and not taking into account self-discharge.

	Binary Sampling			ADC Sampling		
	Power (µW)	**Time (ms)**	**Energy (µJ)**	**Power (µW)**	**Time (ms)**	**Energy (µJ)**
Sleep	2.4	967.5	2.33	2.4	960.9	2.31
Sampling + Pkt Hand.	3 187.8	3.9	12.43	3 465	6.5	23.39
Rx	19 239	1.0	19.24	19 239	1.0	19.24
Tx	49 170	1.0	49.17	49 170	6.25	307.31
Acoustic	1 158.6	1.0	1.16	911.1	1.0	0.91
Acoustic Sleep	6.3	999.0	6.29	6.3	999.0	6.29
Total			**90.62**			**359.45**

Table 4.4: Power and energy comparison of the two sampling techniques implemented on the CC1310 launchpad with external components. The supply voltage was fixed at 3.3 V DC and the ranging update rate was fixed at 1 Hz.

Distance Measurements

Next to an energy based comparison, the two methods are assessed regarding their accuracy and precision in a realistic environment. The experimental setup consists of an anchor and a single node, both positioned at the same height in a high reverberant (average RT60 = 1,92 s) lab room of 8.35 x 16.44 x 5.19 m. The acoustic signal at the anchor was generated by National Instruments' NI-USB-6212 DAQ and amplified before it was broadcasted by the ultrasonic Fostex FT17H speaker. The frequency range of the band-pass chirp depends on the frequency response of both speaker and microphone. In this setup, a frequency range of 20 kHz is chosen, starting from 25 kHz and going up to 45 kHz. Sub-GHz wireless communication was implemented on the aforementioned CC1310 launchpad boards. In the bit-based correlation method, the distances were calculated on the anchor launchpad board. The cross correlation calculations for the ADC based method were performed externally in Matlab. Table 4.5 presents the Mean Absolute Error (MAE) and the standard deviation (σ) for 8 distances. The MAE indicates the accuracy of the measurements and is calculated by taking the absolute value of the difference between the actual and mean measured distance. The standard deviation specifies the precision of the system. At each of these 8 distances, 100 measurements were performed after tuning the transmit time of the RF wake-up signal. The reference distances necessary for the MAE were measured with a Bosch GLM30 [18] laser distance measurer.

With the exception of the smallest and largest distance, the binary and ADC 200 measurements have a comparable accuracy and precision. The error stays below 5 cm for ranging up to 7 m. A decrease in system performance at higher distances can be witnessed, mainly caused by attenuation. However, non-linearities

at the speaker frequency response can increase or decrease the distance locally (i.e. at 2 m versus 3 m). With increasing range, noise has a larger influence on the smaller received signals and cross correlation calculations result in several peaks with similar correlation indexes. Peak prominence methods could optimize the maximum selection to improve the distance measurements. Comparing the two techniques, the binary method performs best for both the smallest and largest distances.

When the amount of transmitted data for both techniques is matched and thus the number of ADC samples is reduced to 41, the accuracy remains within reasonable boundaries (< 25 cm for ranges below 9 m) but the standard deviation increases drastically, meaning that these measurements are evened out and not precise.

Distance (m)		0.20	0.50	1.00	2.00	3.00	5.00	7.00	9.00
Binary 41	MAE (cm)	0.5	0.5	1.2	1.6	0.7	4.8	2.8	62.3
	σ (cm)	1.1	1.4	1.0	5.0	3.7	2.2	3.1	237.3
ADC 200	MAE (cm)	5.6	1.8	0.7	3.2	1.9	8.3	47.6	116.5
	σ (cm)	1.3	1.9	0.9	3.7	2.9	2.0	3.1	254.4
ADC 41	MAE (cm)	4.0	2.3	1.0	6.1	8.4	19.3	24.2	667.6
	σ (cm)	11.2	11.5	8.9	20.3	34.6	36.3	58.8	225.4

Table 4.5: Distance accuracy and precision results at 8 distances of the two correlation techniques.

4.7   Conclusion

The hybrid ranging system concept introduced at the beginning of this chapter, addresses the three implications for energy-neutral devices. (I) Acoustic signals are received on the mobile node. Depending on the distance to the anchor, a low-power MEMS microphone at the mobile node receives a different part of the transmitted ultrasonic chirp. The acoustic chirp frequency swing is chosen based on the measured bandwith in the previous chapter. The RF signals are used for a synchronized wake up and communication. (II) The active time of receiver is limited to 1 ms. The awake time has a large influence on the pulse compression performed on the received audio chirp snippet. With a 1 ms receive window, the correlation peak is large enough and can be differentiated from its sidelobes. (III) By transmitting the received audio samples back to the anchor, and perform the distance calculations on this mains powered device, the mobile node is kept lazy. By implementing zero-crossing frequency demodulation on the mobile node, the

amount of data is reduced with a factor 8 when similar ranging results as the original method are obtained. This lowers the energy consumption 4 times.

Two simulation based performance analyses are performed in a ISM to show the influence of the real scenario constraints discussed in the previous chapter. Monte Carlo simulations show that with the 20 kHz bandwith limitation coming from the MEMS-speaker pair an accuracy of 1 cm can be obtained at an SNR level of 3 dB in an anechoic room. The second set of simulations demonstrate that the impact of reverberations is more discernible, showing an accuracy below 50 cm for half the ranging estimations in a highly reverberant room ($\alpha = 0.05$). Correct peak selection methods improve the ranging accuracy drastically, and the P95 ranging accuracy value is lowered 15 times.

A last contribution in this chapter comes from the ranging measurements assessments. The initial measurements in a real life environment show that for distances up to 3 m, a median error below 9 cm can be achieved. A second round of measurements performed with the zero-crossing frequency demodulation hardware shows that for distances up to 7 m, the mean average distance error can be kept below 5 cm.

The assessment performed in this chapter still uses energy-consuming RF chips for communication and synchronization. In the next chapter, backscattering and RF energy harvesting will be introduced to enable full energy neutrality on the mobile node.

Chapter 5

RF-Based Communication and Energy Provision

This chapter is adapted from:

- Cox, B., Buyle, C., Van der Perre, L., De Strycker, L. "Energy-Neutral Devices: Can Hybrid RF-Acoustic Signals Point Them Out?", 2020, 54th Asilomar Conference on Signals, Systems, and Computers, Pacific Grove, CA, USA. doi: 10.1109/IEEECONF51394.2020.9443432 [Cox+20b]

- Buyle, C., Cox, B., Van der Perre, L., De Strycker, L. "A Multi-band Solution for Interacting with Energy-Neutral Devices.", 2021, 55th Asilomar Conference on Signals, Systems, and Computers, Pacific Grove, CA, USA. doi: 10.1109/IEEECONF53345.2021.9723184 [Buy+21]

- Cox, B., Buyle, C., Delabie, D., De Strycker, L., Van der Perre, L. "Positioning Energy-Neutral Devices: Technological Status and Hybrid RF-Acoustic Experiments.", 2022, Future Internet 2022, 14, 156. doi: 10.3390/fi14050156 [Cox+22]

Contributions: The author and co-author Chesney Buyle drafted the original idea for energy harvesting, performed the formal analysis, contributed to the methodology and original paper writing, and conducted measurements in the first two manuscripts. In the latter manuscript, the author performed the preliminary research and analyzed the possible modulation and demodulation techniques that can enable backscatter communication in the proposed ranging system.

In this chapter, two RF related research courses that potentiate energy-neutral ranging are studied. The first section focuses on backscatter communications.

Compared to traditional RF communications, signals are no longer transmitted via a powered RF generator. In backscattering, incoming RF signals from a separate source are either reflected or absorbed to deliver information to another receiver. The main contribution to this work lies in the research of which modulation and demodulation technique can be adapted to backscatter the zero-crossed, acoustic binary data from the previous chapter. Additionally, a simulation-based assessment is performed to have insight on the radar cross section of common-used antennas. The theoretical study conducted in this section gives the necessary background for hardware development and measurements in the next chapter.

In the second section, RF energy harvesting is investigated for single band wireless power transfer. Accumulating energy from the surroundings to fill an energy buffer is one of the preconditions of an energy neutral device. A mathematical and simulation-based analysis within the European regulations is performed based on the path loss model of a COTS chipset. The last part of this chapter is a practical performance evaluation in a real-life environment to investigate the influence of the distance on the energy harvesting capabilities of this chipset.

5.1 Backscatter Communication

Antenna scattering theory has gained a lot of interest in recent years as a compelling research domain for (near) passive communications. In the course of the history, three large research waves can be distinguished. A great body of knowledge was obtained by military driven research, starting from the first deployment of radars in World War II [Sto48] to present-day stealth weapons and fighter jets [APR07]. It was in this era that 'The Thing', also known as the Great Seal bug, was developed [19]. Acoustic backscattering was used for spying on the American Ambassador in Moscow for over 6 years.
A second research wave on antenna scattering was initiated by Radio-Frequency Identification (RFID) systems. As the name suggests, the goal was to use antenna scattering (passive backscattering) for identification. The transportation sector was one of the early adopters, with examples such as the identification and tracking of railway carts and traffic management [Lan05]. Standardization enabled the unique identification of small objects with cheap tags that allow data encryption, collision resolution protocols, and error detection [Dob07]. In recent years, other groups of investigators have shown interests in this theory, aiming for more data-intensive wireless communication systems [NL19]. Eliminating active RF transceivers could resolve major hurdles in massive IoT and its future applications,

targeting near passive communication between sensor/actuator devices and the internet [Van+18; Kel+14]. Current research on backscatter communications can be divided into four categories. The first one focuses on the pathloss reduction of the backscattered RF signal. This would greatly increase the ranging capabilities of this technology. Examples can be found in [Zha+16] and [Var+17], where distances up to 3.4 km can be achieved. The second category researches higher backscatter data rates where WiFi backscattering currently can obtain speeds up to 5 Mbps [Bha+15]. A third research path can be found in using ambient signal sources instead of a dedicated signal source [Liu+13]. The transmission range in these systems is often lower and depends on the unpredictable and uncontrollable ambient conditions of the signal. The last research category is that of combining backscattering with energy harvesting to support self-sustainability of the mobile node.

In this section, the potential of backscattering approaches to achieve full energy-neutrality for ranging operations is elaborated, which can be further processed for determining the position of devices. Here a dedicated RF signal source will be used and data rates can be lower than current state-of-the-art. 500 kbps is sufficient enough to deliver the 500 binary, zero-crossed samples during the 1 ms awake time, as used in measurements in the previous chapter.

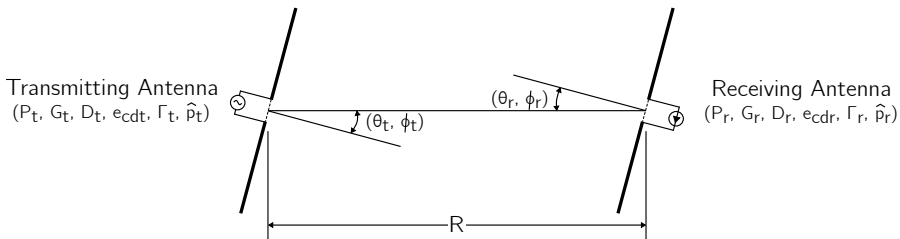Figure 5.1: Visual presentation of different parameters influencing the Friis Transmission Equation for far field received power calculations. (after [Bal05]).

5.1.1 Antenna Scattering

Backscattering is based on radar principles. For far field communication, analysis and design conventionally are based on the Friis transmission equation and the radar range equation. The Friis transmission equation relates the received power

to the transmitted power when two antennas are separated from each other in the far field ($R > 2D^2/\lambda$), with λ the wavelength and D the largest dimension of either antennas (Figure 5.1). Taking the directivity of the transmit antenna into account, the power density (W_t) at a distance R from the antenna is given by:

$$W_t = e_{cdt}\frac{P_t D_t(\theta_t, \phi_t)}{4\pi R^2}.$$
$$(5.1)$$

Here, P_t is the transmit power, $D_t(\theta_t, \phi_t)$ the directivity in the direction θ_t, ϕ_t and e_{cdt} the radiation efficiency of the transmit antenna. Similarly, the receive antenna has an efficiency (e_{cdr}), directivity ($D_r(\theta_t, \phi_t)$) and the effective area A_r can be described by:

$$A_r = e_{cdr}D_r(\theta_r, \phi_r)\frac{\lambda^2}{4\pi}.$$
$$(5.2)$$

Including the polarization losses ($\hat{p}_t$, $\hat{p}_r$) and antenna load mismatches (Γ_t, Γ_r), the received power becomes:

$$P_r = e_{cdt}e_{cdr}(1-|\Gamma_t|^2)(1-|\Gamma_r|^2)\left(\frac{\lambda}{4\pi R}\right)^2 D_t(\theta_t, \phi_t)D_r(\theta_r, \phi_r)\,|\hat{p}\cdot\hat{p}|^2\,P_t. \quad (5.3)$$

For reflection and polarization matched antennas, that are aligned within their maximum directional radiation and reception, the quotient of the received power over the transmitter power from Equation 5.3 can be rewritten as:

$$\frac{P_r}{P_t} = \left(\frac{\lambda}{4\pi R}\right)^2 G_t G_r.$$
$$(5.4)$$

With G_t and G_r respectively the transmit and receive antenna gain, a term incorporating both the directivity and efficiency. The far-field parameter used to characterize the scattering properties of a radar target is the Radar Cross Section (RCS): σ. According to [Bal05], it is defined as *a fictive area intercepting that amount of power, which, when scattered isotropically, produces at the receiver a density which is equal to that scattered by the actual target*. It depends on the relative position of target and transmitter/receiver, target geometry and material, frequency, angular orientation and transmitter/receiver polarization [KST04].

A more intuitive approach for the RCS in a bistatic setup, in which the transmitter and receiver at the infrastructure side are separated, is depicted in Figure 5.2. In this bistatic setup, R_1 represents the distance between the transmitting antenna and the backscatter device and R_2 the distance between the backscatter device and receiving antenna. The transmitted power (P_t) is observed by a target, at a distance R_1 from the source. The incident power (P_i) that is intercepted by the target is determined by the incident power density (W_i) and the cross section σ,
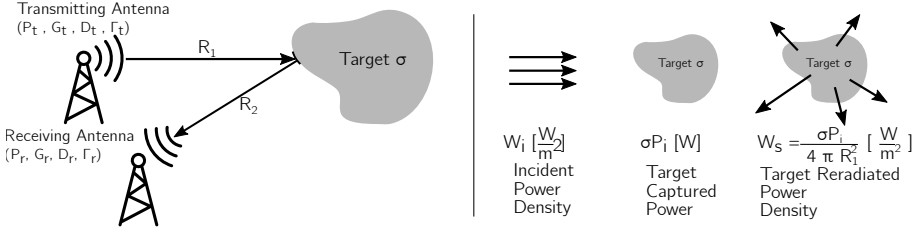
Figure 5.2: Simplified visualization of the Radar Cross Section (RCS).

so that the captured power is σW_i. This intercepted power is either reradiated as scattered power or absorbed as heat. Isotropical reradiation delivers a scattered power density (W_r) at distance R_2 from the target given by:

$$W_i = \frac{P_t}{4\pi R_1^2} \qquad (5.5)$$

$$W_s = \sigma W_i = \sigma \frac{P_i}{4\pi R_1^2} \qquad (5.6)$$

$$W_r = \frac{\sigma W_i}{4\pi R_2^2} \qquad (5.7)$$

Combining the above equations with the Friis transmission equation gives the relation between the radar cross section, the transmitted power of the transmit antenna and the received power by the receiving antenna as a function of the different distances and the RCS in case of polarization-matched and aligned antennas:

$$P_r = \sigma \frac{G_t G_r}{4\pi} \left(\frac{\lambda}{4\pi R_1 R_2} \right)^2 \qquad (5.8)$$

This equation is also known as the *Radar Range Equation*. A digital or analog signal can backscatter a received incoming wave by altering the RCS value (σ). The above equation provides a description of the RCS, but does not state clearly how it can be altered on a hardware level. In practice, the target is implemented as an antenna with an antenna gain (G) whose RCS can be altered. Green [Gre63] introduces a load-dependent radar cross section definition as:

$$\sigma_i = \frac{\lambda^2}{4\pi} G^2 \left| \Gamma_i - A_s \right|^2 . \qquad (5.9)$$

It contains two important design parameters: the antenna mode (Γ_i) and the structural mode (A_s). The antenna mode is load dependent:

$$\Gamma_i \triangleq \frac{Z_i - Z_a^*}{Z_i + Z_a}, \qquad (5.10)$$

where Z_a is the target antenna and Z_i the load impedance of this target antenna. The *antenna mode* describes the power absorbed in the load of a lossless antenna and the power which is reradiated by the antenna due to load mismatch. The second mode that was derived from Equation (5.9) is the *structural mode* (A_S) scattering term which depends on the antenna shape, size and materials [Ruc+70; Han89].

By varying the antenna load, only the antenna mode of the RCS value is altered, resulting in a changing electromagnetic field at the receiving antenna. For analog signals, a linear load, like the transimpedance of a JFET, can be changed depending on the incoming signal. For digital signals, the difference in RCS between a '1' and a '0' should be optimized for a maximal reading distance. The most convenient method would be to use the Thevenin equivalent circuit of an antenna [RNL05]. Solving this circuit for an antenna connector to a load Z_i ($i \in \{1, 2\}$) leads to a differential RCS $\Delta\sigma$ [NRM07]:

$$\Delta\sigma = \frac{\lambda^2 G^2}{4\pi} |\Gamma_1 - \Gamma_2| . \qquad (5.11)$$

This is only true for minimum scattering antennas, as noted carefully in [NRM07], where the antenna structural mode $A_s = 1$. Extended research on different modulation techniques (ASK, FSK, PSK , QAM in [Van+18]), shows that this is often (wrongly) supposed, neglecting the structural mode of the RCS equation, producing potentially sub-optimal reading distance results. Ideally, this should incorporate both the antenna and structural modes. However, complex measurements [BDS10] are necessary to determine the *structural* mode of the RCS. As a solution, the antenna is commonly switched between short and open state, trading the potential improved reading distance in for ease of use. The received backscattered signal is weak due to the energy loss when propagating, absorption by the antenna loads, the lower antenna gains in certain directions, and the negative influence of the structural mode. This makes the signal vulnerable to noise and fading.

RCS Values for Printed Circuit Board (PCB) Antennas

To improve the communication range when using backscattering, the difference between the RCS values ($\Delta\sigma$) obtained when switching between two load impedances should be maximized by accurate load selection. In RFID systems, antenna design is a matured topic as with a perfect impedance match between antenna and chip, the power transfer is maximized as well. In (ambient) backscatter communication, COTS components are used with different in- and output impedances, leading to a plethora of different antenna designs being adopted

in the prototypes. In this work, nine antennas are adapted and assessed after reference designs available in literature to get insight in the simulated RCS values for specific antenna characteristics such as size, bandwidth and impedance stability. Table 5.1 gives an overview of these adapted antennas with their calculated impedances, reflection coefficients (S_{11}), -3 dB bandwiths, reading distances specified in the referenced paper and maximum and minimum RCS values. The antennas are designed for the European 865-868 MHz UHF RFID band and single side PCB antennas are specifically chosen for their simplified design, simulation and production, and their attribution to the omnidirectional behavior of the antenna.

From Equation 5.9, it is clear that the structural mode (A_s) of an antenna can have a major impact on the $\Delta\sigma$. The load dependent antenna mode should be matched to this structural mode to get a maximum RCS swing. As aforementioned, this structural mode can not conveniently be determined theoretically and simulations or measurements are needed. [BDS10] shows that three RCS values are needed (σ_1, σ_2 and σ_3) for closed-form calculations of A_s. These RCS corresponds to the reflection coefficients obtained when the antenna is loaded with three different impedances. Out of equation 5.9, the three reflection coefficients are plotted as a circle on the Smith Chart:

$$(x - x_1)^2 + (y - y_1)^2 = \frac{4\pi}{\lambda^2 G^2}\sigma_1$$

$$(x - x_2)^2 + (y - y_2)^2 = \frac{4\pi}{\lambda^2 G^2}\sigma_2 \qquad (5.12)$$

$$(x - x_3)^2 + (y - y_3)^2 = \frac{4\pi}{\lambda^2 G^2}\sigma_3.$$

For the ideal case, row wise division between the above equations and calculating the intersection of these new circles gives a coordination pair (x, y) inside or outside the Smith chart, that corresponds to the unknown $A_s = x + jy$. When matching the antenna mode to this A_s value, the RCS goes to zero. The maximum RCS is obtained for the impedance located on the opposing side of A_s on the Smith Chart. The minimum and maximum RCS values from Table 5.1 are obtained by (I) performing time domain, small object, mono-static RCS simulations using far field, broadband plane waves (0.5 - 2.5 GHz) for antennas loaded with an open, complex conjugated and reactive load, (II) obtaining the A_s point by intersecting the plotted reflection coefficient circles on the Smith chart and (III) performing new RCS simulations with the obtained A_S dependent impedances to find the σ_{min} and σ_{max} values.

From this table, it can be concluded that size has the largest influence on the obtained RCS-values. For small antennas, the simulated values lies below 0.100 m²

and only the 44×15 cm bowtie antenna has a RCS value larger than 0.5 m². It is however unpractical for mobile nodes to have such a large backscatter antenna. The dipole antenna has the highest performance when the total area is selected as parameter for the obtained RCS comparison. Note that at some points, σ_{min} is larger than zero, showing that the structural parameter could not be derived precisely from the intersection point on the Smith Chart.

A practical assessment of these RCS values is difficult to perform without specialized hardware [20] and in true to life environments [Shr+08]. Parasitic influences on the designed PCB-antennas and tolerances of the frequency dependent impedances make for ill conditioned structural antenna mode calculations. However, in [BDS10] it is stated that any diametrically opposite load on the Smith Charts' unit circle minimizes the Bit Error Rate (BER) probability at the anchors for a given antenna. Therefore, a dipole antenna will be used in this work which will be loaded with an open and shorted circuit.

5.1.2   Backscatter Modulation

In the system description described in Section 4.6, the zero crossed, binary chirp snippets contain the necessary data to perform the ranging measurements. RF backscattering exploits the instantaneous character of electromagnetic waves and can transmit the received information embedded in the acoustic signals directly to an anchor node for further processing. The frequency of the received acoustic signals should get modulated on an RF signal.

Load switching of a single-tone incident wave is adopted in this work as it presents the most simple form of Amplitude Shift Keying (ASK) modulation i.e., On-Off Keying (OOK). It is easy to implement, inexpensive and has demonstrated its ability to perform backscattering in several wireless technologies [ER15; Iye+16]. However, this modulation method has a major drawback, namely it is highly susceptible to noise. In the time domain, an RF source sends out the carrier wave $S(f_c, t)$, a single tone sine wave with a frequency f_c, and the backscatter device changes the RCS at a frequency of Δf_a. This latter represents the received acoustic chirp in the time window τ_{rx}. A_1 and A_2 represent the path loss of the electromagnetic waves. In the bistatic setup, a separate antenna receives the sum of the carrier wave and the basckattered OOK demodulated signal:

$$R(t) = A_1 \, S(f_c, t) + A_2 \, \sigma(\Delta f_a, t) \cdot A_1 \, S(f_c, t) \tag{5.13}$$

As backscattering is a mixing process, the OOK backscattered signals appear as sidelobes on the positive and negative side of the single-tone carrier wave in
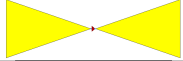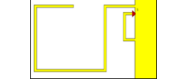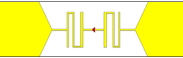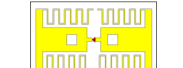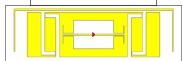
Antenna Type	Source	size (mm)	Impedance (Ω)	S11 (dB) Matched	-3 dB BW MHz Matched	Reading Distance (m)	σ_{min} (m²)	σ_{max} (m²)	Feature	Design
Dipole	[Liu+13]	150 x 15	54.78 + 1.37j	-45.24	272.72	/	0.001	0.079	Reference Design	
Meander Dipole	[RNL05]	166.7 x 30.3	14.48 - 14.21j	-11.97	33.11	5	0.011	0.012	Reference Design	
Bowtie	[Das+16]	440 x 150	170.13 + 1.46j	-39.94	359.32	/	0.026	0.515	Reference Design	
PiFA	[FLL13]	120.6 x 52.2	9.15 + 35.68j	-12.49	85.01	8.06	0.003	0.070	Reference Design	
Folded Monopole	[AA12]	51.8 x 33.6	48.16 + 50.15j	-30.77	63.54	6.3	0.001	0.045	Size	
Meander Stubbed Dipole	[ST06]	44.3 x 72.9	18.80 + 5.25j	-41.87	104.07	4.6	0.002	0.070	Impedance Stability	
Dual Band	[Ma+12]	123.8 x 74.3	75.93 - 14.52j	-33.70	169.28	6.8	0.001	0.097	Bandwidth	
Broadband	[Ham+17]	110 x 35.3	9.93 - 192.92j	-18.64	79.53	11.8	0.006	0.084	Bandwidth	

Table 5.1: Overview of the antennas designed and simulated to gain $\Delta\sigma$ insights.

the spectrum. In other words, the reflective and incoming wave spectra overlap. This approach suffers from self interference as Δf_a is relatively small, and without proper cancellation can not be distinguished from the carrier wave due to the limited resolution of the receiver. This becomes apparent when two or more nodes are available in the same backscatter network. Not only can there be in band interference between the transmitted and reflected signal, but between different backscattered signals as well. With increasing distance, these signals ultimately become too weak to be separated from the noise floor or from out-of-band interference.
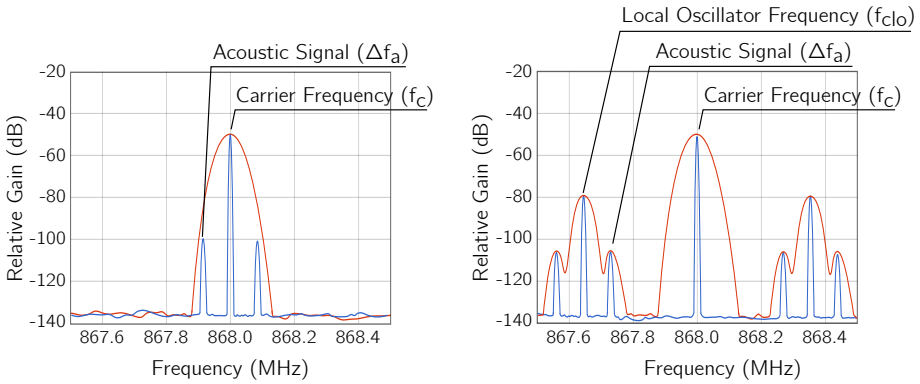
Figure 5.3: Frequency spectra of the combined direct and backscattered received RF signals without the local oscillator at the backscatter device (left). The blue and red lines on both figures represent the spectra for respectively a small and a large resolution bandwidth. By adding the local oscillator, the backscattered signals are shifted away from the carrier, improving distinctiveness and enabling reception at lower spectral resolution.

A solution for the two self-interference problems is achieved through frequency translation backscatter [Var+17], where mixing capabilities of the backscatter principle are used to its advantage. This requires an extra component on the backscatter device. A local oscillator, generating a sine wave at a frequency f_{clo}, moves the signal away from the direct carrier in the frequency domain. The offset of $f_c \pm f_{clo}$ can be seen at both sides. On these two mirror frequencies, the received acoustic chirp signal again appears as a double sideband modulated signal. In total, four mirror frequencies of this acoustic signal can be seen in Figure 5.3. Assuming the RCS variation is defined by a sine wave, the second

term of Equation (5.13) can be rewritten with the product to sum identities as:

$$\sin(f_a\,t) \cdot \sin(f_{clo}\,t) \cdot \sin(f_c\,t) =$$

$$\frac{1}{4}\Big(\sin\big((f_c - \Delta f_a + f_{clo})\,t\big) + \sin\big((f_c + \Delta f_a - f_{clo})\,t\big)\Big) \qquad (5.14)$$

$$-\frac{1}{4}\Big(\sin\big((f_c - \Delta f_a - f_{clo})\,t\big) + \sin\big((f_c + \Delta f_a + f_{clo})\,t\big)\Big)$$

The added local oscillator contributes to a higher power consumption, yet it is an excellent compromise for the gained reading distance, Additionally, it allows for a multiple access implementation. By selecting a different local oscillator frequency for each mobile node, FDMA can be adapted. However, due to the double side band modulation, the maximum amount of simultaneous localized nodes defined by both the acoustic chirp and RF bandwidth is halved. Complex single sideband mixers, such as in [Wan+20a] with two separate loads could cancel out one band but at the same time consume more energy and require a larger complexity on the mobile node. Carrier sensing can be performed at the signal generator, sensing the RF spectrum and selecting the carrier frequency at which the chance of possible collisions with ambient wireless traffic is lowest.

Backscatter Demodulation

As this proposed method does not require any complex self-interference cancellation mechanism on a hardware or software level, a simple radio can be used to demodulate the backscatter signal to retrieve the acoustic information out of the RF-signal at the anchor node. With the addition of the local oscillator on the backscatter device, two types of demodulation can be performed:

1. OOK demodulation. The digitized acoustic signal drives a multiplexer that forwards either the local oscillator or no signal at all. Consequently, the load is switched at the local oscillator frequency f_{clo} or it does not get switched. In the spectrum, this appears as a signal f_{clo} away from the RF carrier frequency that gets turned on and off. As aforementioned, OOK is very susceptible to noise, and the drift of the local oscillators can make the amplitude demodulation on the receiving radio impossible.

2. Frequency Shift Keying (FSK) demodulation. As the acoustic chirp Δf_a can be considered as a signal modulated in frequency, this chirp signal can be observed on both sides of the local oscillator frequency. The demodulation is often done by performing a frequency translation and a decimating FIR

filter on one of the sidebands. With this, only the portion of the wideband signal with the frequency decreasing chirp signal is saved to a buffer for later use.

In this research, FSK is used for demodulating the backscattered acoustic signal. This constant envelop modulation is more robust against fading and non-linear amplification. Additionally, FSK can achieve a lower BER for the same signal-to-noise ratio. In Figures 5.4 and 5.5, a snapshot of both the spectrum and the received signal of an acoustic backscattered signal in the time domain can be observed. The two sides of the spectrum are plotted, clearly showing the powerful RF carrier wave, the local oscillator frequency, and the two acoustic sidebands.
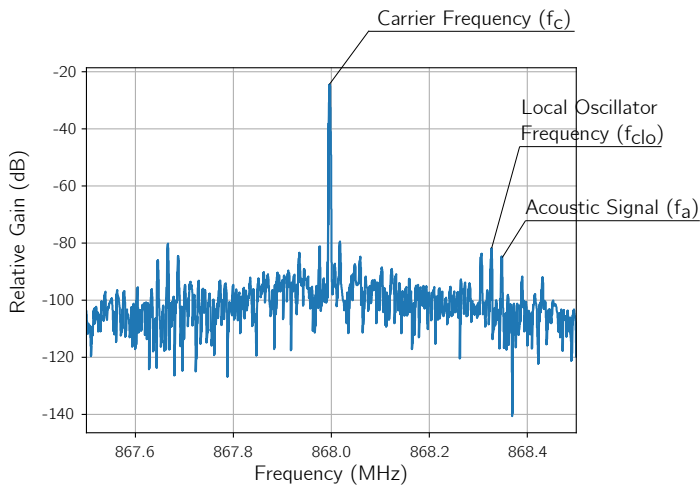
Figure 5.4: Spectrum of received backscattered signal, showing the two symmetric sidebands with the RF carrier frequency as center.

5.2 Energy Harvesting

Next to the optimization of the energy consumption of the device by means of improved data compression suggested in Section 4.6, communication schemes discussed in Section 5.1 and hardware design, a second research direction can be followed to enable energy-neutral devices: energy harvesting. For outdoor applications, energy harvesters with a high power density such as solar panels and wind turbines are chosen. However, indoor environments typically do not have access to these energy sources and LPS have to rely on other, less efficient methods
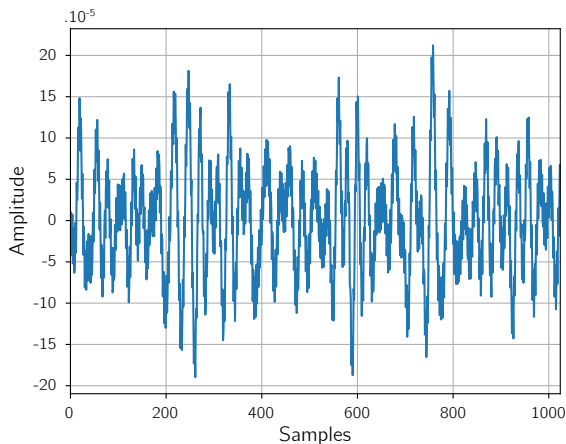
Figure 5.5: 1 ms of samples from an FSK-demodulated acoustic backscattered signal in the time domain before cross correlation is performed.

for energy-neutral operation. A solution with great potential can be found in RF harvesting as it enables energy and information transport simultaneously. This latter is also known as Simultaneous Wireless Information and Power Transfer (SWIPT). As there is a continuous sine wave present for backscatter communication coming from a mains powered anchor, the received energy at the mobile node could be harvested when the positioning hardware is not active, storing it in an energy buffer for when the system wakes-up and needs power. This requires an adaptation in the RF wake-up signaling. In the previous chapter, a short positive rectangular pulse was used to simulate the synchronized wake-up. In order to get a continuous wave to be present the whole time for harvesting purposes, a negative rectangular pulse can be used again, meaning that synchronization should be done on the sudden disappearance of the RF signal. This discontinuity should be short as the continuous wave is used for backscatter communication after this synchronization and shows that no real SWIPT can be implemented if this RF signal is used for synchronous wake up as well. A fast, negative envelope detector should be added to the energy harvesting circuit to function as synchronization hardware [Li+21c].

The overview paper of [Lu+15], reviews research on dedicated antenna, matching network, rectifier and architecture design. Recent developments on dual band [Li+21a; Li+21b], multi-[Vu+20] and broadband [Liu+20] systems, show that a high efficiency (up to 71% of the received RF power) can be obtained with

these dedicated designs. In this section, energy harvesting is tackled by a more practical implementation approach. An off-the-shelf energy harvesting chipset (E-Peas AEM 40940 [21]) was chosen with a Power Management Integrated Circuit (PMIC) containing the necessary rectifier, converters and energy storage controllers, is used in combination with commercially available dipole antenna.

5.2.1 Mathematical and Simulation-Based Analysis

In this section, the performance of the system is evaluated mathematically and through simulations in terms of the tag's charge time, i.e. the time it takes for the beacon to pre-charge the tag's E-buffer with sufficient energy to perform one ranging measurement. Firstly, a suitable size for the tag's energy buffer is determined in accordance with the design guidelines of an off-the-shelf RF energy harvester. Secondly, some insight is given regarding the regulations regarding the 868 MHz band the system is operating in. Lastly, the charge time of the proposed system is simulated based on the generalized Friis transmission formula and measured in a real-life indoor setup.

Energy Buffer Size

Figure 5.6 depicts a schematic overview of transmit and receive side with at the mobile node the different building blocks and their according efficiencies. Energy coming from an anchor point travels through free space, and is received by a dipole on the mobile node. There, a matching network equals the antenna impedance with the input impedance of a rectifier. This latter alters the AC voltage to a low DC voltage, which is then increased to a higher voltage with a boost converter. An internal Low-Dropout voltage regulator (LDO) regulates the voltage for the energy buffer. The energy harvester's E-buffer must be sized carefully. An oversized energy buffer may require a long time to reach the targeted voltage, while an undersized energy buffer contains too little energy to perform the system operations. A capacitor is chosen as energy storage element due to the limited energy need at the mobile tag and its fast charging capabilities. An RF input power between -19 dBm and 10 dBm is necessary at the input of the energy harvester to start charging the capacitor. The size of the capacitor depends on two voltage levels: V_{chrdy} is the minimum starting voltage on which the energy stored in the capacitor can be used. The voltage over this capacitor slowly degrades until it reaches V_{ovdis}, at this point it stops delivering power to the rest of the mobile node's hardware. These two voltages are the boundaries on which power will be delivered, which are subject to the hybrid RF-acoustic

hardware. For a capacitance set to 22 µF with $V_{chrdy} = 3.10\,\text{V}$, $V_{ovdis} = 2.8\,\text{V}$, and worst case LDO efficiency η_{LDO} of 74 %, the necessary storage energy to be harvested can be calculated as:

$$E_{store} = \frac{C \cdot (V_{chrdy}^2 - V_{ovdis}^2)}{2} = 19.5\,\mu\text{J} \tag{5.15}$$
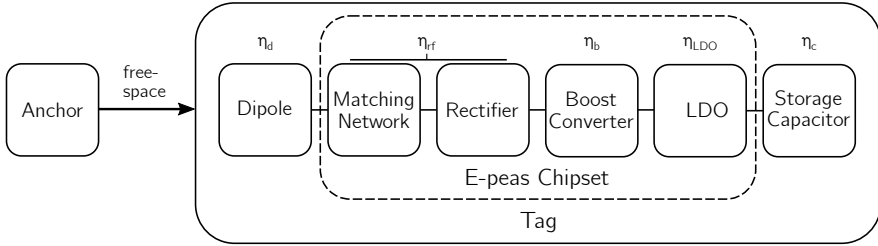
Figure 5.6: Overview of the link budget between anchor and mobile node with the different PMIC elements and their efficiencies.

Regulatory Analysis

Although regulatory limitations have a significant impact on existing technologies, these are often overlooked and left unexplored in current scientific literature [Sae+19]. The harmonized European standards for transmission in this band can be found in ETSI EN 302 208 V3.1.1 [22]. An overview of the available frequency bands can be found in Figure 5.7. Transmission in the 863 to 870 MHz band is determined by two parameters: the maximum allowed transmission power and duty cycle ratio. The frequency band considered for RF power transfer is the 868 MHz RFID band as it allows transmissions with relatively high transmit power (up to 2 W) and duty cycle.

The duty cycle restrictions are imposed in the form of a maximum transmit time or as polite spectrum access. The first is measured by the total time on which there is transmission in a certain observation period (1 hour). The duty cycles range from 0.1 % to 10 %. However, continuous transmission is preferred for power transfer to keep the mobile tags charged at all times. Polite spectrum access allows for longer transmission, but adds extra complexity to the system as Listen Before Talk (LBT) and Adaptive Frequency Agility (AFA) should be implemented. Therefore, transmitters may operate in a presence-sensing mode in which they perform periodic transmissions to verify whether new mobile tags are

present. In this mode, continuous transmissions of maximum 1 s are interleaved with silent periods of at least 100 ms.

In RFID, the maximum Effective Radiated Power (ERP) is stated to be 2 W. However, an additional limitation on this ERP comes from the beam width of the transmit antenna in the horizontal orientation [22]. In the case of omnidirectional transmission, the ERP shall be 500 mW at maximum (27 dBm). When the beam width is less than or equal to 180°or 90°, the ERP of the transmitter can be increased to a maximum of 1 W and 2 W respectively. This 2 W is still an ERP, and the sum of the antenna's input power and directional gain should not exceed 33 dBm.
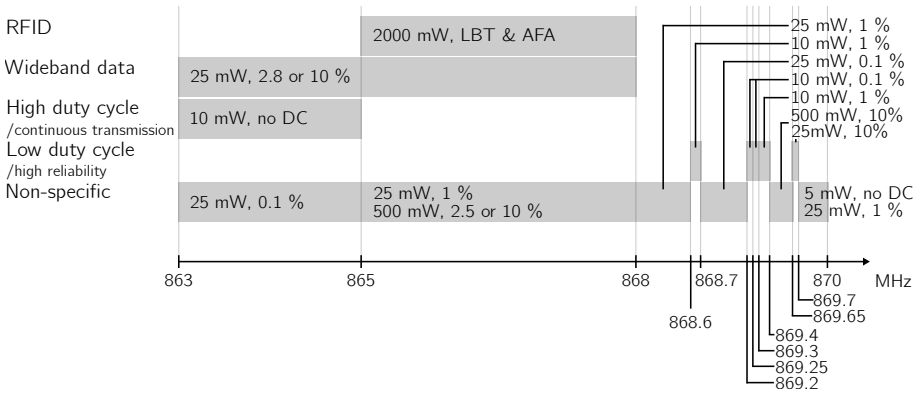
Figure 5.7: Overview of the available frequency bands between 863 and 870 MHz. For each band, the maximum transmission power and duty cycle are given. (After [Sae+19])

Theoretical Performance Assessment

A performance analysis of the RF WPT system is made in terms of the tag's charge time, i.e. the time it takes for the transmit beacon to charge the tag's storage capacitor with sufficient energy to perform ranging measurements. The quantified requirement of the energy consumption stated in Section 1.2.2 is set to 16.5 μJ. Two performance parameters are considered:

1. Initial charge time = time required for the energy harvester to charge the storage capacitor from 0 V to V_{chrdy} = 3.1 V. This scenario takes place when the tag has not been charged for a long time.

2. Update charge time = time required for the energy harvester to charge the storage capacitor from V_{ovdis} = 2.8 V to V_{chrdy} = 3.1 V. This scenario takes place when the tag was recently or is continuously powered.

The calculations of these charge times are based on the Friis transmission formula and E-peas AEM40940 energy harvesting efficiency.

$$P_{harvest} = \eta_{tot} \frac{G_t G_r P_t \lambda^2}{(4\pi d)^2} \quad (5.16)$$

Table 5.2 summarizes the different efficiencies of the link budget in the receiver. Both the efficiency of the dipole (η_d) and the internal RF path efficiency (η_{rf}) are frequency dependent. The first one defines how well the radiated power is converted into supplied power, and depends on conduction and dielectric losses. The efficiency of an antenna can be read directly from the datasheet. The second is defined as the ratio between the power coming out of the rectifier and the power entering the RF-matching network. The internal boost converter (η_b) and LDO (η_{LDO}) lower the total efficiency further. Lastly, there are almost no losses in the charging capacitor. This is due to the low Equivalent Series Resistor (ESR) of the chosen aluminum polymer capacitor, which has the largest influence on the efficiency of a capacitor as storage element. At the transmit beacon, a continuous wave (CW) at the frequency of 865.7 MHz is considered. Two antenna scenarios are considered at the RF-source: an omnidirectional dipole antenna with a gain of 2.15 dBi or a directional antenna with a maximum gain of 6 dB. The ERP (P_t) is for these scenarios respectively limited to 27 dBm or 33 dBm, depending on the transmit antenna's beam width. No transmit duty cycle limitations are considered.

Frequency	η_d (%)	η_{rf} (%)	η_b (%)	η_{LDO} (%)	η_c (%)
868 MHz	75.17	37.78	73.80	74.07	99

Table 5.2: Efficiencies in the receiver's link budget for a receive power of -10 dBm and at a transmit frequency of 865.7 MHz.

Figure 5.8 shows the simulated initial and update charge times in function of the beacon-tag distance for the two considered ERP scenarios. When a mobile tag enters the RF field of the WPT system with a depleted storage capacitor, it would take the omnidirectional base charging system around 10 s to power up the tag at a distance of 5 m. Once the initial charge is overcome, the base charging system is able to initiate a ranging measurement every 2 s for the same distance. If a higher update rate is desired, the directional boost charging system can be

used. However, this requires prior knowledge of the position and a beam steering mechanism at the transmit side. In the directional case, it takes only around 0.4 s to obtain the necessary energy to fill the energy buffer at 5 m distance. When taking the duty cycle limitations implied by the regulations into account, the total duration would become 1.1 times longer in the best case scenario.
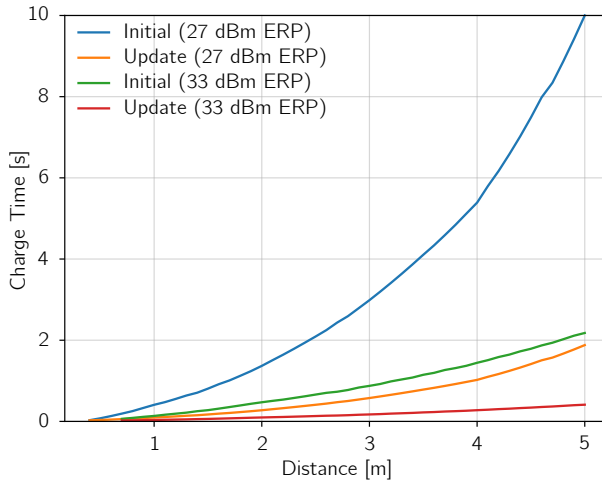
Figure 5.8: Simulated initial and update time of the two antennas, in function of the distance

5.2.2 Practical Performance Assessment

A practical performance evaluation is performed in the multi-functional Techtile infrastructure. This is a 8 x 4 x 2.4 m³ modular structure built for distributed sensing and communication technologies [Cal+22] with 140 tiles covering the walls, ceiling and floor, each equipped with a power, radio, processing and communication module. A DAQ-setup with 384 single ended, synchronized, 16-bit, analog input channels enables fast sampling (3.3 MS/s) of sensors and actuators. This offers a true to life, modular testbed for both acoustic and RF-based research. In this room, the dipole and directional transmit antennas are alternately placed in the center on a 1 m height. A 865.7 MHz continuous sinusoidal wave coming from an RF power amplifier is fed into these antennas. At the mobile device, the same dipole antenna was connected to an E-peas AEM40940 energy harvester board. As an energy buffer, a slightly larger aluminum electrolytic capacitor of 39.7 µF

was used. According to Equation (5.15), the energy buffer is increased to 35.1 μJ.

Two measurement campaigns were conducted. The first campaign consisted of measuring the initial charge time for both the omnidirectional and directional antenna configuration. This is the time interval measured between the start of RF transmission at the beacon and the moment at which the energy harvester charged its storage capacitor from $0\,V$ to V_{chrdy} (2.3 V). The second campaign evaluated the update charge time of the WPT system, i.e. the time interval measured between the start of RF transmission at the beacon and the moment at which the energy harvester charged its storage capacitor from V_{ovdis} to V_{chrdy}. In accordance with the ETSI regulations, the ERP for the omnidirectional antenna configuration was set to $27\,dBm$ For a dipole antenna with maximum gain of 2.15 dB, the transmitted power is set to $24.85\,dBm$ or $305\,mW$. In the case of the directional patch antenna configuration, the ERP was set to only $31.9\,dBm$ due to limitations of the used RF power amplifier and lies below the $33\,dBm$ ERP regulation for directional antennas with a beam width below 90°. In each scenario, the distance between the transmitter and receiver was sequentially increased in steps of $25\,cm$, starting from $0.5\,m$ and up to the border of the Techtile room at $4\,m$. At each distance, the considered charging time was measured 25 times and the measurements using the omnidirectional and directional antenna configurations were conducted separately in order to prevent interference.

Figure 5.9 shows the mean initial and update charge time of both transmit antenna configurations in function of the distance. The initial charge time lies in both cases substantially higher than their update charge time counterpart. In the most unfavorable scenario, that is with omnidirectional transmission and initial charging, a full charge of the energy source can be achieved every $40\,s$, with exception at $3.5\,m$ distance. The exponential development as seen in the simulations of the initial omnidirectional graph can be seen in the measurements as well. This latter has outliers in both positive and negative direction due to interference and the charge times are around 5 times as high, but the overall exponential trend is present. If the position of the mobile node is known prior, a directional beam can be pointed towards the mobile node, resulting in an update charge time falling below $2\,s$, except at the distance of $4\,m$. These results do not incorporate the European duty cycle regulations. Again, in best case scenarios, the total duration will be prolonged 10%.
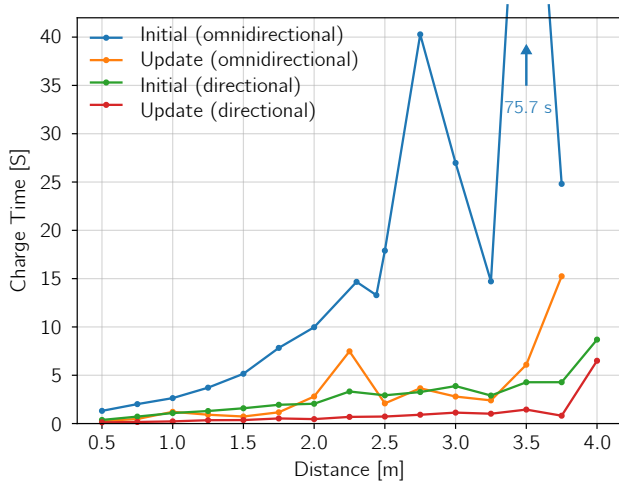
Figure 5.9: Measurements of the initial and update time in function of the charging distance for the two antennas.

5.3 Conclusion

In this chapter, two RF-based approaches are investigated that contribute to the energy-neutrality of mobile nodes in the proposed hybrid ranging system. The binary, zero-crossed acoustic data from the previous chapter can be used to change the antenna load, resulting in the absorption or reflection of an incoming RF wave. The structural mode of the backscatter antenna is unconsidered as this is difficult to measure and antenna mode scattering is implemented by choosing the antenna load between an open and short circuit. For the hardware design in the next chapter, frequency translated backscattering is suggested as this eliminates self-interference and improves detection for RF receivers with a large resolution bandwidth. An extra local oscillator shifts the signal away from the more prominent carrier frequency. The received data at a second RF receiver should be demodulated with FSK, as this achieves a lower BER. Additionally, a PCB dipole antenna is suggested as backcscatter antenna, as the size-to-RCS ratio is high for this given antenna.

From the simulations and measurements it is shown that energy harvesting is viable for distances to at least 4 m, the boarder in the indoor environment. The chosen chipset can fully charge an energy buffer of 35.1 µJ below 44 s within the

most favorable European duty cycle regulations of the 868 MHz band. In case of a directional antenna, this initial charge time decreases to 15 s and even to 2 s when the capacitor needs an update charge. The energy consumption of next chapter's hardware design will tell if this energy buffer is sufficiently large for a single distance measurement.

Chapter 6

Towards Hybrid RF-Acoustic 3D Indoor Positioning

This chapter is adapted from:

- Cox, B., Buyle, C., Van der Perre, L., De Strycker, L., "Towards Centimetre Accurate and Low-Power, Hybrid Radio-Acoustic 3D Indoor Positioning: an Experimental Journey.", 2021, CEUR Workshop Proceedings, Indoor Positioning and Indoor Navigation (IPIN), Lloret de Mar, Spain.

- Cox, B., Buyle, C., Delabie, D., De Strycker, L., Van der Perre, L. "Positioning Energy-Neutral Devices: Technological Status and Hybrid RF-Acoustic Experiments.", 2022, Future Internet 2022, 14, 156. doi: 10.3390/fi14050156 [Cox+22]

Contributions In both manuscripts, the author designed the hardware, conducted the measurement campaigns and wrote the original paper drafts. Co-authors participated in the discussions regarding the obtained results and contributed to the review and editing of the original manuscripts.

In this last chapter, the low-power, hybrid RF-acoustic of the mobile node hardware is presented based on the insights and requirements of the previous chapters. In the first two section, two types of measurements are performed. In Section 6.1 the power consumption of the proposed hardware is assessed and compared with energy retrieved from the RF harvesting circuit to investigate if energy-neutral ranging measurements are possible. The second series of measurements, performed in Section 6.2, examines the impact of the RF backscattering on the precision and accuracy of the developed hardware. Lastly, Section 6.3 extends the ranging

system to enable 3D positioning. Five established indoor positioning algorithms are introduced and applied on spatial dispersed ranging measurements to evaluate the positioning capabilities of this system in a real life scenario. This section is concluded by recommendations to achieve the cherished centimeter accuracy.

6.1 Hardware Implementation and Power Consumption.

In this section the concept and results from Chapter 4 and 5 are combined into a hardware implementation of the frequency shifted, load switching backscatter mechanism for zero crossing chirp fragments. The improved, low-power hardware design is next to data reduction, efficient communication and energy harvesting, the last pillar for energy-neutral operation of the mobile nodes. Care should be taken in optimizing the hardware design, leaving out unnecessary components and searching for the component with the lowest energy consumption. Since the system design imposes an RF wake-up signal, the lowest energy consumption incorporates not only the active power consumption, but wake-up times as well. Next to the hardware design and component selection, the power consumption and linked energy consumption of the contributing elements are evaluated.

6.1.1 Hardware Implementation

Previous implementations [Wan+20a; Lin+21; Kuo+22] demonstrate the backscatter capabilities for IoT applications based on custom Integrated Circuits (ICs). Their small form factor and ultra-low power consumption, often orders of magnitude lower than systems built with lumped components, are attractive features. Due to time and resource constraints in prototyping for R&D, off-the-shelf components were used, selecting options with low-energy consumption in both the active and sleep/passive usage. An overview of this system is depicted in Figure 6.1 and can be divided into two parts: (I) the acoustic section in which the analog, ultrasound signals are captured and transformed via zero-crossing into a digitized version, and (II) the RF section, which uses these digital signals to switch the load of the antenna. The total cost of this designed prototype, including component and PCB cost, is € 14.81 for a single mobile node at the time of writing. This cost will greatly decrease when mobile nodes are mass produced.
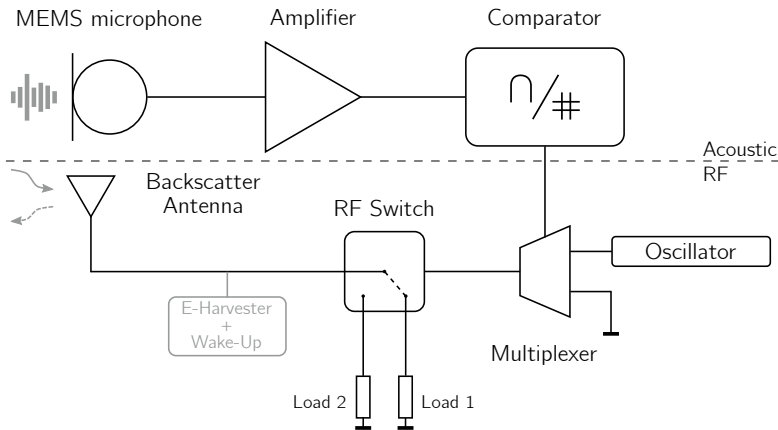
Figure 6.1: Schematic overview of the different components. A distinction between the acoustic (top) and RF part (bottom) can be made.

Acoustic Hardware

The acoustic section consists of:

- MEMS microphone (Vesper VM1000 [5]): out of Table 3.1 the key specifications next to the low power consumption are the short wake-up time (below 200 μs), the high sensitivity, and the wide frequency response. Note that the short wake-up time has the largest impact on the wake-up energy consumption and makes up for the higher power consumption of this MEMS microphone. In house measurements in Figure 3.7 show that frequencies over 80 kHz can be received sufficiently, much higher than stated in the audible domain focused datasheet.

- Amplifier (TLV341 [14]): this low-noise amplifier has a high Unity Gain Bandwidth (UGB), providing a gain up to 34.8 dB for a 40 kHz signal in a single stage. Amplifying and filtering before zero-crossing by the comparator is more noise resilient and gives therefore better results. The single supply, rail-to-rail capability of this opamp makes for an easy implementation and for maximum signal amplitude swings.

- Comparator (TLV7031 [23]): the rise and fall time are specified below 5 ns, giving a quasi-instant change of state when a zero-crossing occurs.
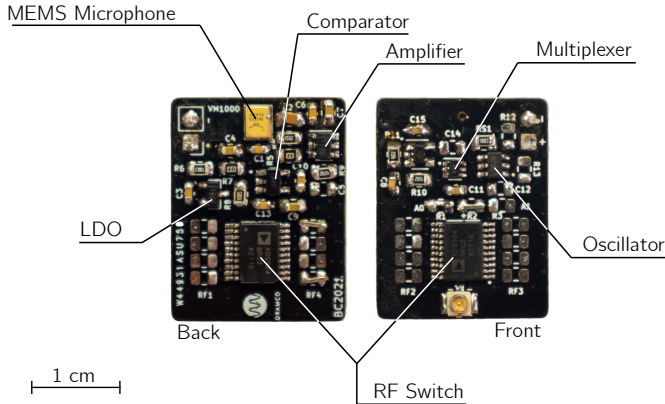
Figure 6.2: Designed PCB of the proposed backscatter module.

RF Hardware

The output of the comparator, containing the digitized microphone signal, is connected to a Single Pole Double Throw (SPDT)-switch (ADG839 [24]). This acts as a multiplexer, passing either the local oscillator signal (LTC6906 [25]) with a frequency of f_{clo} or a low voltage signal. The local oscillator frequency is set with two resistors, and can take values between 10 kHz and 1 MHz. Implementing double sideband frequency modulation as explained in Section 5.1, a total bandwith of 80 kHz is necessary per mobile node, defined by the maximum chirp frequency $f_{a,max} = 40$ kHz. With the local oscillator bandwidth limitation of 1 MHz, this allows for only 12 backscatter nodes to be active at the same time in the same acoustic area when FDMA is implemented. The last part of this RF hardware section are the RF load switches (ADG904 [26]). An external dipole PCB antenna connected to the antenna port of the backscatter module, consists of two $\lambda/4$ copper strips with a small gap between them. For this antenna at least two load switches are required to correctly short and open these two sides. The ADG904 has four multiplexer channels. This means there are two more multiplexer inputs available on both of these chips. This makes it possible for other resistors, inductors and capacitors to be used as a complex, serial load between the two copper traces, enabling additional antenna loads for improved reading distance as proposed in [BDS10]. An LDO voltage converter is missing from the schematic overview in Figure 6.1 but can be found in the PCB design (Figure 6.2). This LDO regulator converts a higher input voltage coming from an energy buffer into a lower voltage for a DC-offset in the acoustic signal and powers the low-voltage components.

6.1.2   Energy Assessment

Energy Consumption Measurements

The measured energy consumption and awake time of the chosen hardware components are shown in Table 6.1. Current measurements were performed in two stages. The first stage was a transient stage where the inrush current at initial startup was mostly determined by the large decoupling capacitors at the voltage regulators. As these start-up transients are short in time, a Keysight DSO-X 2002A digital scope [27] with a stable supply voltage of 2.5 V, reference resistor and precision power source was chosen to measure the transient currents of the system at startup. In the second stage, the steady state currents were measured by an Otii Arc precision power analyzer [28] and used for the stable power consumption calculations. The reference voltage was again fixed at 2.5 V. For the active power consumption, a wake-up time (τ_{rx}) of only 1 ms was set. From this table, a total energy consumption of 3.15 µJ can be calculated to perform a single distance measurement when RF wake-up is implemented.

	Microphone	Amplifier	Comparator	Oscillator	Multiplexer	Switches	LDO
$P_{avg,stable}$ [µW]	213	185	2.5	112.5	197.5	2.5	42
Δt_{on} [µS]	140.5	932	452	223	986	842	810
$E_{avg,trans,all}$ [µJ]				1.66			

Table 6.1: Overview of the measured power consumption per component and their wake-up time. Precision current measurements were performed at a fixed reference voltage of 2.5 V.

For complete energy-neutral operation, the current hardware should be extended with an energy harvesting circuit, e.g. E-Peas AEM 40940 [21], and an RF wake-up detector for synchronized wake-ups. These components are grayed out as these are not integrated yet in the current hardware. According to the practical performance assessment performed in Section 5.2.2, full energy-neutrality can be achieved. The energy buffer of 35.1 µJ of the 39.7 µF capacitor is large enough to perform 10 ranging measurements within the 3.1 V to 2.8 V voltage drop. SWIPT in combination with backscattering is possible and has been shown before in [TXC21]. However in this setup, synchronization would interrupt the continuous signal source. The extra hardware needed for to synchronize the mobile nodes to this interruption is an envelop detector that detects the RF wake-up signal and switches between energy harvesting and acoustic backscattering [Li+21c].

Without reference wake-up and in always active mode, the total power consumption of the mobile node is 755 μW. This configuration could last for 894.04 hours or 37.25 days on a lithium CR2032 [29] coin cell battery with nominal voltage of 3 V and a 225 mAh capacity. Without energy harvesting but with the RF wake-up enabled, the lifetime of such node could be extended to 213 646.13 hours, or 8901.92 days or 24.38 years. This does not takes the power consumption of the wake-up circuit and self discharge of the battery into account.

6.2 Hybrid RF-Acoustic Ranging Assessment

To analyze the acoustic zero-crossing digitization approach from Section 4.6 combined with the backscatter communication from Section 5.1 for realistic positioning scenarios, experiments in a true to life test environment were performed. In this section, the test environment and hardware used in the bistatic measurement setup are described. Consequently, three types of measurements were conducted. In the first two, the interdistances between the microphone-speaker pair and the transmitting and backscatter antenna are increased. In the latter, the angle between the transmitting and backscatter antenna is changed. This work limits itself to the ranging capabilities when both acoustic and RF LoS are assured.

6.2.1 Experimental Environment and Measurement Setup

The experiments are again performed in the multi-functional Techtile infrastructure with the hybrid RF-acoustic setup depicted in Figure 6.3. The acoustic characteristics of this room are defined by the RT60 value and linked critical distance. With an RT60 value of 0.41 seconds above 8 kHz for a volume of 77 m³, this room has a critical distance of only 0.75 m [Del+22]. At this distance, the direct and reverberated sound signals can exhibit equal SPL, making this an acoustically harsh environment to conduct measurements in. Additionally, spatiotemporal SPL measurements with a 60 Hz up to 80 kHz frequency and a 10 second time window show different sources contributing to the ambient noise. In the audible domain peaks over 60 dB were detected close to a server and networking rack, whilst a 40.9 dB peak was measured in the ultrasonic domain, coming from switched power supplies.

Figure 6.4 depicts the top view of the experimental setup in the Techtile environment. The following elements can be distinguished:
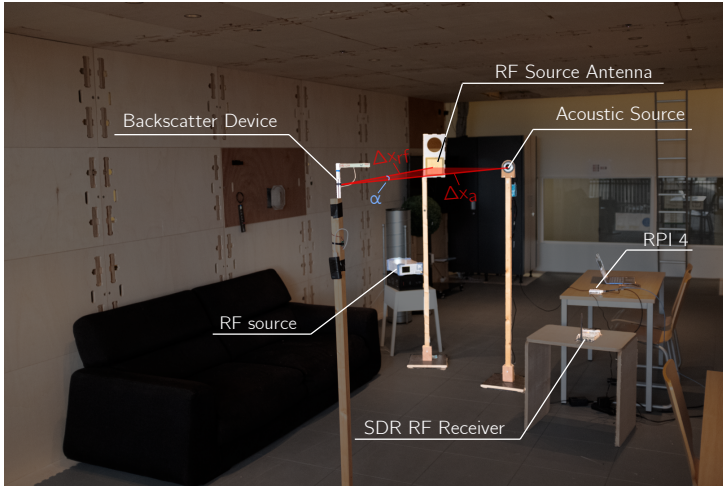
Figure 6.3: Picture of the measurement setup in the wooden Techtile setup.

- RF source: A single frequency carrier sine wave of 868 MHz with an output power of 12 dBm is sent out by R&S SMC100a signal generator [30]. A directional patch antenna with a 6.15 dBi gain is attached to this setup, contributing to a total output power of 18.15 dBm, well below the 27 dBm ERP upper limit imposed by the ETSI regulations for omnidirectional antennas. The antenna is mounted on a pole, at the same height as the antenna of the backscatter device.

- Processing unit for audio transmission (@anchor node): The acoustic signal is generated on a Raspberry Pi 4 [31] running a Debian based operating system. A C library PiGPIO [32] is used for sending out the chirp with a frequency between 40 kHz and 20 kHz by binary switching a GPIO pin for 30 ms. The audio signal is amplified with an off-the-shelf amplifier with a frequency range over 45 kHz. The audio signals are transmitted by a Fostex FT17H [4] ultrasonic tweeter which polar plot is depicted on the left in Figure 3.8. Similar to the RF source, the speaker is mounted on a pole and directed towards the MEMS microphone of the backscatter device.

- Backscatter device (@mobile node): Consists of both RF and audio components and was detailed in Section 6.1.

- Processing unit with SDR (@anchor node): The same Raspberry Pi 4 is used as processing unit running Python based GNU radio [33] in parallel with custom C++ timing and acoustic signal generating code. The RF

backscattered waves are received by a dipole antenna connected to an Ettus B210 Universal Software Radio Peripheral (USRP) Software-Defined Radio (SDR) [34], and converted, filtered and handled by signal processing blocks in GNU radio. These FM demodulated signals are stored on the hard drive for further distance range calculations. Interrupt based, precise timing between the start-up of the acoustic chirp and the RF wake-up time is performed by the software as well, with a maximum measured offset of 10 µs.
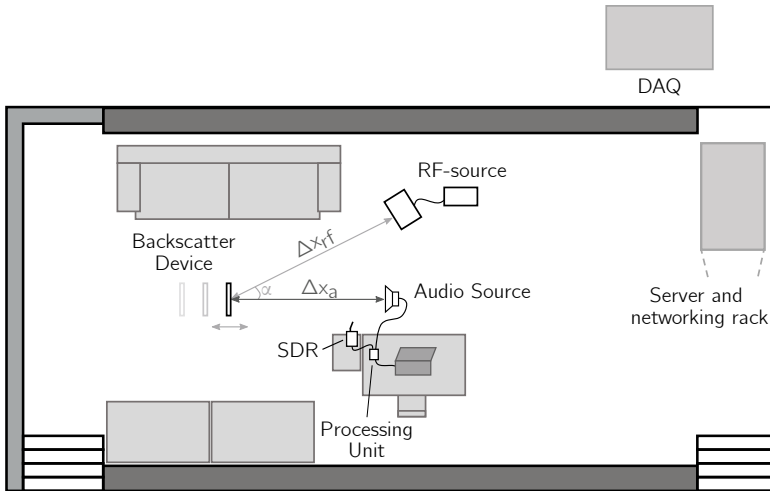
Figure 6.4: Top view of the measurement setup in the Techtile environment.

6.2.2   Conducted Experiments

Three types of experiments were conducted to test the accuracy and precision of the ranging method when backscattering is implemented. The first two assess the distant-dependent performance between the backscatter device and the audio or RF-source. In the third test, the angle of arrival (α) between the RF source and device is varied. All measurements are realized in quasi-ideal circumstances, there is a direct LoS between the source and receiver and both audio and RF-sources and receivers are pointed towards each other. Interfering sources are kept to a minimum, but could not be totally excluded as the room was used under normal conditions with persons walking in and out and other equipment turned on and off at certain moments in time. The current setup lacks the RF wake-up

system. This means that in the reported experiments there was a continuous backscatter communication of the received acoustic signal. To simulate the synchronization and the limited awake time of the mobile node, a 1 ms sampling window was chosen at the end of the acoustic chirp for the distance calculations. To calculate the distances, the maximum method was adopted for the sake of simplicity. Improvements could be obtained when other peak selection methods from Section 4.4 are selected.
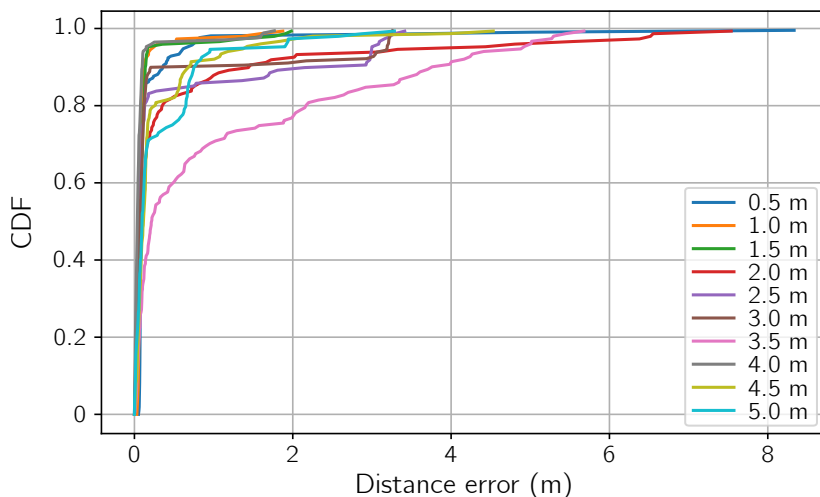
Figure 6.5: General acoustic CDF plot of the measured distance error for different inter speaker and backscatter distances.

Ranging - Audio

As sound propagation is subject to the inverse square law, an experiment of interest is to investigate how well the ranging method performs if the audio distance (Δx_a) is increased by moving the mobile node in a linear, step wise motion. The RF source and accompanying antenna are moved along, keeping the distance ($\Delta x_{rf} < 2$ m) and angle of the incoming RF wave (α) similar in all test cases. This minimizes the potential influence of RF source and receiver spacing. Nevertheless, since the receive antenna of the anchor node is connected through an SDR with the centrally positioned processing unit, there is still some unavoidable influence of the increased RF distance.
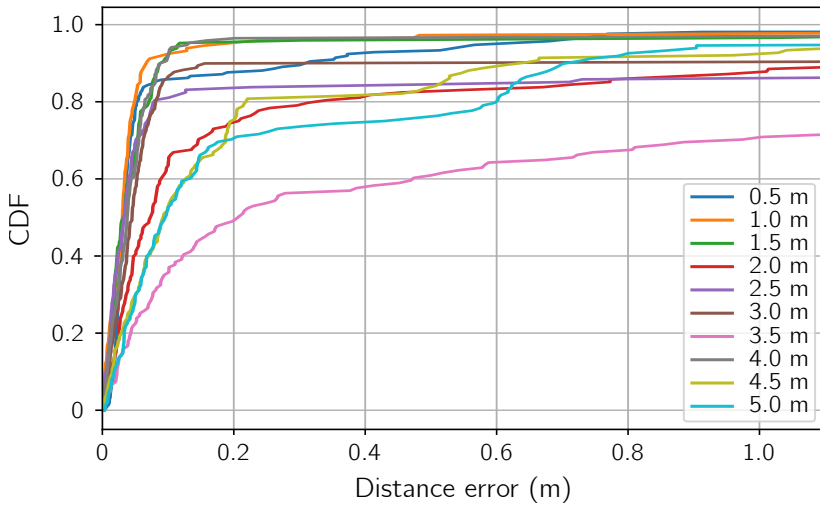
Figure 6.6: Detail of the general acoustic CDF plot for distance errors smaller than 1 m.

Figures 6.5 and 6.6 plot the CDF of the measured error for 10 distances, ranging from 50 to 500 cm. For each distance, at least 150 measurements were performed. The error is the absolute difference of the calculated hybrid ranging measurement and a reference value, measured with a laser-based instrument. The results show an initial steep slope and sudden increase to the outliers. These results are comparable with the ranging results obtained in Section 4.6.2 and validate that on the acoustic level, the ranging performs well. Only at the 350 cm distance in Figure 6.5, a more gradual increasing graph can be observed. This anomaly can be addressed to path loss or reverberation in the acoustic or the RF medium, as better results are obtained at larger distances. The initial rapid incline of this 350 cm graph shows however that the system is capable of calculating the correct distance which rules out errors in the calculations or constructive interference at another fixed frequency. This anomaly can be fixed when redundancy in the form of distributed set-ups is introduced to the system. At the larger distances between the acoustic source and backscatter device, the method behaves as expected and increases with the interdistance (Δx_a). A detail of the acoustic CDF plot is depicted in Figure 6.6. Here, it can be seen that most of the experiments have a P90 value below 20 centimeters. Additionally, all except two have a median error within a 10 cm error, a favorable result for indoor positioning where outlier detection algorithms and Kalman filtering can be used to optimize the results. The 400 cm curves on both plots show that even for larger distances, excellent results

can be obtained. For the largest two distances, a plateau can be noticed on the CDF plot. This plateau can be explained by the fact that, wrongfully, the index of the maximum correlation coefficient is used to estimate the distance, as can be seen in Figure 6.7 where a cross correlation result at $x_a = 5\,\text{m}$ is plotted. The red line on this correlation plot describes the actual distance, whilst the orange lines indicate the peak selected based on the overall maximum. In case of this sample set, adopting an advanced peak selection method as suggested in Section 4.4 would not improve the distance error drastically. From Table 6.2, similar results can be deduced. The difference between the mean and P50 error can be attributed to the high outlier errors. How early these outliers occur is described by the P90 value. The last metric in this table is the mean value of the Side lobe To Main lobe Ratio (STMR). Here the second highest correlation peak is divided by the highest which gives an index in how distinct the highest peak is.

$$mean\,STMR = \sum_{i=0}^{n} \frac{1}{n} \frac{max_2\,(f(t) \star g(t))}{max\,(f(t) \star g(t))} \tag{6.1}$$

With $f(t)$ the received backscatter signal, $g(t)$ the transmitted chirp signal and max_2 the second highest value of the cross correlation between these two. Values closer to 1 indicate that these peaks have similar heights and can often be caused by noise-induced backscatter signals. For ranging calculations with a high STMR, refined peak selection methods could have an impact on the results.

Δx_a [m]	0.501	1.010	1.515	1.998	2.473	3.024	3.499	3.993	4.512	4.992
Mean Error [m]	0.211	0.119	0.125	0.539	0.423	0.335	1.063	0.087	0.294	0.314
P50 Error [m]	0.081	0.080	0.069	0.095	0.058	0.063	0.212	0.036	0.112	0.096
P90 Error [m]	0.351	0.115	0.136	1.268	1.909	0.197	3.704	0.094	0.657	0.746
Mean STMR [m]	0.245	0.249	0.332	0.659	0.474	0.606	0.786	0.470	0.667	0.644

Table 6.2: Metrics overview of the acoustic ranging.

Ranging - RF

A second parameter that is tested is the influence of the distance between the RF-source and the antenna of the backscatter device. In the first set of acoustic measurements, this distance was kept above the far field distance and below 2 m. In the next measurements, the distance Δx_{rf} is gradually increased while keeping the distance between the acoustic transmitter and receiver constant. The influence of the inter-RF distance can be seen in two selected CDF plots, for Δx_a 300 cm and 400 cm in respectively Figures 6.8 and 6.9.
The first plot shows that for smaller values of Δx_{rf}, some interference at a fixed
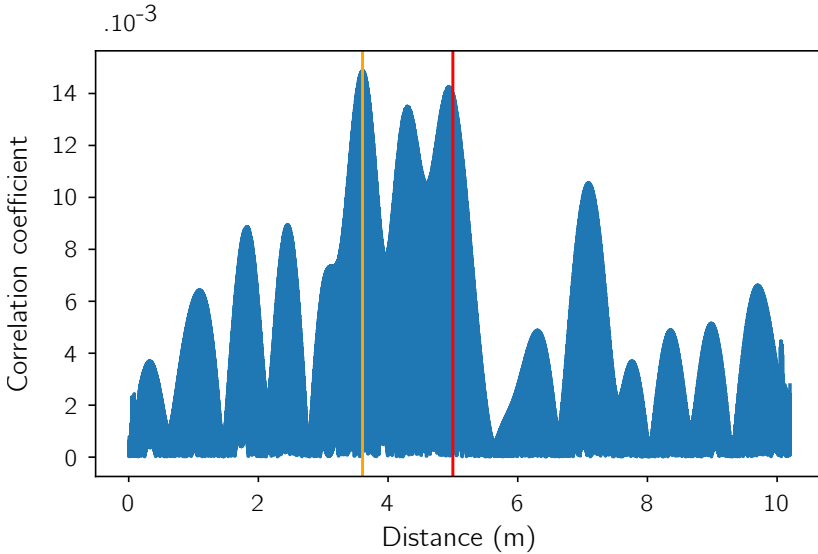
Figure 6.7: Example of a correlation plot between the received RF samples and the original transmitted chirp for an interdistance of $\Delta x_a = 5\,\text{m}$. The red line is the actual distance, the orange line, the selected maximum peak for the used distance estimation.

frequency occurs. This results in a more prominent peak than the correct distance peak after correlation. This interference was only noted at this distance, and its influence diminishes with the increasing distance. This reduction potentially points out an influence of the RF wave's incoming angle (α), as this angle decreases when the RF source moves linearly away from the backscatter device, in parallel with the backscatter-audio source axis. Out of the second CDF figure, it can be seen that for a well performing ranging measurement, there is no influence of the interference nor from the distance, as some larger distances of Δx_a show better results. However, as not all lines follow the same course, the interference effect must come from somewhere else. As aforementioned, a possible candidate is the angle of arrival from the incoming RF wave (α). In this measurement set, this was kept as consistent as possible but not actively measured.

To assess this influence of the angle, a last set of measurements was performed. Here the backscatter device was kept at a constant distance of 250 cm from the acoustic source. The RF-source antenna was moved around this device on a 190 cm radius, with the incoming angle (α) going from 0° to 180° in steps of
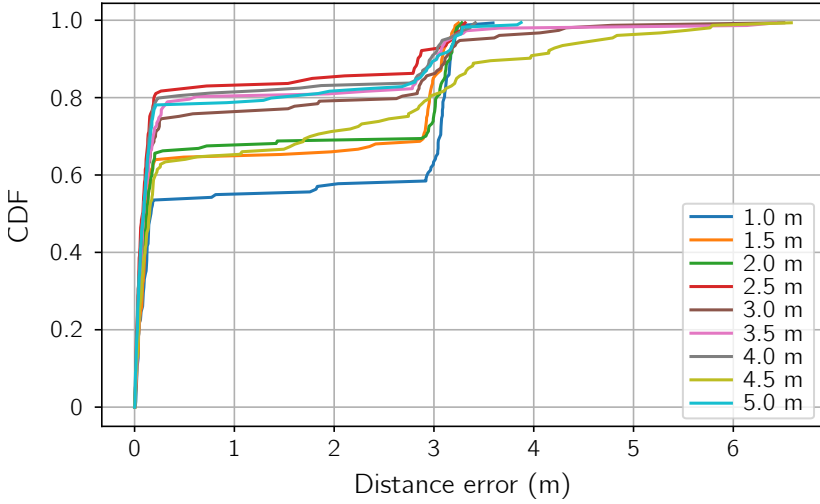
Figure 6.8: CDF plot of the measured distance error for $\Delta x_a = 300\,\mathrm{cm}$ and different Δx_{rf}.
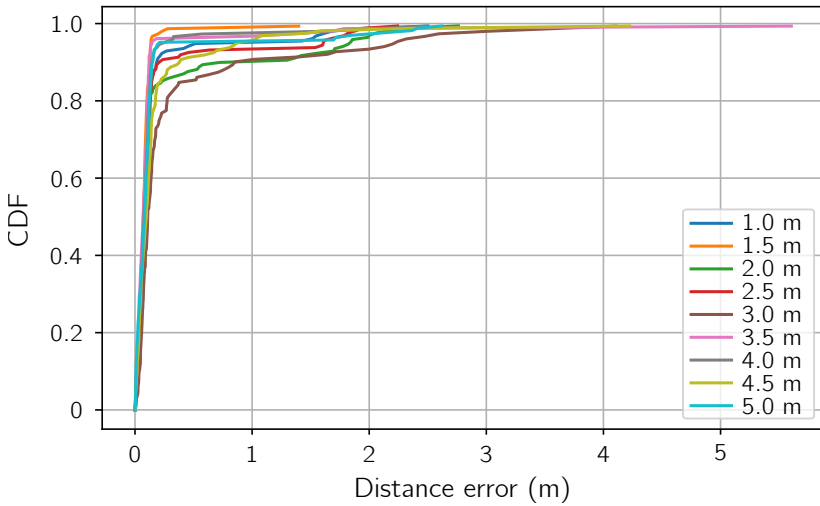
Figure 6.9: Similar to Figure 6.8 fixed acoustic distance is here $\Delta x_a = 400\,\mathrm{cm}$.

27.5°. With this increasing angle, the ranging performance drops drastically, as can be seen in Figure 6.10 and confirms our hypothesis stated before. For angles of 27.5° and above, the curves behave similar as the in Figure 6.8. Again some fixed

frequency interference in the received backscatter signal can be observed, with a larger influence on the cross correlation and ranging measurements, resulting in the previously observed plateaus. Only at 90°, the shape of the plot differs, and inclines more uniformly. The source antenna is here perpendicular to the PCB dipole antenna. From a backscatter perspective, only a small surface of this latter dipole antenna can be seen by the source antenna, leading to poor absorption and reflection capabilities. This can be attributed to the directivity of the half-wave dipole backscatter antenna and is normally embedded in the extended radar range equation from which the incident power density W_i is derived. Half-wave dipoles have a three dimensional toroid shape. In this measurement setup, the radiation peaks when the transmit antenna faces the backscatter dipole ($\alpha = 0°$) and goes towards zero when it is positioned perpendicular to the antenna ($\alpha = 90°$). The cause of the deviations in the previous ranging measurements depicted in Figures 6.5 and 6.8 can thus be explained by the incoming angle, which in most cases is best kept low. With this, it can be concluded that it is better to position the RF side along the acoustic source rather than on the opposite of it. Another solution would be to position the dipole antenna on the perpendicular axis as it has an omnidirectional radiation pattern in this plane.
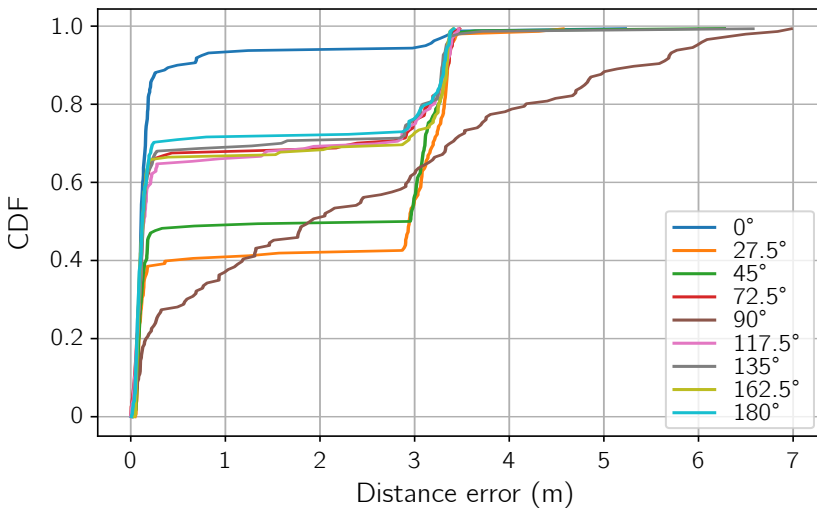
Figure 6.10: CDF plot on the influence of the angle between the RF source and backscatter with $\Delta x_a = 250$ cm and $\Delta x_{rf} = 190$ cm.

6.2.3   System Comparison

Table 6.3 shows an overview of backscatter implementation in different technologies. When our active (always-on) power consumption of 755 μW is compared with that of these state-of-the-art systems, it can be concluded that our system in this always active mode performs the worst of all. However, as the initial ranging concept implies, a synchronized wake-up of the mobile nodes reduced this power consumption below 5 μW. This would put this system to the top of the list regarding the power consumption.

The ranges obtained with the backscatter implementation comes nowhere near the kilometer range that LoRea achieves. These distances are often biased in the literature as the signal sources are kept close to the mobile node, e.g. as close as 20 cm in the PloRa setup [Pen+18]. These do not represent real life scenarios where RF-sources present in anchors are often meters away from the and transmission power is often limited by regulations. A more real to life scenario can be seen in the ambient FM backscatter [Wan+17] where the backscatter range is limited to 1.5 m.

A last parameter that can be compared is the bit rate of the system. In the proposed system, the bit rate depends on the sample rate of the used USRP and the ability of the processing system to handle the incoming data. In the conducted measurements, this sample rate was set to 1 MHz, giving us a 1 Mbps bit rate, which is comparable to the Passive WiFi and BLE backscatter systems. In combination with a high-end processing system, the USRP can sample up to 61.44 MS/s increasing the potential bit rate to 61.44 Mbps.

Signal Source	Reference	Range (m)	Carrier Strength (dBm)	Bit Rate (kbps)	Power Cons. (μW)
WiFi	Passive WiFi [Kel+16]	31	30	1000/110000	14.5/59.2
	HitchHike [Zha+16]	54	30	222	33
LoRa	LoRea [Var+17]	3400	28	2.9	70
	PloRa [Pen+18]	300	21	6.3	220
BLE	BLE Backscatter [ER17]	30	23	1000	623
Ambient FM	FM Backscatter [Wan+17]	1.5	up to 70	3.2	11.1

Table 6.3: Overview of backscatter communication in different technologies.

6.3 From Indoor Ranging to 3D Indoor Positioning

The potential applications of the hybrid ranging system could be greatly expanded when the obtained ranges are used to estimate a position. Previous sections performed a step-by-step evaluation of the most critical elements in this ranging system. In this section, the hybrid-acoustic ranging method is extended into a 3D positioning system and its performance is evaluated in a challenging real-life environment. It puts the algorithmic and architectural co-design to the test for its intended purpose. It is generally known that at least four ranges are necessary for 3D-indoor positioning [Kup05], leading to a setup expansion with a minimum of four anchors. From the anchor's point-of-view, a Time Division Multiple Access (TDMA) scheme is chosen to obtain the corresponding distances, as this prevents acoustic signal collision efficiently at the cost of a lower positioning update rate. Several positioning methods are tested in search of the smallest mean 3D Euclidean distance at all test positions in the acoustically harsh set-up. In this section, RF backscattering is not implemented and only the acoustic side of this hybrid 3D positioning system is considered.
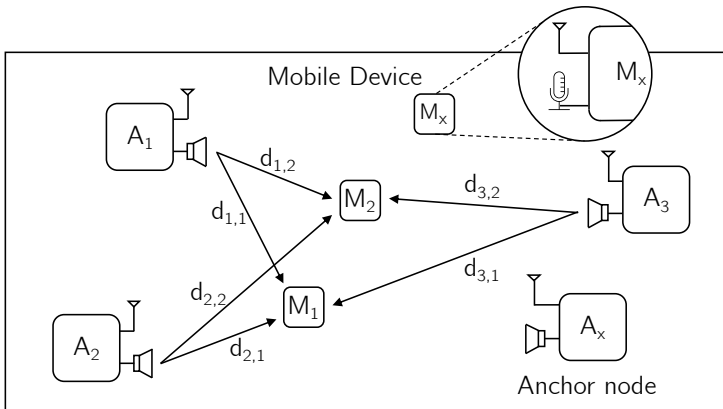
Figure 6.11: Overview of a 2D hybrid RF-acoustic indoor positioning setup. For 3D positioning, an additional anchor node is necessary.

6.3.1 Indoor Positioning and Estimate Optimization Algorithms

In Section 6.2, it is clear that the hybrid ranging has still a median euclidean distance of 10 cm to the ground truth. Using these erroneous ranges in a circular

lateration algorithm results in an unclear intersection. Range-based positioning optimization is intrinsically finding a position estimate with the smallest error term fitting all the distance measurements. This is often achieved by solving a set of nonlinear equations in a least square sense. A fair simulation-based comparison of different iterative and closed-form nonlinear algorithms for 2D positioning can be found in [Sir10]. We have adapted these algorithms for a 3D environment and extended the simulations with experimental data from ranging measurements. This section gives an overview of the implemented algorithms accompanied with a short explanation. For a full derivation and description we refer to the original papers. Notations are the same in all algorithms with:

- s_i is the position vector of anchor i containing its x, y and z coordinates
- N is the number of anchors (4)
- r_i is the ranging measurement to anchor i
- $\hat{p}$ is the position estimate

The pseudocode of the algorithms can be found in Appendix A

Simple Intersection

Classical circular lateration interprets the measured ranges as circles centered around the anchor in 2D. The combination of several of these circular Lines of Positions (LoPs), generates an intersection. The latter is considered to represent the best estimate for the position of the mobile sensor node. However, this geometrical approach is susceptible to noise. As errors are introduced, the circular LoPs do not intersect in a specific point, but create an area with potential estimates. In [Caf00], linear LoPs are created by drawing a straight line through the intersecting points of two ranging circles. The intersection of these newly generated lines indicates the position estimation. The advantage of this method is that it is still possible to generate linear LoPs when, due to errors, two or more circles do not intersect. The Moore-Penrose inverse, least squares estimate can be used to find an algorithmic rather than a geometric solution with a minimum number of linear LoPs of $N - 1$.

Bancroft

Bancroft [Ban85] uses an algebraic, non-iterative technique to solve the GPS equations that is computationally efficient and numerically stable. In contrast to

iterative techniques, higher order terms of the Taylor series expansions are not discarded, resulting in a better performance when anchors are poorly arranged. Although there is a lot of similarity with the Simple Intersection method, the Moore-Penrose inverse is not used for minimizing the difference between the exact position and measurement residual, but as a projection operator in the n-dimensional space of these residuals.

Beck

Instead of a Range-Based Least Squares (R-LS) minimization, a Squared-Range-Based Least Squares (SR-LS) (or least quartic) method can be used to find a position estimate [BSL08]. An exact, optimal solution can be found by using a bisection algorithm to find a single root of a univariate strictly monotonous function. This method shows a better mean squared position error in comparison with the R-LS method.

Chueng

An alternative way to compute the SR-LS estimate is presented in [Che+04]. For a 3-dimensional space, all roots of a seven root equation are calculated by rewriting it in a seventh degree polynomial. In contrast with the original paper, the absolute of the roots are taken instead of eliminating complex roots. The root closest to zero is used to compute the estimate of the globally optimal constrained weighted least squares.

Gauss-Newton

Also known as Weighted Iterative Least Squares (WILS) is a straightforward method using only algebraic operations, in the form of a Jacobian matrix or the derivative of the measurement equation, to find an estimation. The disadvantages of this method are the need for prior information in the form of an initial positioning guess and the fact that it is computationally harder. Sirola [Sir10] suggests the simple intersection method as a starting point for the position estimation. When used in time series, the algorithm extends naturally to a Kalman filter.

6.3.2   Spatial Dispersed Ranging Measurements

All experiments are performed in the Techtile test environment. Four acoustic anchors are spread across the test bed, with three of them close to the outer edges of the room, maximizing the spatial resolution on all three axes. Each anchor consists of an ultrasonic speaker (Kemo L010) directed to the center of the room and an off-the-shelf amplifier with a frequency range over 45 kHz. These four anchors are connected to a multi-channel DAC (NI-USB-6212 DAQ), where the chirp signals are generated and TDMA anchor selection is performed. The sensor node consists of a single MEMS microphone with distinctive amplifier and band filter combined with a sub-GHz wireless MCU launchpad (CC1310). A central computer connected to another launchpad handles the received binary sampled audio chirps and calculates the measured distances.

Measurements are performed on 150 fixed positions. Three layers with an uniform planar array of 50 points on fixed heights are created. On each position at least 50 distances are measured to each of the four anchors, resulting in a total of over 30 000 ranging measurements. These time expanded ranging measurement are necessary to average out errors introduced by the dynamic Techtile environment.

To understand the potential positioning inaccuracies and single out advanced positioning algorithms, the ranging measurements are explored, this time for spatial dispersed mobile nodes. Four heat maps, displaying the error range's magnitude in a 2D projection of the room, can be found in Figure 6.12. Each heat map, one for each anchor, shows the Mean Absolute Error (MAE) of 50 measurement for 50 positions on a fixed height (1.4 m). The speaker position and orientation are illustrated by a symbol. A couple of observations can be made. Firstly, as could be expected from the acoustic ranging assessment in Section 4.5.1 the error increases with the distance. This can be attributed to the acoustic signal attenuation and can be easily described by the inverse square law and additional air absorption attenuation. In this system, lower signal-to-noise ratios are detrimental for the zero-crossing based, binary template cross correlation. Secondly, larger errors can be found closer to the edge of the room, where effects from reflections and scattering are more prone. And thirdly, in all four heat maps, a directional speaker pattern can be noticed. This is caused by the directionality of the Kemo L010 speaker, with a half power beam width of 30° derived from the right polar plot in Figure 3.8.

To evaluate the influence of the acoustic scattering and reflections, extra
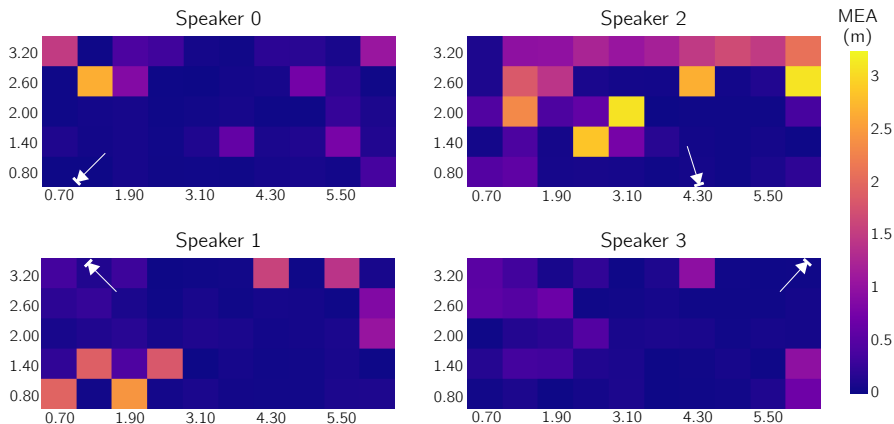
Figure 6.12: Mean absolute distance error heat maps for ranging to different anchors at a height of 1.407 m.

measurements were performed. Table 6.4 gives more insight in the accuracy and precision of the distance measurements between a single anchor and a sensor node close to a wall. As shown in Section 4.5.1, acoustic reverberation has a large influence on the ranging accuracy. For this reason, two sets of 140 ranging measurements were conducted on the same position, one with and another without acoustic absorbers added on the nearest wall. The mean (μ), difference between minimum and maximum value (range), median (P50), P95 and standard deviation (σ) values are all spectacularly improved when absorbers are added, confirming the reverberation hypothesis by canceling out reflections and scattering and decreasing the reverberation locally. In this case, the low median and mean distance error values result in a high accuracy whilst the standard deviation of only 5.2 cm and range of 22.8 cm reveal a small error variation with low outliers and thus a high precision.

	μ (m)	Range (m)	P50 (m)	P95 (m)	σ (m)
Absorber	0.083	0.228	0.087	0.179	0.052
No absorber	0.958	1.965	0.971	1.938	0.894

Table 6.4: Influence of acoustic absorbers on the absolute distance error for a sensor node close to a wall.

6.3.3   Empirical 3D Positioning Comparison

The obtained ranging results are promising, achieving centimeter-accuracy given favorable circumstances. Yet it will be interesting to see how well the 3D positioning algorithms perform for mobile sensor nodes close to walls or out of the main acoustic lobes. A comparative Cumulative Density Function (CDF) of the mean Euclidean error distance of 50 measurements in each of the 150 positions for the different methods is created (Figure 6.13). At first glance, it is clear that implementing more advanced estimation algorithms greatly improves the position estimation. When taking a closer look, the plots can be divided into three groups. The first one is the Chueng method, showing the steepest incline and outperforming all the other algorithms. With half the measurements below an Euclidean distance error of 0.73 m and 95% just above the 1.54 m, it demonstrates to be accurate even with erroneous ranging measurements. The three methods belonging to the second group are Bancroft, Beck and Gauss-Newton. They have a similar curvature and a P90 value below 3.5 m, with the Gauss Newton method having a single outlier at 69.8 m. The last curve consists of the basic intersection method, with a low accuracy and high susceptibility to noise (P90 of 10.34 m).
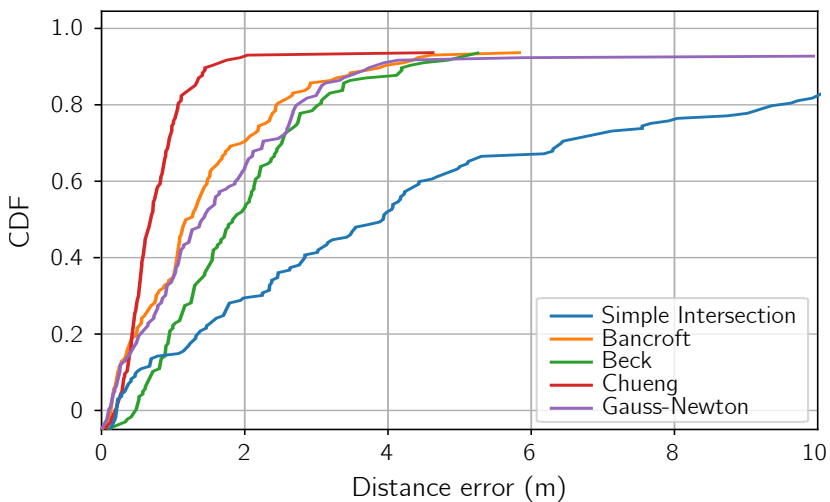
Figure 6.13: Cumulative density functions of the mean 3D Euclidean distance error over 50 measurements at the 150 different positions.

To investigate the influence of the ranging error on the precision, the position estimates of the two best performing techniques are plotted in Figure 6.14 and 6.15. Two scenarios are depicted, with the yellow dot representing the actual

position. The sensor node position in the first scenario is closer to the wall, with larger average distance measurement errors to two anchors: 0.923 m and 0.626 m to respectively Anchor 1 in the upper left corner, and Anchor 4, centrally at the far right. The second sensor node position is more centered, and has a maximum mean ranging error below 5 cm.

- The Chueng algorithm behaves similarly in both scenarios: forming a dense cloud in the neighborhood of the actual position. The mean Euclidean distance error is 0.490 m for the first scenario and 0.554 m for the second. This indicates a lower accuracy, while at the same time having a high precision for both scenarios, hence the dense cloud.

- The Bancroft forms a more scattered arrangement, performing worse on both accuracy and precision. Even with precise distance measurements, the estimates spread out in the z-direction, where the anchor range resolution is lowest.
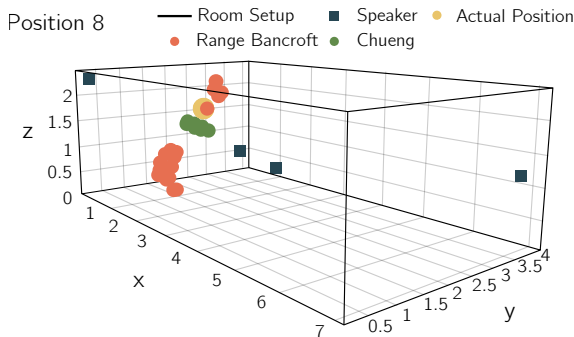
Figure 6.14: 3D position estimations of the Chueng and Bancroft method on position close to the wall.

Towards Centimeter Accurate 3D Positioning

In the most favorable conditions, the Euclidean distance is 0.0102 m, indicating that the intended accuracy *can* be achieved. Undeniable, there is still a long road ahead go to reach this centimeter accuracy in non-ideal conditions, and the gap to be bridged is at least an order of magnitude higher. For more consistent
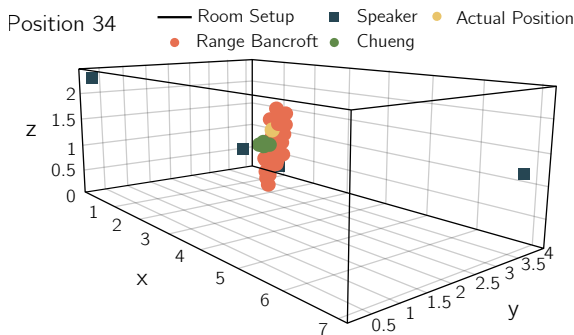
Figure 6.15: 3D position estimations of the Chueng and Bancroft method on position more in the center of the room.

exact location estimates of energy-constraint nodes, the following upgrades are proposed:

- **Hardware and system based improvements.** To prevent signal attenuation due to speaker directivity, the system could be extended on a hardware level by adding extra speakers to the anchors. As stated in Section 3.2.3, care should be taken in the design, as constructive interference and spatial aliasing occur at higher frequencies when multiple speakers are used, resulting in non-uniform and, again, directional sound pressure fields [Que+14]. Anchor placement should be optimized as well, potentially increasing the number of anchors. Even with precise ranging measurements, positioning errors are largest in the z-dimension of the room. The resolution on this axis can be increased by placing an anchor in the ceiling or embed it in the floor. When such anchors are added to the system, adaptive anchor selection algorithms could be implemented to minimize the amount of active anchors and increase the position reliability.

- **Improve, combine or implement new positioning algorithms.** The chosen optimization algorithms are considered as safe and credible. They are an excellent way to test the feasibility of the system at the cost of accuracy and precision. Advanced position estimation techniques could be combined. Algorithms like non-linear least square estimation and Gauss-Newton require an initial positioning guess. In this paper, the poorly performing simple intersection method is used as a starting point as suggested by [Sir10].

Future research could explore the Chueng algorithm as a starting point or investigate the potential accuracy gain of time-series Kalman filters.

- **Tackle the position update rate and mobile node energy consumption.** Current TDMA implementation gives a positioning update every 4 seconds. Increasing the ranging frequency solves the positioning update rate as long as multi-user interference is prevented. To lower the energy consumption, a better solution would be to simultaneously transmit the acoustic signals. In [YWC16; Ber+20] a Chirp Spread Spectrum (CSS) transmission scheme is introduced, enabling multi-user communication. A more in-depth study should validate the bit based sampling for this latter method.

6.4 Conclusion

In this chapter, a hardware implementation of the mobile node is proposed that incorporates the zero-crossed acoustic chirp reception proposed in Section 4.6 together with the RF backscattering explained in Section 5.1. Using the digitized acoustic signal to switch the antenna load between a local oscillator frequency or a DC signal generates two-sided frequency modulation. This hardware solution addresses two of the three implications for energy neutral devices proposed in Section 3.3: the acoustic reception and the mobile node's allowed laziness. This latter is acknowledged on the mobile node by transmitting the digitized acoustic signals directly back to the anchor nodes, where the distance calculations are performed. The third implication, keeping the active time of the mobile node low is not tackled, as synchronized wake-ups and energy harvesting are not yet implemented. However, an evaluation of the mobile node's hardware design shows that with a total energy consumption of $3.15\,\mu J$ per ranging measurement, 10 distances can be measured with the energy stored in the capacitor buffer from Section 5.2.1.

The ranging measurements performed with this hardware in a real life environment investigate the influence of the RF backscattering on the accuracy and precision. In ideal conditions, where the source antenna is placed perpendicular to the backscatter antenna and the range between these two antennas is kept below $2\,m$, a median Euclidean distance around $10\,cm$ can be obtained for inter-acoustic distances up to $5\,m$. When compared to the pure acoustic zero-crossed measurements, the obtained backscattered euclidean distances are higher, showing the negative impact of RF backscattering on the peak prominence methods. The influence source-to-backscatter antenna distance can be considered as minimal.

The final measurement campaigns conducted with the dedicated hardware show the influence of the angle between the transmit and backscatter antennas on the accuracy. This latter drops significantly and can be described to the directionality dependency of the radar range equation.

To conclude this PhD an evaluation of the 3D positioning capabilities of this hybrid RF-acoustic ranging system is conducted. Five safe and credible algorithms are used to estimate the position based on the zero-crossed ranging results. A cm-accurate 3D position is only obtained in a couple of estimations and with the majority of the ranging errors above one meter of distance error, it is clear to state that there is still a long road ahead to reach this centimeter accuracy in non-ideal conditions.

Chapter 7

Conclusions and Outlook

At the end of each chapter, a specific conclusion was provided. In this last chapter, a more general conclusion and look on potential future research and applications is given.

When reconsidering the most prominent and overall objective of this work, it can be concluded that with the proposed hybrid RF-acoustic system, a disruptive and innovative approach for indoor ranging is designed and researched. The full potential of this system is obtained thanks to the symbiotic algorithmic and architectural co-design. An in-depth evaluation of the key elements confirms the application in real-life scenarios and unveils the research potential for future improvements.

7.1 Conclusions

The specific conclusions made here are based on the research questions raised in the first chapter of this book. These answers also include whether the recommended system requirements are satisfied or not.

What technology can be used to design an energy-neutral, low cost and accurate ranging system? Choosing a technology for the enforced evaluation parameters can be seen as the plate spinning circus manipulation exercise. At a certain moment, you have to sacrifice a plate to keep the rest spinning. Analogously, it is impossible for a single technology to tick every evaluation parameter's box and compromises should be made. In this work, hybrid-RF acoustic is chosen, as the

slower propagating acoustic waves allow for accurate ToF-based ranging with low-complexity hardware. Regarding the energy-neutrality of the ranging measurements, it emerges that not only the signal's physical quantity and technology have impact on these parameters. Disruptive methods should be developed on a system level with clear requirements based on real-life hardware and environmental constraints. With a cost just shy of €15 for a single prototype, the cost requirement is met.

Choosing hybrid RF-acoustic does not mean that parallel research could present similar or even better results on certain evaluation parameters with a different technology and approach. With the vast amount of academic and commercial research done on this subject, chances are high that this will happen in the near future.

How do the environmental factors impact the system performance and what improvements can be carried out to counter these negative effects? Hybrid indoor ranging systems are both a curse and a blessing. They can combine the advantages of each physical signal, gaining the best of both worlds, but at the same time suffer from double the impact of the channel and hardware effects. An extensive step by step evaluation was performed to investigate both of these effects on the ranging measurements. Both simulations and measurements show that the major influences on the acoustic part of the ranging system come from room reverberation, signal attenuation, the limited bandwith in the ultrasonic domain of the commercially available MEMS microphones and the directionality of the tweeters. Peak selection methods introduced in this work improve these results, countering the room reverberation introducing unwanted correlation maxima when pulse compression is applied.
For RF-backscattering, the largest impact on the ranging accuracy comes from the antenna directivity, with additional, lower influence of the inter-antenna distance.

How can a ranging accuracy below 10 cm be achieved with energy-constrained measurements? And how well can a mobile node be located when the ranging system is expanded to a 3D environment? Pulse compression is applied to the received, zero-crossed and backscattered acoustic chirp signal to obtain range estimations. Whilst the pure acoustic, zero-crossed chirp frequency demodulation shows a mean average error below 5 cm for ranges up to 7 m, a median euclidean distance of just above 10 cm is obtained for distances below 4.5 m. This means that in the current prototype, the system design requirements regarding the range and ranging accuracy are not met yet. However, the obtained results are promising and show that with the architectural and algorithmic co-design, it is possible for hybrid-ranging to obtain the requested centimeter accuracy with an energy-neutral mobile node. A fair and in-depth comparison of this system with the current state-of-the-art low-power hybrid RF-acoustic systems is hard, as the tests are

performed outside ideal, lab based environments and ranging measurements are done for more realistic indoor distances.

The effects of the hardware and environmental influences are even more present when 3D positioning is performed. The safe and credible positioning algorithms do not achieve the centimeter accurate ranging measurements. With a median Euclidean distance of 75 cm, a first step towards this accurate indoor positioning is made and with the obtained data, new and more unconventional 3D positioning algorithms can be easily implemented on real-life measurements.

How can energy-neutrality be achieved at the mobile node? The strength of the proposed ranging system lies in the symbiotic co-design of the algorithms and architecture. For example, the awake time has a major impact on the energy neutrality. For this awake time to be as low as possible, the wake-up of the hardware needs to be short and a ranging algorithm needs to be chosen that can receive sufficient data within the short receive period. Other cooperative design examples can be found in the combination of backscatter communication and energy harvesting on the same RF signal, the ultrasonic acoustic reception and zero-crossing digitization, acoustic signal modeling and efficient processing, and acoustic signal to FM-based backscattering and processing offloading.

In the proposed ranging method, five major algorithmic-architectural ideas contribute to the obtained energy-neutrality at the mobile node. The first originates from the system design strategy and implies acoustic reception, awake time limitations and processing transfer to the anchor nodes. The second implementation is the acoustic data reduction by means of zero-crossed digitization. This discards energy-consuming ADCs. The next contribution comes from RF-backscattering and replaces common radio-chips with RF-switches and a local oscillator. The necessary energy budget needed to perform measurements is provided by RF energy harvesting, forms the fourth contribution. Measurements performed in this work show that the harvested energy is sufficient for quasi-static or slow moving devices. The final contribution comes in the form of the hardware design. Well-chosen COTS components with low active power and wake-up times make the implementation of the acoustic receive-and-backscatter solution possible.

With an always-active power consumption below 1 mW, this solution consumes far more energy than any other (long-range) backscatter solutions but not compared to state-of-the-art positioning systems with similar range and accuracy. This

always-active mode renounces the whole RF wake up concepts envisioned in this work and with the implementation of RF-synchronization, the power consumption drops significantly below 5 μW for a 1 Hz positioning update rate. This fulfills the design requirement drafted in Section 1.2.2 and ranging measurements with this update rate can be performed for over 15 years on a single CR2032 coin cell battery.

7.2 Outlook

This work confirms the promising potential of hybrid RF-acoustic ranging with experimental assessments, showing that this technology is mature enough to be exploited for 3D positioning. With the accuracy obtained in the ranging system, a couple of applications can currently be addressed such as proof of authenticity when being physically present to gain access to secure environments and alarming when coming too close to certain hazardous areas. The application potential is greatly increased in societal, personal and business areas when the ranging system is extended to 2D and 3D positioning. The current implementation is only assessed for static devices with applications in tracking with low update rates and location based services. For indoor navigation of faster moving devices, further research needs to be conducted as Doppler effects can have a major influence on the accuracy.

Hardware integration: The road ahead addresses further integration on the hardware level, including synchronization and energy harvesting to reduce the mobile nodes' energy consumption. A possible approach for this first hardware integration could be in the form of an RF envelope detector to serve as a wake-up signal. For energy harvesting, SWIPT on the same frequency is however not possible but multiband solutions could solve this issue.

Multiple Access: The current system is not assessed when multiple mobile nodes are present in the same room. In the acoustic domain, the slower TDMA was implemented for 3D positioning, needing at least 4 separate measurements to obtain a single position. FDMA is possible in the frequency domain, but requires specific selected impedances on the mobile nodes and a large bandwidth to accommodate a large amount of nodes. In both the acoustic and RF domain, future research is necessary to allow simultaneous acoustic transmission of several anchors to improve positioning rates and for single frequency band backscatter modulation on the mobile device.

Methods to improve the precision and accuracy: Solutions to increase precision and reliability in challenging reflective indoor environments are to be researched.

For example Simultaneous Localization and Mapping techniques (SLAM) could help to combat bad outliers and give insight in room shapes and dimensions. Another example can be found in data driven machine learning methods where the previous location can be used as an input for current position estimations.

Hardware design: As described in the literature, implementing the zero-crossed acoustic backscattering on a single integrated circuit has the potential to further increase the energy efficiency drastically.

Positioning of mobile devices Research potential lies in the tracking of objects where energy consumption is not crucial, e.g. cobots and autonomous vehicles . Here the acoustic receive window can be extended, resulting in improved pulse compression and the processing units available on these commodities enable self-positioning.

REINDEER - Smart Connectivity beyond 5G: Within the European Horizon 2020 project REINDEER, a new smart connect-compute platform is developed to interact with an extremely high number of embedded devices, where radio, computing and storage devices are distributed. One of the objectives within this project is to develop protocols and algorithms to accomplish interaction with energy-neutral devices. The practical knowledge gathered in this PhD can be adopted for the uplink communication in this system and support novel applications envisioned in 6G networks.

Appendix A

3D Indoor Positioning Algorithms

Algorithm 1 Simple Intersection

$$A = \begin{bmatrix} 2s_1^T \\ \vdots \\ 2s_4^T \end{bmatrix}, \quad b = \begin{bmatrix} \|s_1\|^2 - r_1^2 \\ \vdots \\ \|s_4\|^2 - r_4^2 \end{bmatrix}$$

$$D = \begin{bmatrix} -1 & I_{N-1} \end{bmatrix}$$

with I_{N-1} the identity matrix gives:

$$\hat{p} = \left(A^T D^T D A \right)^{-1} A^T D^T D b$$

Algorithm 2 Bancroft

$$A = \begin{bmatrix} 2s_1^T \\ \vdots \\ 2s_4^T \end{bmatrix}, \quad b = \begin{bmatrix} \|s_1\|^2 - r_1^2 \\ \vdots \\ \|s_4\|^2 - r_4^2 \end{bmatrix}$$

$$v = \left(A^T A \right)^{-1} A^T \mathbf{1}$$

$$w = \left(A^T A \right)^{-1} A^T b$$

find the roots of:

$$\|v\|^2 t^2 + \left(2v^T w - 1 \right) t + \|w\|^2 = 0,$$

and from the two position candidates:

$$\hat{p}_i = v t_i + w, \quad i = 1, 2$$

pick the one with the smallest residual as the final estimate.

Algorithm 3 Beck

$$A = \begin{bmatrix} 2s_1^T & -1 \\ \vdots & \\ 2s_4^T & -1 \end{bmatrix}, \quad b = \begin{bmatrix} \|s_1\|^2 - r_1^2 \\ \vdots \\ \|s_4\|^2 - r_4^2 \end{bmatrix}$$

$$P = \begin{bmatrix} 1 & 0 & 0 & 0 \\ 0 & 1 & 0 & 0 \\ 0 & 0 & 1 & 0 \\ 0 & 0 & 0 & 0 \end{bmatrix}, \quad q = \begin{bmatrix} 0 \\ 0 \\ 0 \\ -\frac{1}{2} \end{bmatrix}$$

Use a bisection method to obtain a solution for

$$\phi(\lambda) = \hat{z}(\lambda)^T P \hat{z}(\lambda) + 2q^T \hat{z}(\lambda)$$

in the declining interval $[-1/\lambda_1, \infty]$, where

$$\lambda_1 = \max \left(\text{eig} \left(A^T A \right)^{-\frac{1}{2}} P \left(A^T A \right)^{-\frac{1}{2}} \right)$$

and

$$\hat{z}(\lambda) = \left(A^T A + \lambda P \right)^{-1} \left(A^T b - \lambda q \right)$$

The estimate $\hat{p}$ is given by the first 3 elements of $\hat{z}$.

Algorithm 4 Chueng

$$A = \begin{bmatrix} s_1^T & -0.5 \\ \vdots & \\ s_4^T & -0.5 \end{bmatrix}, \quad b = 2\tfrac{1}{2} \begin{bmatrix} \|s_1\|^2 - r_1^2 \\ \vdots \\ \|s_4\|^2 - r_4^2 \end{bmatrix}$$

$$B = \begin{bmatrix} r_1 & & \\ & \ddots & \\ & & r_4 \end{bmatrix}, \quad \Psi = B(B^T I_N)$$

$$P = \begin{bmatrix} 1 & 0 & 0 & 0 \\ 0 & 1 & 0 & 0 \\ 0 & 0 & 1 & 0 \\ 0 & 0 & 0 & 0 \end{bmatrix}, \quad q = \begin{bmatrix} 0 \\ 0 \\ 0 \\ -1 \end{bmatrix}$$

Compute U and Λ from the eigenvalue decomposition

$$\left(A^T \Psi^{-1} A\right)^{-1} P = U \Lambda U^{-1}$$

$$= U \begin{bmatrix} \gamma_1 & & & \\ & \gamma_2 & & \\ & & \gamma_3 & \\ & & & 0 \end{bmatrix} U^{-1}$$

with γ_i the eigenvalues of the matrix $\left(A^T \Psi^{-1} A\right)^{-1} P$, and

$$c = 2 U^T q$$

$$g = 2 U^{-1} \left(A^T \Psi^{-1} A\right)^{-1} q$$

$$e = \left(\Psi^{-1} A U\right)^T b$$

$$f = U^{-1} \left(A^T \Psi^{-1} A\right)^{-1} A^T \Psi^{-1} b,$$

Find the absolute of the complex root λ^* closest to zero of the following seven-root equation

$$0 = c_4 f_4 - \frac{\lambda}{2} c_4 g_4 + \sum_{i=1}^{3} \frac{c_i f_i}{1 + \lambda \gamma_i} - \frac{\lambda}{2} \sum_{i=1}^{3} \frac{c_i g_i}{1 + \lambda \gamma_i}$$

$$+ \sum_{i=1}^{3} \frac{e_i f_i \gamma_i}{(1 + \lambda \gamma_i)^2} - \frac{\lambda}{2} \sum_{i=1}^{3} \frac{(e_i g_i + c_i f_i) \gamma_i}{(1 + \lambda \gamma_i)^2}$$

$$+ \frac{\lambda^2}{4} \sum_{i=1}^{3} \frac{c_i g_i \gamma_i}{(1 + \lambda \gamma_i)^2}.$$

and compute the estimate of the constrained weighted least squares

$$\hat{z} = \left(A^T \Psi^{-1} A + \lambda^* P\right)^{-1} \left(A^T \Psi^{-1} b - \frac{\lambda^*}{2} q\right)$$

with the first three elements of $\hat{z}$ as the position estimate $\hat{p}$.

Algorithm 5 Gauss-Newton

1: Calculate an initial guess p_0, a stopping tolerance δ and an iteration upper limit k_{max}. As a starting point, the simple intersection method is chosen. Set $k = 0$.

2: Compute the Jacobian Matrix:

$$J_k(p) = \begin{bmatrix} \frac{s_1-p}{\|s_1-p\|}^T \\ \vdots \\ \frac{s_4-p}{\|s_4-p\|}^T \end{bmatrix}$$

3: Set $p_{k+1} = p_k + \Delta p_k$, where Δp_k the least square solution is of:

$$\left(\Sigma^{-\frac{1}{2}} \left(h\left(p_k\right) - r \right) \right) \Delta p_k = - \left(\Sigma^{-\frac{1}{2}} J_k \right)$$

4: If stopping condition $\|\Delta p_k\| < \delta$ is not satisfied and $k \leq k_{\max}$, increment k and repeat from Step 2.

Datasheets, Whitepapers and Reference Manuals

[1]   *The route to a trillion devices*. Tech. rep. ARM, 2017, p. 14. URL: `https://community.arm.com/cfs-file/__key/telligent-evolution-components-attachments/01-1996-00-00-00-01-30-09/Arm-_2D00_-The-route-to-a-trillion-devices-_2D00_-June-2017.pdf`.

[2]   *Galileo High Accuracy Services*. Tech. rep. European Global Navigation Satellite Systems Agency, 2020, p. 14. URL: `https://www.gsc-europa.eu/sites/default/files/sites/all/files/Galileo_HAS_Info_Note.pdf`.

[3]   *Global Indoor Positioning and Indoor Navigation (IPIN) Market Outlook, 2024*. Tech. rep. Goldstein Market Intelligence, 2019, p. 200. URL: `https://www.goldsteinresearch.com/report/global-indoor-positioning-and-indoor-navigation-ipin-market-outlook-2024-global-opportunity-and-demand-analysis-market-forecast-2016-2024`.

[4]   *FT17H Horn Tweeter*. Tech. rep. Fostex, 2013, p. 1. URL: `https://www.fostexinternational.com/docs/speaker_components/pdf/ft17hrev2.pdf`.

[5]   *VM1000 Low Noise Bottom Port Analog Single-Ended Piezoelectric MEMS Microphone*. Tech. rep. Vesper, 2019, p. 9. URL: `https://vespermems.com/wp-content/uploads/2019/03/VM1000_Datasheet-2.pdf`.

[6]   *MM20 MEMS microphone*. Tech. rep. Knowles, 2018, p. 10. URL: `https://www.knowles.com/docs/default-source/default-document-library/mm20-33366-b116.pdf`.

[7]   *IMP23ABSU, High-performance MEMS microphone with extended frequency response up to 80 kHz for ultrasound applications*. Tech. rep. ST microelectronics, 2020, p. 15. URL: `https://www.st.com/resource/en/datasheet/imp23absu.pdf`.

[8]   *L010- Piezo Loudspeaker*. Tech. rep. Kemo Electronic, 2016, p. 1. URL: `http://www.kemo-electronic.de/product_info_pdf.php?products_id=386`.

[9]   *Microphone N8AC03*. Tech. rep. Sonion, 2014, p. 1. URL: `discontinued`.

[10]   *M30 - High Definition Measurement Microphone*. Tech. rep. Earthworks Audio, 2018, p. 1. URL: `https://earthworksaudio.com/wp-content/uploads/2018/07/M30-Data-Sheet-2018.pdf`.

[11]   *MEMS Speaker ADAP UT-P2023*. Tech. rep. USound, 2021, p. 16. URL: `https://www.usound.com/download/adap-ut-p2023-datasheet/?wpdmdl=3742`.

[12] Akustik. *Absorption Coefficients*. 2014. URL: `http://www.acoustic.ua/st/web_absorption_data_eng.pdf`.

[13] *SPU1410LR5H-QB Zero-Height SiSonic Microphone With Extended Low Frequency Performance*. Tech. rep. Knowles, 2013, p. 11. URL: `https://eu.mouser.com/datasheet/2/218/pu1410lr5h-qb-1522384.pdf`.

[14] *TLV34xx Low-Voltage Rail-to-Rail Output CMOS Operational Amplifiers With Shutdown*. Tech. rep. Texas Instruments, 2016, p. 40. URL: `https://www.ti.com/lit/ds/symlink/tlv342a.pdf`.

[15] *USB-621x User Manual*. Tech. rep. National Instruments, 2009, p. 204. URL: `https://www.ni.com/docs/en-US/bundle/usb-621x-features/resource/371931f.pdf`.

[16] *TDA7492- 50 W + 50 W dual BTL class-D amplifier*. Tech. rep. ST Microelectronics, 2015, p. 32. URL: `https://www.st.com/resource/en/datasheet/tda7492.pdf`.

[17] *CC1310 SimpleLink Ultra-Low-Power Sub-1 GHz Wireless MCU*. Tech. rep. Texas Instruments, 2018, p. 70. URL: `https://www.ti.com/lit/ds/swrs181d/swrs181d.pdf`.

[18] *Bosch GLM 30 Professional*. Tech. rep. Bosch, 2020, p. 115. URL: `https://www.bosch-pt.com.cn/binary/ocsmedia/optimized/full/o331567v21_160992A5E0_202001.pdf`.

[19] K. Teltsch. "Lodge Tells U.N. Symbol Was Gift From Russians; Russians Tapped U.S. Embassy Seal". In: *The New York Times* (May 26, 1960). URL: `https://www.nytimes.com/1960/05/27/archives/lodge-tells-un-symbol-was-gift-from-russians-russians-tapped-us.html?legacy=true`.

[20] *Measurement of Radar Cross Section Using the VNA Master Handheld VNA*. Tech. rep. Anritsu, 2011, p. 12. URL: `https://dl.cdn-anritsu.com/en-us/test-measurement/files/Application-Notes/Application-Note/11410-00604B.pdf`.

[21] *AEM40940 Highly-efficient, regulated dual-output, ambient energy manager for high-frequency RF input with optional primary battery*. Tech. rep. e-Peas semiconductors, 2018, p. 25. URL: `https://e-peas.com/wp-content/uploads/2020/04/E-peas_RF_Energy_Harvesting_Datasheet_AEM40940.pdf`.

[22] *ETSI Regulations: EN 302 208 V3.1.1 (2016-11)*. Tech. rep. ETSI, 2016, p. 69. URL: `https://www.etsi.org/deliver/etsi_en/302200_302299/302208/03.01.01_60/en_302208v030101p.pdf`.

[23] *TLV703x and TLV704x Small-Size, Nanopower, Low-Voltage Comparators*. Tech. rep. Texas Instruments, 2017, p. 62. URL: `https://www.ti.com/lit/ds/symlink/tlv7031.pdf`.

[24] *ADG839 Single SPDT Switch/2:1 MUX*. Tech. rep. Analog Devices, 2004, p. 16. URL: `https://www.analog.com/media/en/technical-documentation/data-sheets/adg839.pdf`.

[25] *LTC6906 Micropower, 10kHz to 1MHz Resistor Set Oscillator*. Tech. rep. Linear Technology, 2005, p. 14. URL: `https://www.analog.com/media/en/technical-documentation/data-sheets/6906fc.pdf`.

[26] *ADG904 CMOS 1.65 V to 2.75 V, 4:1 Mux/SP4T*. Tech. rep. Analog Devices, 2016, p. 16. URL: `https://www.analog.com/media/en/technical-documentation/data-sheets/adg904.pdf`.

[27] *InfiniiVision 2000 X-Series Oscilloscopes*. Tech. rep. Keysight Technologies, 2019, p. 30. URL: `https://www.keysight.com/be/en/assets/7018-02733/data-sheets/5990-6618.pdf`.

[28] Qoitech. *Otii Arc User Manual*. 2022. URL: `https://www.qoitech.com/docs/user-manual/otii`.

[29] *Manganese Dioxide Lithium Coin Batteries: Individual Specifications*. Tech. rep. Panasonic, 2005, p. 1. URL: `http://www.cr2032.co/cms/prodimages/panasonic_cr2032_datasheet.pdf`.

[30] *SMC100A Signal Generator Specifications*. Tech. rep. Rohde & Schwarz, 2011, p. 16. URL: `https://scdn.rohde-schwarz.com/ur/pws/dl_downloads/dl_common_library/dl_brochures_and_datasheets/pdf_1/SMC100A_dat-sw_en.pdf`.

[31] *Raspberry Pi 4 Computer Model B Datasheet*. Tech. rep. Raspberry Pi, 2019, p. 6. URL: `https://datasheets.raspberrypi.com/rpi4/raspberry-pi-4-datasheet.pdf`.

[32] abyz. *The pigpio library*. 2021. URL: `https://abyz.me.uk/rpi/pigpio/`.

[33] GNU Radio. *GNU Radio Usage Manual*. 2020. URL: `https://wiki.gnuradio.org/index.php/Usage_Manual`.

[34] *USRP B200/B210 Bus Series*. Tech. rep. Ettus Research, 2019, p. 2. URL: `https://www.ettus.com/wp-content/uploads/2019/01/b200-b210_spec_sheet.pdf`.

Bibliography

[AA12]   A. E. Abdulhadi and R. Abhari. "Design and Experimental Evaluation of Miniaturized Monopole UHF RFID Tag Antennas". In: *IEEE Antennas and Wireless Propagation Letters* 11 (2012), pp. 248–251. DOI: `10.1109/LAWP.2012.2187632`.

[AB79]   J. Allen and D. Berkley. "Image method for efficiently simulating small-room acoustics". In: *The Journal of the Acoustical Society of America* 65 (Apr. 1979), pp. 943–950. DOI: `10.1121/1.382599`.

[Adu+18]   K. S. Adu-Manu, N. Adam, C. Tapparello, H. Ayatollahi, and W. Heinzelman. "Energy-Harvesting Wireless Sensor Networks (EH-WSNs): A Review". In: *ACM Trans. Sen. Netw.* 14.2 (Apr. 2018). ISSN: 1550-4859.

[Agu+20]   T. Aguilera, F. J. Alvarez, J. A. Paredes, and J. A. Moreno. "Doppler compensation algorithm for chirp-based acoustic local positioning systems". In: *Digital Signal Processing* 100 (2020), p. 102704. ISSN: 1051-2004.

[Ali+09]   C. Alippi, G. Anastasi, M. Di Francesco, and M. Roveri. "Energy management in wireless sensor networks with energy-hungry sensors". In: *IEEE Instrumentation and Measurement Magazine* 12.2 (Apr. 2009), pp. 16–23.

[Ana+08]   G. Anastasi, M. Conti, M. Di Francesco, and A. Passarella. "Energy conservation in wireless sensor networks: A survey". In: *Ad Hoc Networks* 7 (June 2008), pp. 537–568.

[APR07]   M. A. Alves, R. J. Port, and M. C. Rezende. "Simulations of the radar cross section of a stealth aircraft". In: *SBMO/IEEE MTT-S International Microwave and Optoelectronics Conference*. 2007, pp. 409–412. DOI: `10.1109/IMOC.2007.4404292`.

[Arn+18]   M. Arnela, O. Guasch, P. Sánchez-Martín, J. Camps, R. M. Alsina-Pagès, and C. Martínez-Suquía. "Construction of an Omnidirectional Parametric Loudspeaker Consisting in a Spherical Distribution of Ultrasound Transducers". In: *Sensors* 18.12 (Dec. 2018), E4317. DOI: `10.3390/s18124317`.

[Awa+16]   M. R. Awal, M. Jusoh, T. Sabapathy, M. R. Kamarudin, and R. A. Rahim. "State-of-the-Art Developments of Acoustic Energy Transfer". In: *International Journal of Antennas and Propagation* 2016 (July 2016), pp. 1–14.

[Bal05]   C. A. Balanis. *Antenna Theory: Analysis and Design*. USA: Wiley-Interscience, 2005. ISBN: 0471714623.

[Ban85]   S. Bancroft. "An Algebraic Solution of the GPS Equations". In: *IEEE Transactions on Aerospace and Electronic Systems* 21.1 (1985), pp. 56–59. DOI: `10.1109/TAES.1985.310538`.

[Bar+21]   P. Barsocchi, A. Calabrò, A. Crivello, S. Daoudagh, F. Furfari, M. Girolami, and E. Marchetti. "COVID-19 & privacy: Enhancing of indoor localization architectures towards effective social distancing". In: *Array* 9 (2021), p. 100051. ISSN: 2590-0056. DOI: `0.1016/j.array.2020.100051`.

[Bar19]   T. Bart. "Indoor Localization in Energy Constrained Wireless Acoustic Sensor Networks". PhD thesis. KU Leuven, Nov. 2019.

[BB18]   Y. Bai and P.-J. Bouvet. "Orthogonal Chirp Division Multiplexing for Underwater Acoustic Communication". In: *Sensors* 18.11 (2018), pp. 1–13.

[BDS10]   A. Bletsas, A. G. Dimitriou, and J. N. Sahalos. "Improving Backscatter Radio Tag Efficiency". In: *IEEE Transactions on Microwave Theory and Techniques* 58.6 (2010), pp. 1502–1509. DOI: `10.1109/TMTT.2010.2047916`.

[BEH18]   C. Bradley, S. El-Tawab, and M. H. Heydari. "Security analysis of an IoT system used for indoor localization in healthcare facilities". In: *Systems and Information Engineering Design Symposium (SIEDS)*. 2018, pp. 147–152. DOI: `10.1109/SIEDS.2018.8374726`.

[Ber+20]   C. Bernard, P.-J. Bouvet, A. Pottier, and P. Forjonel. "Multiuser Chirp Spread Spectrum Transmission in an Underwater Acoustic Channel Applied to an AUV Fleet". In: *Sensors (Basel, Switzerland)* 20.5 (Mar. 2020), p. 1527. ISSN: 1424-8220. DOI: `10.3390/s20051527`.

[Bha+15]   D. Bharadia, K. R. Joshi, M. Kotaru, and S. Katti. "BackFi– High Throughput WiFi Backscatter". In: SIGCOMM '15. London, United Kingdom, 2015, pp. 283–296. DOI: `10.1145/2785956.2787490`.

[BSD16]   A. Boyden, V. K. Soo, and M. Doolan. "The Environmental Impacts of Recycling Portable Lithium-Ion Batteries". In: *Procedia CIRP* 48 (2016), pp. 188–193. DOI: `10.1016/j.procir.2016.03.100`.

[BSL08]   A. Beck, P. Stoica, and J. Li. "Exact and Approximate Solutions of Source Localization Problems". In: *IEEE Transactions on Signal Processing* 56.5 (2008), pp. 1770–1778. DOI: `10.1109/TSP.2007.909342`.

[Buy+21]   C. Buyle, B. Cox, L. Van der Perre, and L. De Strycker. "A Multi-band Solution for Interacting with Energy-Neutral Devices". In: *55th Asilomar Conference on Signals, Systems, and Computers*. 2021, pp. 329–333. DOI: `10.1109/IEEECONF53345.2021.9723184`.

[Cad+16]   C. Cadena, L. Carlone, H. Carrillo, Y. Latif, D. Scaramuzza, J. Neira, I. Reid, and J. J. Leonard. "Past, Present, and Future of Simultaneous Localization and Mapping: Toward the Robust-Perception Age". In: *IEEE Transactions on Robotics* 32.6 (2016), pp. 1309–1332.

[Caf00]   J. Caffery. "A new approach to the geometry of TOA location". In: *52nd Vehicular Technology Conference*. Vol. 4. 2000, 1943–1949 vol.4. DOI: `10.1109/VETECF.2000.886153`.

[CAK19]   M. Cansiz, D. Altinel, and G. K. Kurt. "Efficiency in RF energy harvesting systems: A comprehensive review". In: *Energy* 174 (2019), pp. 292–309.

[Cal+21]   G. Callebaut, G. Leenders, J. Van Mulders, G. Ottoy, L. De Strycker, and L. Van der Perre. "The Art of Designing Remote IoT Devices—Technologies and Strategies for a Long Battery Life". In: *Sensors* 21.3 (2021). DOI: 10.3390/s21030913.

[Cal+22]   G. Callebaut, J. V. Mulders, G. Ottoy, D. Delabie, B. Cox, N. Stevens, and L. V. der Perre. *Techtile – Open 6G R&D Testbed for Communication, Positioning, Sensing, WPT and Federated Learning.* 2022. arXiv: 2202.04524.

[Cao+20]   S. Cao, X. Chen, X. Zhang, and X. Chen. "Effective Audio Signal Arrival Time Detection Algorithm for Realization of Robust Acoustic Indoor Positioning". In: *IEEE Transactions on Instrumentation and Measurement* 69.10 (2020), pp. 7341–7352.

[Car+17]   R. Carotenuto, M. Merenda, D. Iero, and F. G. D. Corte. "Using ANT Communications for Node Synchronization and Timing in a Wireless Ultrasonic Ranging System". In: *IEEE Sensors Letters* 1.6 (2017), pp. 1–4.

[Car+18]   R. Carotenuto, M. Merenda, D. Iero, and F. G. D. Corte. "Ranging RFID Tags With Ultrasound". In: *IEEE Sensors Journal* 18.7 (2018), pp. 2967–2975.

[Car+19]   R. Carotenuto, M. Merenda, D. Iero, and F. G. Della Corte. "An Indoor Ultrasonic System for Autonomous 3-D Positioning". In: *IEEE Transactions on Instrumentation and Measurement* 68.7 (2019), pp. 2507–2518.

[CCF12]   C. C. Cruz, J. R. Costa, and C. A. Fernandes. "Design of a passive tag for indoor localization". In: *6th European Conference on Antennas and Propagation (EUCAP)*. 2012, pp. 2495–2499.

[CCF13]   C. C. Cruz, J. R. Costa, and C. A. Fernandes. "Hybrid UHF/UWB Antenna for Passive Indoor Identification and Localization Systems". In: *IEEE Transactions on Antennas and Propagation* 61.1 (2013), pp. 354–361.

[Che+04]   K. Cheung, H. So, W.-K. Ma, and Y. Chan. "Least squares algorithms for time-of-arrival-based mobile location". In: *IEEE Transactions on Signal Processing* 52.4 (2004), pp. 1121–1130. DOI: 10.1109/TSP.2004.823465.

[Che+19]   X. Chen, Y. Chen, S. Cao, L. Zhang, X. Zhang, and X. Chen. "Acoustic Indoor Localization System Integrating TDMA+FDMA Transmission Scheme and Positioning Correction Technique". In: *Sensors* 19.10 (2019). ISSN: 1424-8220.

[Chr05]   C. Christensen. "A new scattering method that combines roughness and diffraction effects". In: *Journal of The Acoustical Society of America* 117 (Apr. 2005). DOI: 10.1121/1.4788035.

[CM08]   O. Z. Chaudhry and W. A. Mackaness. "Creating Mountains out of Mole Hills: Automatic Identification of Hills and Ranges Using Morphometric Analysis". In: *Transactions in GIS* 12.5 (2008), pp. 567–589.

[Cox+20a]   B. Cox, L. Van der Perre, S. Wielandt, G. Ottoy, and L. De Strycker. "High precision hybrid RF and ultrasonic chirp-based ranging for low-power IoT nodes." In: *EURASIP Journal on Wireless Communications and Networking* 2020.187 (2020).

[Cox+20b]   B. Cox, C. Buyle, L. Van der Perre, and L. De Strycker. "Energy-Neutral Devices: Can Hybrid RF-Acoustic Signals Point Them Out?" In: *2020 54th Asilomar Conference on Signals, Systems, and Computers*. 2020, pp. 657–661. DOI: 10.1109/IEEECONF51394.2020.9443432.

[Cox+22]   B. Cox, C. Buyle, D. Delabie, L. De Strycker, and L. Van der Perre. "Positioning Energy-Neutral Devices: Technological Status and Hybrid RF-Acoustic Experiments". In: *Future Internet* 14.5 (2022). DOI: `10.3390/fi14050156`.

[CSQ08]   Q. M. Chaudhari, E. Serpedin, and K. Qaraqe. "On Maximum Likelihood Estimation of Clock Offset and Skew in Networks With Exponential Delays". In: *IEEE Transactions on Signal Processing* 56.4 (2008), pp. 1685–1697. DOI: `10.1109/TSP.2007.910536`.

[CVD20]   B. Cox, L. Van der Perre, and L. De Strycker. "Zero-Crossing Chirp Frequency Demodulation for Ultra-Low-Energy Precise Hybrid RF-Acoustic Ranging of Mobile Nodes". In: *IEEE Sensors Letters* 4.5 (2020), pp. 1–4.

[Das+16]   S. Daskalakis, S. D. Assimonis, E. Kampianakis, and A. Bletsas. "Soil Moisture Scatter Radio Networking With Low Power". In: *IEEE Transactions on Microwave Theory and Techniques* 64.7 (2016), pp. 2338–2346. DOI: `10.1109/TMTT.2016.2572677`.

[De +15]   E. De Sena, N. Antonello, M. Moonen, and T. van Waterschoot. "On the Modeling of Rectangular Geometries in Room Acoustic Simulations". In: *IEEE/ACM Transactions on Audio, Speech, and Language Processing* 23.4 (2015), pp. 774–786. DOI: `10.1109/TASLP.2015.2405476`.

[Dek+17]   G. Dekkers, S. Lauwereins, B. Thoen, M. W. Adhana, H. Brouckxon, B. Van den Bergh, T. van Waterschoot, B. Vanrumste, M. Verhelst, and P. Karsmakers. "The SINS database for detection of daily activities in a home environment using an Acoustic Sensor Network". In: DCASE Workshop, 2017, pp. 1–5.

[Del+22]   D. Delabie, B. Cox, L. D. Strycker, and L. V. der Perre. *Techtile: a Flexible Testbed for Distributed Acoustic Indoor Positioning and Sensing*. 2022. arXiv: `2204.06352`.

[Dep+18]   A. Depari, A. Flammini, D. Fogli, and P. Magrino. "Indoor Localization for Evacuation Management in Emergency Scenarios". In: *Workshop on Metrology for Industry 4.0 and IoT*. 2018, pp. 146–150. DOI: `10.1109/METROI4.2018.8428343`.

[DM14]   E. DiGiampaolo and F. Martinelli. "Mobile Robot Localization Using the Phase of Passive UHF RFID Signals". In: *IEEE Transactions on Industrial Electronics* 61.1 (2014), pp. 365–376.

[Dob07]   D. M. Dobkin. *The RF in RFID: Passive UHF RFID in Practice*. USA: Newnes, 2007. ISBN: 0750682094.

[DP10]   W. Dargie and C. P. Poellabauer. "Time Synchronisation". In: *Location Based Services and TeleCartography II: From Sensor Fusion to Context Models*. Hoboken, United States: Wiley, 2010, pp. 229–248. ISBN: 978-0-470-97568-8.

[EDP10]   A. F. C. Errington, B. L. F. Daku, and A. F. Prugger. "Initial Position Estimation Using RFID Tags: A Least-Squares Approach". In: *IEEE Transactions on Instrumentation and Measurement* 59.11 (2010), pp. 2863–2869.

[Els+22]   M. Elsanhoury, P. Mäkelä, J. Koljonen, P. Välisuo, A. Shamsuzzoha, T. Mantere, M. Elmusrati, and H. Kuusniemi. "Precision Positioning for Smart Logistics Using Ultra-Wideband Technology-Based Indoor Navigation: A Review". In: *IEEE Access* 10 (2022), pp. 44413–44445. DOI: `10.1109/ACCESS.2022.3169267`.

[ER15]   J. F. Ensworth and M. S. Reynolds. "Every smart phone is a backscatter reader:
            Modulated backscatter compatibility with Bluetooth 4.0 Low Energy (BLE)
            devices". In: *IEEE International Conference on RFID*. 2015, pp. 78–85. DOI:
            `10.1109/RFID.2015.7113076`.

[ER17]   J. F. Ensworth and M. S. Reynolds. "BLE-Backscatter: Ultralow-Power IoT
            Nodes Compatible With Bluetooth 4.0 Low Energy (BLE) Smartphones and
            Tablets". In: *IEEE Transactions on Microwave Theory and Techniques* 65.9
            (2017), pp. 3360–3368. DOI: `10.1109/TMTT.2017.2687866`.

[ES01]   F. Everest and N. Shaw. "Master Handbook of Acoustics, Fourth Edition". In:
            Journal of The Acoustical Society of America - J ACOUST SOC AMER 110
            (Oct. 2001).

[Fab+20]   D. Fabbri, N. Decarli, A. Guerra, A. Romani, and D. Dardari. "High-Accuracy
            Positioning of Battery-Less Hybrid Gen2 UHF-UWB Tags". In: *54th Asilomar
            Conference on Signals, Systems, and Computers*. 2020, pp. 646–650.

[FHP98]   E. Foxlin, M. Harrington, and G. Pfeifer. "Constellation: a wide-range wireless
            motion-tracking system for augmented reality and virtual set applications". In:
            *Proceedings of the 25th annual conference on Computer graphics and interactive
            techniques* (1998).

[FLL13]   V. Ferro, A. Luz, and A. Lucrecio. "Small Long Range UHF Tag for Metal
            Applications". In: *IEEE International Conference on RFID-Technologies and
            Applications* (2013), pp. 1–6. DOI: `10.1109/RFID-TA.2013.6694521`.

[Flu+20]   L. Flueratoru, S. Wehrli, M. Magno, and D. Niculescu. "On the Energy
            Consumption and Ranging Accuracy of Ultra-Wideband Physical Interfaces". In:
            IEEE Global Communications Conference. 2020, pp. 1–7.

[FR09]   Q. Fu and G. Retscher. "Using RFID and INS for Indoor Positioning". In: *Location
            Based Services and TeleCartography II: From Sensor Fusion to Context Models*.
            Berlin, Heidelberg: Springer, 2009, pp. 421–438. ISBN: 978-3-540-87393-8.

[Fri46]   H. Friis. "A Note on a Simple Transmission Formula". In: *Proceedings of the IRE*
            34.5 (1946), pp. 254–256. DOI: `10.1109/JRPROC.1946.234568`.

[FTW21]   J. Friedrich, J. Tiemann, and C. Wietfeld. "Accurate Multi-Zone UWB TDOA
            Localization utilizing Cascaded Wireless Clock Synchronization". In: *International
            Conference on Indoor Positioning and Indoor Navigation (IPIN)*. 2021, pp. 1–8.
            DOI: `10.1109/IPIN51156.2021.9662537`.

[Gar+15]   E. García, J. A. Paredes, F. J. Álvarez, M. C. Pérez, and J. J. García. "Spreading
            sequences in active sensing: A review". In: *Signal Processing* 106 (2015), pp. 88–
            105. ISSN: 0165-1684. DOI: `10.1016/j.sigpro.2014.07.002`.

[Gol+04]   D. H. Goldberg, A. G. Andreou, P. Julian, P. O. Pouliquen, L. Riddle, and
            R. Rosasco. "A Wake-Up Detector for an Acoustic Surveillance Sensor Network:
            Algorithm and VLSI Implementation". In: *ISPN'04* (Apr. 2004), pp. 134–141.

[Gom+22]   E. L. Gomes, M. Fonseca, A. E. Lazzaretti, A. Munaretto, and C. Guerber.
            "Clustering and Hierarchical Classification for High-Precision RFID Indoor
            Location Systems". In: *IEEE Sensors Journal* 22.6 (2022), pp. 5141–5149.

[Gre63]   R. B. Green. "The general theory of antenna scattering". PhD thesis. The Ohio
            State University, 1963.

[Ham+17]   A. Hamani, M. C. E. Yagoub, T. Vuong, and R. Touhami. "A Novel Broadband Antenna Design for UHF RFID Tags on Metallic Surface Environments". In: *IEEE Antennas and Wireless Propagation Letters* 16 (2017), pp. 91–94. DOI: `10.1109/LAWP.2016.2557778`.

[Han89]   R. C. Hansen. "Relationships between antennas as scatterers and as radiators". In: *Proceedings of the IEEE* 77.5 (1989), pp. 659–662.

[Har+02]   A. Harter, A. Hopper, P. Steggles, A. Ward, and P. Webster. "The Anatomy of a Context-Aware Application". In: *Wireless Networks* 8.2 (Mar. 2002), pp. 187–197. DOI: `10.1023/A:1013767926256`.

[HC16]   S. He and S.-H. G. Chan. "Wi-Fi Fingerprint-Based Indoor Positioning: Recent Advances and Comparisons". In: *IEEE Communications Surveys Tutorials* 18.1 (2016), pp. 466–490.

[HDK16]   A. Hammoud, M. Deriaz, and D. Konstantas. "Robust Ultrasound-Based Room-Level Localization System Using COTS Components". In: *UPINLBS '16* (Nov. 2016).

[Hei04]   A. Hein. *Processing of SAR Data: Fundamentals, Signal Processing, Interferometry*. Springer, 2004, pp. 471–478.

[Hol09]   S. Holm. "Hybrid ultrasound-RFID indoor positioning: Combining the best of both worlds". In: *IEEE International Conference on RFID*. 2009, pp. 155–162. DOI: `10.1109/RFID.2009.4911169`.

[HW02]   M. Hazas and A. Ward. "A Novel Broadband Ultrasonic Location System". In: *Ubiquitous Computing*. Berlin, Heidelberg: Springer, 2002, pp. 264–280.

[Ija+13]   F. Ijaz, H. K. Yang, A. W. Ahmad, and C. Lee. "Indoor positioning: A review of indoor ultrasonic positioning systems". In: *15th International Conference on Advanced Communications Technology*. 2013, pp. 1146–1150.

[Iye+16]   V. Iyer, V. Talla, B. Kellogg, S. Gollakota, and J. Smith. "Inter-Technology Backscatter: Towards Internet Connectivity for Implanted Devices". In: *Proceedings of the 2016 ACM SIGCOMM Conference*. Florianopolis, Brazil, 2016, pp. 356–369. ISBN: 9781450341936.

[Jin+14]   M. Jin, B. Koo, S. Lee, C. Park, M. J. Lee, and S. Kim. "IMU-assisted nearest neighbor selection for real-time WiFi fingerprinting positioning". In: *International Conference on Indoor Positioning and Indoor Navigation (IPIN)*. 2014, pp. 745–748. DOI: `10.1109/IPIN.2014.7275556`.

[Kap16]   N. Kaplanis. "Perception of Reverberation in Domestic and Automotive Environments". PhD thesis. Aalborg University, Dec. 2016, p. 229.

[Kel+14]   B. Kellogg, A. Parks, S. Gollakota, J. R. Smith, and D. Wetherall. "Wi-Fi Backscatter: Internet Connectivity for RF-Powered Devices". In: *Proceedings of the 2014 ACM Conference on SIGCOMM*. SIGCOMM '14. 2014, pp. 607–618. ISBN: 9781450328364.

[Kel+16]   B. Kellogg, V. Talla, S. Gollakota, and J. R. Smith. "Passive Wi-Fi: Bringing Low Power to Wi-Fi Transmissions". In: *13th USENIX Symposium on Networked Systems Design and Implementation*. Mar. 2016, pp. 151–164. ISBN: 978-1-931971-29-4.

[Khy+17]   M. O. Khyam, S. Sam Ge, X. Li, and M. Pickering. "Orthogonal Chirp-Based Ultrasonic Positioning". In: *Sensors 2017* 17 (July 2017).

[Kle+01]   N. Klepeis, W. Nelson, W. Ott, J. Robinson, A. Tsang, P. Switzer, J. Behar, S. Hern, and W. Engelmann. "The National Human Activity Pattern Survey (NHAPS): A resource for assessing exposure to environmental pollutants". In: *Journal of exposure analysis and environmental epidemiology* 11 (Mar. 2001), pp. 231–52. DOI: `10.1038/sj.jea.7500165`.

[Kon+18]   J. Konecny, M. Prauzek, R. Martinek, L. Michalek, and M. Tomis. "Real-time Patient Localization in Urgent Care: System Design and Hardware Perspective". In: *IEEE 20th International Conference on e-Health Networking, Applications and Services*. 2018, pp. 1–5. DOI: `10.1109/HealthCom.2018.8531110`.

[Kro68]   L. Kronecker. "Ueber bilineare Formen." In: *Journal fur die reine und angewandte Mathematik* 68 (1868), pp. 273–285.

[KST04]   E. F. Knott, J. F. Schaeffer, and T. M. Tulley. *Radar Cross Section*. USA: SciTech Publishing, 2004. ISBN: 1891121251.

[Kuo+22]   S.-K. Kuo, M. Dunna, D. Bharadia, and P. P. Mercier. "A WiFi and Bluetooth Backscattering Combo Chip Featuring Beam Steering via a Fully-Reflective Phased-Controlled Multi-Antenna Termination Technique Enabling Operation Over 56 Meters". In: *IEEE International Solid- State Circuits Conference (ISSCC)*. Vol. 65. 2022, pp. 1–3.

[Kup05]   A. Kupper. *Location-based services: fundamentals and applications.* eng. Chichester: Wiley, 2005. ISBN: 0470092319.

[Kut06]   H. Kuttruff. *Acoustics*. CRC Press, Nov. 2006.

[Kut16]   H. Kuttruff. *Room acoustics*. CRC Press, 2016.

[KWV13]   T. Knüttel, I. B. Witew, and M. Vorländer. "Influence of "omnidirectional" loudspeaker directivity on measured room impulse responses". In: *The Journal of the Acoustical Society of America* 134.5 (Nov. 2013), pp. 3654–3662.

[La +19]   R. La Rosa, P. Livreri, C. Trigona, L. Di Donato, and G. Sorbello. "Strategies and Techniques for Powering Wireless Sensor Nodes through Energy Harvesting and Wireless Power Transfer". In: *Sensors* 19.12 (June 2019), p. 2660. ISSN: 1424-8220.

[Lan05]   J. Landt. "The history of RFID". In: *IEEE Potentials* 24.4 (2005), pp. 8–11. DOI: `10.1109/MP.2005.1549751`.

[Li+19]   X. Li, E. Leitinger, M. Oskarsson, K. Åström, and F. Tufvesson. "Massive MIMO-Based Localization and Mapping Exploiting Phase Information of Multipath Components". In: *IEEE Transactions on Wireless Communications* 18.9 (2019), pp. 4254–4267.

[Li+21a]   L. Li, X. Zhang, C. Song, W. Zhang, T. Jia, and Y. Huang. "Compact Dual-Band, Wide-Angle, Polarization- Angle -Independent Rectifying Metasurface for Ambient Energy Harvesting and Wireless Power Transfer". In: *IEEE Transactions on Microwave Theory and Techniques* 69.3 (2021), pp. 1518–1528. DOI: `10.1109/TMTT.2020.3040962`.

[Li+21b]   S. Li, F. Cheng, C. Gu, S. Yu, and K. Huang. "Efficient Dual-Band Rectifier Using Stepped Impedance Stub Matching Network for Wireless Energy Harvesting". In: *IEEE Microwave and Wireless Components Letters* 31.7 (2021), pp. 921–924. DOI: `10.1109/LMWC.2021.3078546`.

[Li+21c]   Y. Li, X. Liu, X. Wang, Q. Su, S. Zhao, Z. Wang, and Y. Liu. "A High Conversion Gain Envelope Detector with Wide Input Range for Simultaneous Wireless Information and Power Transfer System". In: *Electronics* 10.2 (2021). ISSN: 2079-9292.

[Lin+21]   L. Lin, K. A. Ahmed, P. S. Salamani, and M. Alioto. "Battery-Less IoT Sensor Node with PLL-Less WiFi Backscattering Communications in a 2.5-uW Peak Power Envelope". In: *Symposium on VLSI Circuits*. 2021, pp. 1–2.

[Liu+13]   V. Liu, A. Parks, V. Talla, S. Gollakota, D. Wetherall, and J. R. Smith. "Ambient Backscatter: Wireless Communication out of Thin Air". In: *SIGCOMM Comput. Commun. Rev.* 43.4 (Aug. 2013), pp. 39–50. DOI: 10.1145/2534169.2486015.

[Liu+20]   W. Liu, K. Huang, T. Wang, Z. Zhang, and J. Hou. "A Broadband High-Efficiency RF Rectifier for Ambient RF Energy Harvesting". In: *IEEE Microwave and Wireless Components Letters* 30.12 (2020), pp. 1185–1188. DOI: 10.1109/LMWC.2020.3028607.

[LR12]   P. Lazik and A. Rowe. "Indoor Pseudo-ranging of Mobile Devices using Ultrasonic Chirps". In: *SenSys '12* (Nov. 2012).

[Lu+15]   X. Lu, P. Wang, D. Niyato, D. I. Kim, and Z. Han. "Wireless Networks With RF Energy Harvesting: A Contemporary Survey". In: *IEEE Communications Surveys Tutorials* 17.2 (2015), pp. 757–789. DOI: 10.1109/COMST.2014.2368999.

[Ma+12]   Z. L. Ma, L. J. Jiang, J. Xi, and T. T. Ye. "A Single-Layer Compact HF-UHF Dual-Band RFID Tag Antenna". In: *IEEE Antennas and Wireless Propagation Letters* 11 (2012), pp. 1257–1260. DOI: 10.1109/LAWP.2012.2225821.

[Mag+17]   M. Magno, F. A. Aoudia, M. Gautier, O. Berder, and L. Benini. "WULoRa: An energy efficient IoT end-node for energy harvesting and heterogeneous communication". In: *Design, Automation Test in Europe Conference Exhibition*. 2017, pp. 1528–1533.

[Man+19]   K. Mannay, J. Urena, A. Hernandez, M. Machhout, and T. Aguili. "3D Ultrasonic Indoor Local Positioning System: Study and Implementation". In: *The Convergence of 5G & Smart Computing Days*. Feb. 2019.

[Mar+92]   D. Marioli, N. C., C. Offelli, D. Petri, E. Sardini, and A. Taroni. "Digital Time-Of-Flight Measurement for Ultrasonic Sensors". In: *IEEE Trans. On Instrumentation and Measurement* 41.1 (Feb. 1992), pp. 93–97.

[MB18]   P. Malcovati and A. Baschirotto. "The Evolution of Integrated Interfaces for MEMS Microphones". In: *Micromachines* 9.7 (June 2018), p. 323.

[Mer+21]   M. Merenda, L. Catarinucci, R. Colella, F. G. Della Corte, and R. Carotenuto. "Exploiting RFID technology for Indoor Positioning". In: *6th International Conference on Smart and Sustainable Technologies*. 2021, pp. 1–5.

[MH21]   K. Majeed and S. Hranilovic. "Passive Indoor Visible Light Positioning System Using Deep Learning". In: *IEEE Internet of Things Journal* 8.19 (2021), pp. 14810–14821. DOI: 10.1109/JIOT.2021.3072201.

[MSD13]   C. Medina, J. C. Segura, and A. De la Torre. "Ultrasound indoor positioning system based on a low-power wireless sensor network providing sub-centimeter accuracy". In: *Sensors* 13.3 (2013), pp. 3501–3526.

[MT11]   R. Mautz and S. Tilch. "Survey of optical indoor positioning systems". In: *International Conference on Indoor Positioning and Indoor Navigation*. 2011, pp. 1–7. DOI: 10.1109/IPIN.2011.6071925.

[MTH19]   G. M. Mendoza-Silva, J. Torres-Sospedra, and J. Huerta. "A Meta-Review of Indoor Positioning Systems". In: *Sensors* 19.20 (2019).

[Mun+09]   D. Munoz, F. L. Bouchereau, C. Vargas, and R. Enriquez-Caldera. *Position Location Techniques and Applications*. 1st ed. Burlington, MA: Academic Press, Elsevier, 2009. ISBN: 9780123743534.

[Mur+20]   S. Murano, C. Pérez-Rubio, D. Gualda, F. J. Álvarez, T. Aguilera, and C. D. Marziani. "Evaluation of Zadoff–Chu, Kasami, and Chirp-Based Encoding Schemes for Acoustic Local Positioning Systems". In: *IEEE Transactions on Instrumentation and Measurement* 69.8 (2020), pp. 5356–5368. DOI: 10.1109/TIM.2019.2959290.

[Nad+18]   S. Naderiparizi, M. Hessar, V. Talla, S. Gollakota, and J. R. Smith. "Towards Battery-Free HD Video Streaming". In: *NSDI 18*. Apr. 2018, pp. 233–247.

[Nak+01]   K. Nakahira, T. Kodama, S. Morita, and S. Okuma. "Distance Measurements by an Ultrasonic System Based on a Digital Polarity Correlator". In: *IEEE Trans. On Instrumentation and Measurement* 50.6 (Dec. 2001), pp. 1748–1752.

[Nie13]   T. M. Niebauer. "Analytic signal demodulation of phase-modulated frequency-chirped signals". In: *Applied Optics* 52.9 (Mar. 2013), pp. 1838–1846.

[NL19]   J.-P. Niu and G. Y. Li. "An Overview on Backscatter Communications". In: *Journal of Communications and Information Networks* 4.2 (2019), pp. 1–14. DOI: 10.23919/JCIN.2019.8917868.

[NRM07]   P. Nikitin, K. Rao, and R. Martinez. "Differential RCS of RFID tag". In: *Electronics Letters* 43 (Feb. 2007), pp. 431–432. DOI: 10.1049/el:20070253.

[Ogi21]   S. Ogiso. "Robust acoustic localization in a reverberant environment for synchronous and asynchronous beacons". In: *International Conference on Indoor Positioning and Indoor Navigation (IPIN)*. 2021, pp. 1–8.

[Ogu+18]   G. Oguntala, R. Abd-Alhameed, S. Jones, J. Noras, M. Patwary, and J. Rodriguez. "Indoor location identification technologies for real-time IoT-based applications: An inclusive survey". In: *Computer Science Review* 30 (2018), pp. 55–79. ISSN: 1574-0137.

[Par+21]   T. Partanen, P. Muller, J. Collin, and J. Bjorklund. "Implementation and Accuracy Evaluation of Fixed Camera-Based Object Positioning System Employing CNN-Detector". In: *9th European Workshop on Visual Information Processing (EUVIP)*. 2021, pp. 1–6. DOI: 10.1109/EUVIP50544.2021.9483987.

[Pen+18]   Y. Peng, L. Shangguan, Y. Hu, Y. Qian, X. Lin, X. Chen, D. Fang, and K. Jamieson. "PLoRa: A Passive Long-Range Data Network from Ambient LoRa Transmissions". In: SIGCOMM '18. Budapest, Hungary, 2018, pp. 147–160. DOI: 10.1145/3230543.3230567.

[PJF91]   M. Parrilla, A. J., and C. Fritsch. "Digital Signal Processing Techniques for High Accuracy Ultrasonic Range Measurements". In: *IEEE Trans. On Instrumentation and Measurement* 40.4 (Aug. 1991), pp. 759–763.

[Pos+22]   I. V. Pospelova, I. V. Cherepanova, D. S. Bragin, I. A. Sidorov, E. Y. Kostyuchenko, and V. N. Serebryakova. "The Estimation of the Potential for Using Smart-Trackers as a Part of a Medical Indoor-Positioning System". In: *Electronics* 11.1 (2022). DOI: 10.3390/electronics11010107.

[Pri+09] J. C. Prieto, A. R. Jimenez, J. Guevara, J. L. Ealo, F. Seco, J. O. Roa, and F. Ramos. "Performance Evaluation of 3D-LOCUS Advanced Acoustic LPS". In: *IEEE Transactions on Instrumentation and Measurement* 58.8 (2009), pp. 2385–2395. DOI: 10.1109/TIM.2009.2016378.

[Pri05]   N. B. Priyantha. "The Cricket Indoor Location System". PhD thesis. USA, 2005.

[Que+14] C. Quested, A. Moorhouse, B. Piper, and B. Hu. "An analytical model for a dodecahedron loudspeaker applied to the design of omni-directional loudspeaker arrays". In: *Applied Acoustics* 85 (2014), pp. 161–171. DOI: https://doi.org/10.1016/j.apacoust.2014.03.023.

[Rae22]   W. Raes. "Machine Learning as a Means for Highly Accurate, RSS-based Visible Light Positioning in Industrial Environments". PhD thesis. KU Leuven, Jan. 2022.

[RC09]   J. Rindel and C. Christensen. "Auralisation of a symphony orchestra with odeon – the chain from musical instruments to the eardrums". In: *Proc. of the EAA Symposium on Auralization*. June 2009, p. 6.

[RD14]   M. Razzaque and S. Dobson. "Energy-Efficient Sensing in Wireless Sensor Networks Using Compressed Sensing". In: *Sensors* 14 (Feb. 2014), pp. 2822–2859.

[Rek+21] A. S. Rekhi, E. So, A. Gural, and A. Arbabian. "CRADLE: Combined RF/Acoustic Detection and Localization of Passive Tags". In: *IEEE Transactions on Circuits and Systems I: Regular Papers* 68.6 (2021), pp. 2555–2568.

[RLW20]   A. B. M. M. Rahman, T. Li, and Y. Wang. "Recent Advances in Indoor Localization via Visible Lights: A Survey". In: *Sensors* 20.5 (2020).

[RNL05]   K. V. S. Rao, P. V. Nikitin, and S. F. Lam. "Antenna design for UHF RFID tags: a review and a practical application". In: *IEEE Transactions on Antennas and Propagation* 53.12 (2005), pp. 3870–3876. DOI: 10.1109/TAP.2005.859919.

[Roy+21] J. J. Roy, S. Rarotra, V. Krikstolaityte, K. W. Zhuoran, Y. D.-I. Cindy, X. Y. Tan, M. Carboni, D. Meyer, Q. Yan, and M. Srinivasan. "Green Recycling Methods to Treat Lithium-Ion Batteries E-Waste: A Circular Approach to Sustainability". In: *Advanced Materials* (2021), p. 2103346.

[Ruc+70] G. T. Ruck, D. E. Barrick, W. D. Stuart, and C. K. Krichbaum. *Radar cross section handbook*. New York: Plenum Press, 1970. ISBN: 0306303434.

[Sae+19] M. Saelens, J. Hoebeke, A. Shahid, and E. D. Poorter. "Impact of EU duty cycle and transmission power limitations for sub-GHz LPWAN SRDs: an overview and future challenges". In: *EURASIP Journal on Wireless Communications and Networking* 2019.1 (Nov. 2019), p. 219.

[SBD17]   R. Scheibler, E. Bezzam, and I. Dokmanic. "Pyroomacoustics: A Python package for audio room simulations and array processing algorithms". In: *CoRR* abs/1710.04196 (2017). arXiv: 1710.04196.

[SGG08]   Z. Sahinoglu, S. Gezici, and I. Guvenc. *Ultra-wideband Positioning Systems: Theoretical Limits, Ranging Algorithms, and Protocols*. Cambridge University Press, 2008. DOI: 10.1017/CBO9780511541056.

[Shr+08] S. Shrestha, M. D. Balachandran, M. Agarwal, L.-H. Zou, and K. Varahramyan. "A Method to Measure Radar Cross Section Parameters of Antennas". In: *IEEE Transactions on Antennas and Propagation* 56.11 (2008), pp. 3494–3500. DOI: 10.1109/TAP.2008.2005541.

[Sir10]   N. Sirola. "Closed-form algorithms in mobile positioning: Myths and misconceptions". In: *7th Workshop on Positioning, Navigation and Communication*. 2010, pp. 38–44. DOI: `10.1109/WPNC.2010.5653789`.

[SN11]   S. S. Saab and Z. S. Nakad. "A Standalone RFID Indoor Positioning System Using Passive Tags". In: *IEEE Transactions on Industrial Electronics* 58.5 (2011), pp. 1961–1970.

[SN99]   J. S. Suh and P. A. Nelson. "Measurement of Transient Response of Rooms and Comparison with Geometrical Acoustic Models". In: *The Journal of the Acoustical Society of America* 105.4 (1999), pp. 2304–2317.

[Sok63]   R. R. Sokal. "The Principles and Practice of Numerical Taxonomy". In: *Taxon* 12.5 (June 1963), pp. 190–199.

[SP20]   P. Spachos and K. N. Plataniotis. "BLE Beacons for Indoor Positioning at an Interactive IoT-Based Smart Museum". In: *IEEE Systems Journal* 14.3 (2020), pp. 3483–3493. DOI: `10.1109/JSYST.2020.2969088`.

[SP80]   D. Sarwate and M. Pursley. "Crosscorrelation properties of pseudorandom and related sequences". In: *Proceedings of the IEEE* 68.5 (1980), pp. 593–619. DOI: `10.1109/PROC.1980.11697`.

[SR20]   J. Singh and U. Raza. "Passive Visible Light Positioning Systems: An Overview". In: LIOT '20. London, United Kingdom, 2020, pp. 48–53. ISBN: 9781450380997.

[ST06]   Sung-Jung Wu and Tzyh-Guang Ma. "A passive UHF RFID meandered tag antenna with tuning stubs". In: *Asia-Pacific Microwave Conference* (2006), pp. 1486–1492. DOI: `10.1109/APMC.2006.4429688`.

[Sto48]   H. Stockman. "Communication by Means of Reflected Power". In: *Proceedings of the IRE* 36.10 (1948), pp. 1196–1204. DOI: `10.1109/JRPROC.1948.226245`.

[Sun+19]   Y. Sun, L. Guan, Z. Chang, C. Li, and Y. Gao. "Design of a Low-Cost Indoor Navigation System for Food Delivery Robot Based on Multi-Sensor Information Fusion". In: *Sensors* 19.22 (2019). DOI: `10.3390/s19224980`.

[SVW22]   T. Savic, X. Vilajosana, and T. Watteyne. "Constrained Localization: A Survey". In: *IEEE Access* 10 (2022), pp. 49297–49321. DOI: `10.1109/ACCESS.2022.3171859`.

[Tah+16]   A. Tahat, G. Kaddoum, S. Yousefi, S. Valaee, and F. Gagnon. "A Look at the Recent Wireless Positioning Techniques With a Focus on Algorithms for Moving Receivers". In: *IEEE Access* 4 (2016), pp. 6652–6680.

[Tal+17]   V. Talla, B. Kellogg, S. Gollakota, and J. R. Smith. "Battery-Free Cellphone". In: *ACM on Interactive, Mobile, Wearable and Ubiquitous Technologies* 1.2 (June 2017), pp. 2500–2520.

[Tho62]   R. C. Thor. "A Large Time-Bandwidth Product Pulse-Compression Technique". In: *IRE Transactions on Military Electronics* 6.2 (1962), pp. 169–173.

[TOD17]   B. Thoen, G. Ottoy, and L. De Strycker. "An ultra-low-power omnidirectional MEMS microphone array for wireless acoustic sensors". In: *2017 IEEE SENSORS*. 2017, pp. 1–3. DOI: `10.1109/ICSENS.2017.8234392`.

[TS19]   A. Tadayon and M. Stojanovic. "Iterative Sparse Channel Estimation and Spatial Correlation Learning for Multichannel Acoustic OFDM Systems". In: *IEEE Journal of Oceanic Engineering* 44.4 (2019), pp. 820–836.

[Tsa87]   R. Tsai. "A versatile camera calibration technique for high-accuracy 3D machine vision metrology using off-the-shelf TV cameras and lenses". In: *IEEE Journal on Robotics and Automation* 3.4 (1987), pp. 323–344. DOI: `10.1109/JRA.1987.1087109`.

[TXC21]   X. Tang, G. Xie, and Y. Cui. "Self-Sustainable Long-Range Backscattering Communication Using RF Energy Harvesting". In: *IEEE Internet of Things Journal* 8.17 (2021), pp. 13737–13749. DOI: `10.1109/JIOT.2021.3067948`.

[Ure+18]   J. Urena, A. Hernandez, J. J. Garcia, J. M. Villadangos, M. Carmen Perez, D. Gualda, F. J. Alvarez, and T. Aguilera. "Acoustic Local Positioning With Encoded Emission Beacons". In: *Proceedings of the IEEE* 106.6 (2018), pp. 1042–1062.

[Van+18]   N. Van Huynh, D. T. Hoang, X. Lu, D. Niyato, P. Wang, and D. I. Kim. "Ambient Backscatter Communications: A Contemporary Survey". In: *IEEE Communications Surveys Tutorials* 20.4 (2018), pp. 2889–2922. DOI: `10.1109/COMST.2018.2841964`.

[Var+17]   A. Varshney, C. Pérez-Penichet, C. Rohner, and T. Voigt. "LoRea: A Backscatter Architecture That Achieves a Long Communication Range". In: *Proceedings of the 15th ACM Conference on Embedded Network Sensor Systems*. Delft, Netherlands, 2017. ISBN: 9781450354592.

[Ver21]   K. Verniers. "Investigation of Visible Light Communication in a Realistic Indoor Illumination Scenario". PhD thesis. KU Leuven, Feb. 2021.

[Vle+21]   R. Vleugels, B. Van Herbruggen, J. Fontaine, and E. De Poorter. "Ultra-Wideband Indoor Positioning and IMU-Based Activity Recognition for Ice Hockey Analytics". In: *Sensors* 21.14 (2021). DOI: `10.3390/s21144650`.

[Vor07]   M. Vorlander. *Auralization: Fundamentals of Acoustics, Modelling, Simulation, Algorithms and Acoustic Virtual Reality*. en. Berlin, Germany: Springer, Oct. 2007. ISBN: 9783540488293.

[VSV19]   A. Varshney, A. Soleiman, and T. Voigt. "TunnelScatter: Low Power Communication for Sensor Tags Using Tunnel Diodes". In: *MobiCom '19*. 2019. ISBN: 9781450361699.

[Vu+20]   H. S. Vu, N. Nguyen, N. Ha-Van, C. Seo, and M. Thuy Le. "Multiband Ambient RF Energy Harvesting for Autonomous IoT Devices". In: *IEEE Microwave and Wireless Components Letters* 30.12 (2020), pp. 1189–1192. DOI: `10.1109/LMWC.2020.3029869`.

[Wan+17]   A. Wang, V. Iyer, V. Talla, J. R. Smith, and S. Gollakota. "FM Backscatter: Enabling Connected Cities and Smart Fabrics". In: *Proceedings of the 14th USENIX Conference on Networked Systems Design and Implementation*. Boston, MA, USA, 2017, pp. 243–258. ISBN: 9781931971379.

[Wan+20a]   P.-H. P. Wang, C. Zhang, H. Yang, D. Bharadia, and P. P. Mercier. "A 28uW IoT Tag That Can Communicate with Commodity WiFi Transceivers via a Single-Side-Band QPSK Backscatter Communication Technique". In: *IEEE International Solid- State Circuits Conference - (ISSCC)*. 2020, pp. 312–314.

[Wan+20b]   W. Wang, Q. Wang, J. Zhang, and M. Zuniga. "PassiveVLP: Leveraging Smart Lights for Passive Positioning". In: *ACM Transactions on Internet of Things* 1.1 (2020). ISSN: 2691-1914.

[Wan+21] J. Wang, S. Sun, Y. Ning, M. Zhang, and W. Pang. "Ultrasonic TDoA Indoor Localization Based on Piezoelectric Micromachined Ultrasonic Transducers". In: *IEEE International Ultrasonics Symposium (IUS)*. 2021, pp. 1–3. DOI: 10.1109/IUS52206.2021.9593813.

[Wan+22] J. Wang, M. Zhang, Z. Wang, S. Sun, Y. Ning, X. Yang, and W. Pang. "An Ultra-Low Power, Small Size and High Precision Indoor Localization System Based on MEMS Ultrasonic Transducer Chips". In: *IEEE Transactions on Ultrasonics, Ferroelectrics, and Frequency Control* 69.4 (2022), pp. 1469–1477. DOI: 10.1109/TUFFC.2022.3148314.

[Wit+16] K. Witrisal, S. Hinteregger, J. Kulmer, E. Leitinger, and P. Meissner. "High-accuracy positioning for indoor applications: RFID, UWB, 5G, and beyond". In: *IEEE International Conference on RFID (RFID)*. 2016, pp. 1–7.

[WS17] S. Wielandt and L. D. Strycker. "Indoor Multipath Assisted Angle of Arrival Localization". In: *Sensors* 17.11 (Nov. 2017), p. 2522. ISSN: 1424-8220.

[Yan+15] Z. Yang, Z. Wang, J. Zhang, C. Huang, and Q. Zhang. "Wearables Can Afford: Light-Weight Indoor Positioning with Visible Light". In: *Proceedings of the 13th Annual International Conference on Mobile Systems, Applications, and Services*. MobiSys '15. Florence, Italy, 2015, pp. 317–330. ISBN: 9781450334945.

[YJC20] F. Yuan, Z. Jia, and E. Cheng. "Chirp-rate quasi-orthogonality based DSSS-CDMA system for underwater acoustic channel". In: *Applied Acoustics* 161 (2020), p. 107163.

[YWC16] F. Yuan, Q. Wei, and E. Cheng. "Multiuser chirp modulation for underwater acoustic channel based on VTRM". In: *International Journal of Naval Architecture and Ocean Engineering* 9 (Oct. 2016). DOI: 10.1016/j.ijnaoe.2016.09.004.

[ZGL19] F. Zafari, A. Gkelias, and K. K. Leung. "A Survey of Indoor Localization Systems and Technologies". In: *IEEE Communications Surveys Tutorials* 21.3 (2019), pp. 2568–2599.

[Zha+16] P. Zhang, D. Bharadia, K. Joshi, and S. Katti. "HitchHike: Practical Backscatter Using Commodity WiFi". In: *Proceedings of the 14th ACM Conference on Embedded Network Sensor Systems CD-ROM*. Stanford, CA, USA, 2016, pp. 259–271. DOI: 10.1145/2994551.2994565.

[ZS13] Y. Zhao and J. R. Smith. "A battery-free RFID-based indoor acoustic localization platform". In: *IEEE International Conference on RFID*. 2013, pp. 110–117.

[Zwi+15] L. Zwirello, T. Schipper, M. Jalilvand, and T. Zwick. "Realization Limits of Impulse-Based Localization System for Large-Scale Indoor Applications". In: *IEEE Transactions on Instrumentation and Measurement* 64.1 (2015), pp. 39–51.

List of Publications

Articles in Internationally Reviewed Academic Journals

B. Cox, C. Buyle, D. Delabie, L. Van der Perre and L. De Strycker, "Positioning Energy-Neutral Devices: Technological Status and Hybrid RF-Acoustic Experiments." in Future Internet, 14 (5), Art. No. 156, 2022, doi: 10.3390/fi14050156

B. Cox, L. Van der Perre, S. Wielandt, G. Ottoy and L. De Strycker, "High Precision Hybrid RF and Ultrasonic Chirp-based Ranging for Low-Power IoT Nodes." in Eurasip Journal On Wireless Communications And Networking, Art. No. 187, 2020, doi: 10.1186/s13638-020-01795-1

B. Cox, L. Van der Perre and L. De Strycker, "Zero-crossing Chirp Frequency Demodulation for Ultra Low-Energy Precise Hybrid RF-Acoustic Ranging of Mobile Nodes." in IEEE Sensors Letters, 4 (5), Art. No. 7001504, 2020, doi: 10.1109/LSENS.2020.2990213

Articles in International Conferences and Symposia

Peer Reviewed

B. Cox, C. Buyle, L. Van der Perre and L. De Strycker: "Towards Centimetre Accurate and Low-Power, Hybrid Radio-Acoustic 3D Indoor Positioning: an Experimental Journey", in CEUR Workshop Proceedings of IPIN Conference: vol. 3097, Lloret de Mar, Spain, 2021, Open Access

C. Buyle, **B. Cox**, L. Van der Perre and L. De Strycker: "A Multi-band Solution for Interacting with Energy-Neutral Devices", in 2021 55th Asilomar

Conference on Signals, Systems, and Computers, Pacific Grove, USA, 2021, doi: 10.1109/IEEECONF53345.2021.9723184

B. Cox, C. Buyle, L. Van der Perre and L. De Strycker: "Energy-Neutral Devices: Can Hybrid RF-Acoustic Signals Point Them Out?", in 2020 54th Asilomar Conference on Signals, Systems, and Computers, Pacific Grove, USA, 2020, doi: 10.1109/IEEECONF51394.2020.9443432

C. Buyle, **B. Cox**, and L. Van der Perre: "Low Power Ultrasound Location System for Secure Identification", in Proceedings of the 2018 International Conference on Indoor Positioning and Indoor Navigation (IPIN), Nantes, France, 2018, Open Access

Q. Yan, J. Chen, G. Ottoy, **B. Cox**, and L. De Strycker: "Low Power Ultrasound Location System for Secure Identification", in Sensors Applications Proceedings 2018 Symposium Proceedings, Seoul, South Korea, 2018, doi: 10.1109/SAS.2018.8336730

B. Cox, L. De Strycker and L. Van der Perre: "Acoustic Backscatter: Enabling Ultra-Low Power, Precise Indoor Positioning?", in 2018 Ubiquitous Positioning, Indoor Navigation and Location-Based Services (UPINLBS), Wuhan, China, 2018, doi: 10.1109/UPINLBS.2018.8559762

B. Cox, G. Ottoy and L. De Strycker: "Development of an Optoacoustic Distance Measurement System.", in International Conference on Indoor Positioning and indoor Navigation (IPIN), Alcala de Henares, Spain, 2016, ISBN: 978-1-5090-2424-7.

D. Delabie, **B. Cox** , L. De Strycker and L. Van der Perre: "Techtile: a Flexible Testbed for Distributed Acoustic Indoor Positioning and Sensing.", Sensors Applications Symposium (SAS), Sundsvall, Sweden, 2022

Not Peer Reviewed

C. Buyle, B. Thoen, **B. Cox**, M. Alleman, S. Wielandt and L. De Strycker: "Ultra-Low-Power Smart Sensing Platform for Urban Sound Event Monitoring", in Proceedings of the 2019 Symposium on Information Theory and Signal Processing in the Benelux, Ghent, Belgium, 2019, ISBN: 978-94-918-5703-4

C. Buyle, **B. Cox**, and L. Van der Perre: "Measurement-based Assessment of Noise Sources in Office and Household Environments Impacting Ultrasound Indoor Positioning", in Proceedings of the 2018 Symposium on Information Theory

and Signal Processing in the Benelux, Enschede, The Netherlands, 2018, ISBN: 978-90-365-4570-9

B. Cox, B. Thoen, V. Rijmen, L. De Strycker and L. Van der Perre: "Directivity Assessment of MEMS Microphones in Microphone Array Applications", in Proceedings of the 2017 Symposium on Information Theory and Signal Processing in the Benelux, Delft, The Netherlands, 2018, ISBN: 978-94-6186-811-4

C. Buyle, **B. Cox**, T. Baele, L. Monteyne and L. De Strycker: "Compressed Sensing in Wireless Acoustic Sensor Networks", submitted to 2022 Symposium on Information Theory and Signal Processing in the Benelux, Louvain-La-Neuve, Belgium, 2022

FACULTY OF ENGINEERING TECHNOLOGY
DEPARTMENT OF ELECTRICAL ENGINEERING
DRAMCO-WAVECORE
Gebroeders De Smetstraat 1
B-9000 Gent
bert.cox@kuleuven.be